ABSTRACT

Title of dissertation: NUMERICAL STUDIES ON NEW
                         TECHNIQUES FOR GRAVITATIONAL
                         WAVE EXTRACTION AND BINARY
                         BLACK HOLE SIMULATIONS

                         Enrique Pazos, Doctor of Philosophy, 2009

Dissertation directed by: Professor Manuel Tiglio
                            Department of Physics

This dissertation presents numerical studies of gravitational waves produced by black holes in two scenarios: perturbations of a single black hole, and the collision of a binary pair. Their detection plays a crucial roll in further testing General Relativity and opens a whole new field of observational astronomy.

First, a technique called Cauchy–perturbative matching is revisited in one dimension through the use of new numerical methods, such as high order finite difference operators, constraint-preserving boundary conditions and, most important, a multi-domain decomposition (also referred to as multi-patch, or multi-block approach).

These methods are then used to numerically solve the fully non-linear three-dimensional Einstein vacuum equations representing a non-rotating distorted black hole. In combination with a generalization of the Regge-Wheeler-Zerilli formalism, we quantify the effect of the background choice in the wave extraction techniques. It is found that a systematic error is introduced at finite distances. Furthermore,

such error is found to be larger than those due to numerical discretization.

Subsequently, the first simulations ever of binary black holes with a finite-difference multi-domain approach are presented. The case is one in which the black holes orbit for about twelve cycles before merging. The salient features of this multi-domain approach are: i) the complexity of the problem scales linearly with the size of the computational domain, ii) excellent scaling, in both weak and strong senses, for several thousand processors.

As a next step, binary black hole simulations from inspiral to merger and ringdown are performed using a new technique, turduckening, and a standard finite difference, adaptive mesh-refinement code. The computed gravitational waveforms are compared to those obtained through evolution of the same exact initial configuration but with a pseudo-spectral collocation code. Both the gravitational waves extracted at finite locations and their extrapolated values to null infinity are compared.

Finally, a numerical study of generic second order perturbations of Schwarzschild black holes is presented using a new gauge invariant high order perturbative formalism. A study of the self-coupling of first order modes and the resulting radiated energy, in particular its dependence on the type of initial perturbation, is detailed.

NUMERICAL STUDIES ON NEW TECHNIQUES FOR GRAVITATIONAL WAVE EXTRACTION AND BINARY BLACK HOLE SIMULATIONS

by

Enrique Pazos

Dissertation submitted to the Faculty of the Graduate School of the
University of Maryland, College Park in partial fulfillment
of the requirements for the degree of
Doctor of Philosophy
2009

Advisory Committee:
Professor Manuel Tiglio, Chair/Advisor
Professor Dieter Brill
Professor Alessandra Buonanno
Professor Christopher Reynolds
Professor Peter Shawhan

Preface

Portions of the research described in this work have been published elsewere. The contents of Chapter 2 appeared in a modified form in [180]. Chapter 3 was published in a modified form in [132]. Chapter 4 was published in a modified version in [133].

Dedication

To my parents, for giving me life.

To life, for giving me parents.

And to the...

Blissful, magical, glorious moments

enacted by the characters in a cosmic play,

allow them to dwell in our hearths.

Greet the time that shall make them gray.

Acknowledgments

Table of Contents

List of Tables

List of Figures

xvii

Chapter 1

Introduction

In the last few years the field of Numerical Relativity has reached a landmark state of maturity. As a consequence, it is now possible to numerically model the two-body problem of General Relativity, i.e. the dynamics of the gravitational field produced by compact objects orbiting around each other. The hallmark feature of such a problem is the prediction of an energy flow leaving the system, carried away by *gravitational waves*. The existence of gravitational waves is a prediction of Einstein's field equations of General Relativity [70]. Since the past century, Einstein's geometrical description of gravity has passed stringent tests, such as the the perihelion shift of Mercury, the bending of light around massive objects and the loss of energy in binary pulsars [172]. The first two validate General Relativity in the weak field regime whereas the later is an indirect confirmation of the existence of gravitational waves produced in a dynamical and much stronger gravitational field. Notwithstanding all the experimental confirmations, a direct detection of gravitational waves has not yet been made. That is the main drive behind Numerical Relativity, the necessity to accurately model and predict the gravitational radiation generated in a highly dynamical strong field regime [31]. This need stems from the fact that gravitational waves will be so faint by the time they reach our earth-based interferometer gravitational wave detectors that they will be buried in the charac-

teristic noise of the apparatus [116]. As a consequence, the ability to model binary pairs in General Relativity and, in particular, to generate a bank of gravitational wave templates, is a key component for the detection of such waves.

The task of detecting gravitational waves is not limited to asserting the validity of General Relativity. Its main goal is to explore the universe by 'listening' [1] to the gravitational waves produced in cataclysmic astrophysical events. In this regard, the main tools for modeling gravitational waves—namely, Post-Newtonian approximations [29, 71, 104], Perturbation Theory [142, 177] and Numerical Relativity [54, 138, 19]—have shown that the dynamics and certain properties of the system are encoded in the shape of the wave, i.e. the waveform. Quantities such as the masses of the compact objects, their angular momentum and eccentricity of the orbit can be accessed via gravitational waves [43]. It is therefore of extreme interest to be able to detect and analyze gravitational wave emissions, which in short will constitute a new field of physics, namely that of *gravitational wave astronomy.* This field will play an important role in gaining a deeper understanding of the universe we live in. Thanks to the advances in theoretical modeling and the construction and continuous improvement of ground-based gravitational wave observatories, such as LIGO [6], VIRGO [169], TAMA [166] and GEO [173], gravitational wave astronomy will soon provide us information about the cosmos that has been so far not accessible.

The challenge of studying and modeling sources of gravitational waves has

---

[1]A gravitational wave is akin to a sound wave, being possible to assign an audible frequency to its chirp signal.

proven to be a difficult one. The inherent complexity of the Einstein equations has motivated the use of computational numerical tools to unravel the behavior of the gravitational field, especially in the strong field regime. Advances achieved in Numerical Relativity have been possible through a combination of computational technology, mathematical formalisms, and physical insight. Progress in all three fronts has enabled the current capabilities for simulating binary collisions of a black hole and a neutron star, two black holes or two neutron stars.

1.1   Numerical Relativity and Perturbation Theory

In Numerical Relativity one is interested in finding solutions to the Einstein equations using numerical algorithms. In order to achieve this goal the most important step is to write the equations in the form of an initial value problem. The way in which this is done consists in splitting the four-dimensional spacetime into a foliation of three-dimensional spacelike hyper-surfaces which are labeled by a time coordinate. This is commonly referred to as the *3+1 decomposition* of the Einstein equations [121]. The idea is to give initial data at a given initial hyper-surface and *evolve* them in time using Einstein's equations. The choice of initial data is not completely free since they have to satisfy four constraints. The constraints are equations that do not contain time derivatives. The computed solution from any given initial data needs to fulfil the constraint equations at all times. For this reason, monitoring such quantities provides a measure of the error in the numerical solution.

Perturbation theory is useful to study spacetimes for which deviations from a

known analytic solution are small. For the binary black hole problem, the ringdown stage can be analyzed using this framework, since the system can be approximated as a single black hole (the background geometry) plus small perturbations (the gravitational waves). When one considers as background the spacetime of a Schwarzschild black hole, the perturbations are described by the Regge-Wheeler and the Zerilli equations, for odd and even parity perturbations respectively [60]. Once we know the solutions to these equations it is possible to compute the metric perturbations which are added to the background spacetime thus obtaining the whole description of the system. The apparatus of perturbation theory can also be used in the reverse way, i.e. starting from a full numerical solution and separating the metric in a background part plus a perturbation part. The metric perturbations are decomposed in tensor spherical harmonics and with these multipoles the Regge-Wheeler and Zerilli functions are computed. They satisfy the corresponding Regge-Wheeler and Zerilli master equations.

1.2   This work

In this dissertation, we present and discuss some of the mathematical and numerical techniques that have been successfully integrated as standard tools for modeling gravitational wave sources. We focus our attention to applications in Numerical Relativity simulations and the computation of gravitational waveforms using Perturbation Theory.

The work presented here relies heavily on high-order finite difference methods.

The numerical scheme is based on a new family of highly optimized, efficient, and accurate difference operators satisfying Summation By Parts (SBP) and a penalty technique to handle communication among patches or blocks in a way that ensures numerical stability. These numerical techniques are described in [111, 61], where they are implemented in a parallel modular infrastructure for solving the Einstein equations on non-trivial geometries [155]. The techniques and infrastructure have been tested in a variety of three-dimensional numerical relativity simulations [65]. More recently, all this machinery has been successfully used in the more complicated case of binary black holes [133]. As described in that reference, the coordinate conditions used in those simulations are rather simple and they crash while entering the merger regime. In order to handle this phase of the collision, we use the "turducken" technique [40, 38]. Data corresponding to the "late" stage of an inspiral multi-domain simulation is saved at a given instant of time and the interior of the holes is filled in. The resulting data is then read by our AMR turducken code and evolved through the merger and ringdown.

The results presented in this dissertation are organized as follows. In Chapter 2 we study in detail some of the basic mathematical tools that have been instrumental in black hole numerical simulations. We do this in the context of the Cauchy–perturbative matching problem in spherical symmetry. The basic setting for this problem is to have two numerical algorithms that solve a set of different equations in different parts of the domain. In our case we solve for Einstein equations coupled to a scalar field in the inner part of the domain. Whereas in the outer part, we only solve for the equations of motion of the scalar field. The idea is to mimic the

behavior of the gravitational field in the numerical relativity simulations, i.e. that the geometry is dynamical close to the coordinate origin but is almost static far away from that point. Since the scalar field is the same in both inner and outer regions, we need to communicate or to *match* that information at the boundary of the two regions. The mathematical tools that make this problem worth revisiting are: high-order finite difference operators, the penalty method to communicate information across different domains and constraint-preserving boundary conditions.

High-order finite difference operators that satisfy the summation by parts property and their corresponding dissipation operators ensure the stability of the numerical scheme. All the finite difference simulations presented here make use of these operators. The penalty method plays a fundamental role in all the simulations that benefit from a multi-block (or multi-patch) domain structure. In Chapters 3 and 4 this technique is applied to three-dimensional multi-block simulations of a single perturbed and binary black hole, respectively. In Chapter 6 the same technique is applied to a one-dimensional pseudo-spectral method code.

Constraint-preserving boundary conditions are important since they don't pollute the numerical solution. In the Cauchy–perturbative problem they are used to impose boundary conditions in a way consistent with the Einstein equations. They make clear what are the physical modes that need to be communicated when matching a full Cauchy evolution with a perturbative one.

Chapter 3 presents a method for extracting gravitational waves from numerical spacetimes which generalizes and refines one of the standard methods based on the Regge–Wheeler–Zerilli perturbation formalism. At the analytical level, this gener-

alization allows a much more general class of slicing conditions for the background geometry, and is thus not restricted to Schwarzschild–like coordinates. At the numerical level, our approach uses high-order multi-block methods (see Chapter 2), which improve both the accuracy of our simulations and of our extraction procedure. In particular, the latter is simplified since there is no need for interpolation, and we can afford to extract accurate waves at large radii with only little additional computational effort.

We perform fully nonlinear three-dimensional numerical evolutions of a distorted Schwarzschild black hole in Kerr–Schild coordinates with an odd parity perturbation and analyze the improvement we gain from our generalized wave extraction, comparing our new method to the standard one. This comparison is done using the extracted waves and one-dimensional high resolution solutions of the corresponding generalized Regge–Wheeler equation.

In Chapter 4 we turn our attention to the binary black hole problem. We present numerical simulations of orbiting black holes for around twelve cycles, using a high-order finite difference multi-patch approach. Unlike some other approaches, the computational speed scales almost perfectly for thousands of processors. Multi-patch methods are an alternative to adaptive mesh refinement, with benefits of simplicity and better scaling for improving the resolution in the wave zone. The results presented here pave the way for multi-patch evolutions of black hole-neutron star and neutron star-neutron star binaries, where high resolution grids are needed to resolve details of the matter flow.

Chapter 5 presents results from waveform comparison using two different Nu-

merical Relativity codes. One code is based on pseudo-spectral collocation methods with a multi-domain decomposition. The other is a finite difference based code using adaptive mesh refinement and the "turducken" technique. We performed three-dimensional simulations of binary black holes with both codes using the *same* initial data. This initial data set is a snapshot of one of the simulations carried out by the Caltech-Cornell collaboration. The time chosen for our study corresponds to about three orbits before merger. Setting the initial conditions of the simulations in this way allows us to eliminate initial junk radiation otherwise present. Furthermore, it enables us to eliminate the differences in the computed waveforms originated by using nominally physically equivalent yet different initial data.

Finally, in Chapter 6 we make use of a recently developed gauge-invariant formalism for studying generic second-order perturbations of Schwarzschild black holes. We use that formalism to numerically study the second-order corrections to linear gravitational radiation due to the self-coupling of linear $(\ell = 2, m = \pm 2)$ even-parity perturbations, which due to selection rules turn out to be the $(\ell = 4, m = \pm 4)$ and $(\ell = 2, m = 0, \pm 2)$ even-parity modes. We numerically compute the gravitational radiation emitted by these four modes for a variety of initial perturbations and study their dependence on the parameters of such initial data. We also investigate the frequency of oscillations and damping rates of the radiated gravitational waves associated to non-linear modes. Contrary to previous claims in the literature, we find that they essentially oscillate with the standard, linear quasi-normal mode frequencies.

Chapter 2

Cauchy–perturbative matching revisited: tests in spherical symmetry

2.1 Introduction

It is generally expected that the geometry of compact sources should resemble flat spacetime at large enough distances. This is true not only qualitatively, but through very precise falloff conditions that are built into the formal definition of asymptotic flatness. Within this definition, the deviations from flat spacetime are well described (in the sense of the leading order behaviour of an expansion in powers of "$1/r$") by perturbations of the Schwarzschild spacetime [123].

Such perturbations can in turn be studied through the gauge invariant Regge-Wheeler and Zerilli (RWZ) formalisms [142, 177]. These allow one to derive, after a spherical harmonic decomposition (that is, for each "(ℓ, m)"), two master evolution equations for the truly gauge invariant, linearized physical degrees of freedom. Due to the multipole decomposition, these equations involve only one spatial coordinate (the radial one). The fact that they are one-dimensional implies that these master equations can be solved for very large computational domains with very modest computational resources. On the other hand, three-dimensional Cauchy codes are very demanding on their resource requirements. Even though mesh refinement can help in this respect, there is a limit to how much one can coarsen the grid in the asymptotic region; this limit is set by the resolution required to reasonably represent

wave propagation in the radiative zone. The use of a grid structure adapted to the physical geometry (possibly through multiple patches) can also help [112, 168, 98], but one still ends up imposing artificial (even if constraint-preserving) boundary conditions at the outer boundary. For example, one in general misses information about the geometry outside the domain [108].

Two approaches that at the same time provide wave extraction, physically motivated boundary conditions, and extend the computational domain to the radiative regime are Cauchy–characteristic [175, 28, 80] and Cauchy–perturbative matching (CPM) [2, 143, 148, 79]; here we are concerned with the latter. In the first case, the idea is to match at each timestep a fully non-linear Cauchy code to an outer one solving, the RWZ equations,[1] which describe the gravitational waves as perturbations of a given background. In the later case, the Cauchy code is matched to a code that uses null (characteristic) surfaces to foliate the spacetime.

We plan to revisit CPM in the light of some recent technical developments —which we describe below— that should help in its implementation. Before discussing these developments, we point out and summarize some features present in the original implementation of CPM [148] which we hope to improve on:

1. The non-linear Cauchy equations were solved on a Cartesian, cubic grid. On the other hand, the RWZ equations use a radial coordinate for the spatial dimension. Mixing Cartesian coordinates with spherical ones leads to the need

---

[1]Even though including the angular momentum of the background is a high-order correction in terms of powers of $1/r$, one might, in principle, try to solve for perturbations of Kerr spacetime (as opposed to Schwarzschild).

for interpolation back and forth between both grids. Especially when using high-order methods, this type of interpolation might not only be complicated but also subtle: depending on how it is done it might introduce noise and sometimes it might even be a source of numerical instabilities.

2. When injecting data from the perturbative module to the Cauchy code and vice versa boundary conditions were given to all modes, irrespectively of their propagation speed and without taking into account the existence of constraint violating boundary modes. One would intuitively expect a cleaner matching if boundary conditions are given according to the characteristic (propagation) speeds of the different modes, and even cleaner if constraint preservation is automatically built in during the matching.

3. Low-order numerical schemes, which result in slow convergence, were used.

In recent years there has been progress on several related fronts that should in principle help in the implementation of CPM. We describe these new results next[2]:

1. The first improvement is the ability to implement smooth (in particular, spherical) boundaries in 3D Cauchy evolutions [112, 168, 98]. One important advantage of this is the fact that the matching can be performed —to either a perturbative or a characteristic outer module— without the need for in-

---

[2]There is actually another ingredient: the use of a generalized perturbative formalism that allows for any (spherically symmetric) slicing of the background Schwarzschild metric [149]. However, since such ingredient will not appear in the simplified model that we look at here, we skip its discussion here.

terpolation between spherical and Cartesian grids. In that way a possible source of noise can be eliminated. It is now understood how to match different domains using schemes of arbitrary high order while at the same time ensuring numerical stability. One way of doing so is through the use of multiple patches (much in the same way multiple charts are used in differential geometry), penalty terms and difference operators satisfying summation by parts (SBP) [112] (more about this below). This is the approach we shall explore here in the context of CPM[3].

2. The second improvement is the construction of constraint-preserving boundary conditions (CPBC). Several efforts have by now reported numerically stable (in the sense of convergent) implementations of such boundary conditions for the fully three-dimensional non-linear Einstein's equations [150, 100, 165]. Furthermore, there have been reports in the context of three-dimensional Cauchy–characteristic matching that significant improvements are obtained when this type of boundary conditions are used in the matching [165]. With this in mind, we will test their use in CPM.

3. Lastly, new, accurate and efficient high order difference operators satisfying SBP and associated dissipative operators have been constructed recently [162, 163, 120, 61]. As mentioned above, in conjunction with certain penalty

---

[3]Regardless of whether matching is present or not, the use of multiple coordinate patches has advantages when modeling black holes through excision of the singularity from the computational domain.

interface treatment such operators guarantee numerical stability when "glue-ing" together different computational grids. We will test these operators in the context of CPM.

We have incorporated these techniques, i.e., high-order summation-by-parts finite differencing and dissipation operators, multiple coordinate patches with penalty inter-patch constraint-preserving boundary conditions and Cauchy–perturbative matching, into a spherically symmetric numerical code evolving the Einstein–Christoffel form of the field equations [13], minimally coupled to a Klein-Gordon field. Using this tool, we can test the performance of the numerical methods in a non-trivial, but easily reproducible and computationally inexpensive setting, and gain experience for three-dimensional applications. The evolutions presented here model black holes with excision in isolation, under dynamical slicings, and black holes accreting scalar field pulses, which are used as a scalar analogue of gravitational radiation.

The presentation is as follows. In section 2.2 we introduce the continuum system and the numerical techniques we have used. Results are presented in section 2.3, where a black hole is evolved successively from simple settings, i.e., single-patch, isolated, Killing-field adapted gauges, to more involved ones including Cauchy–perturbative matching and scalar pulse accretion. Finally, in section 2.4, we draw conclusions and give an outlook to future work.

2.2 Equations and Methods

2.2.1 Evolution equations and constraint-preserving boundary conditions

We use the Einstein–Christoffel (EC) system [13] in spherical symmetry. We follow the notation of Ref. [99]; in particular, the densitized lapse is denoted by $\alpha = N g^{-1/2}$, and $\tilde{\alpha} = \alpha r^2 \sin(\theta)$ is introduced for convenience. Here, g is the determinant of the 3-metric and N the lapse function, while the 4-metric is written as

$$ds^2 = -N^2 dt^2 + g_{rr}(dr + \beta dt)^2 + r^2 g_T(d\theta^2 + \sin^2 \theta d\phi^2)$$

The vacuum part of the evolution equations in spherical symmetry for this formulation constitute a symmetric hyperbolic system of six first order differential equations. The vacuum variables are the two metric and extrinsic curvature components

$$g_{rr}, \ g_T, \ K_{rr}, \ K_T,$$

where the extrinsic curvature is written as

$$K_{ij} = K_{rr}dr^2 + r^2 K_T(d\theta^2 + \sin^2 \theta d\phi^2),$$

plus two auxiliary variables needed to make Einstein's equations a first order system. These extra variables are defined as

$$
\begin{aligned}
f_{rrr} &= \frac{g'_{rr}}{2} + 4\frac{g_{rr} f_{rT}}{g_T}, \\
f_{rT} &= \frac{g'_T}{2} + \frac{g_T}{r}.
\end{aligned}
$$

14

In addition, a massless Klein-Gordon field is minimally coupled to the geometry [98, 47]. The scalar field equation

$$g^{ab}\nabla_a\nabla_b\Psi = 0$$

is converted into a first order system by introduction of the variables

$$\Pi = \frac{1}{N}(\beta\Psi' - \dot{\Psi}),$$
$$\Phi = \Psi'.$$

Throughout this chapter the 'prime' and 'dot' represent partial derivatives with respect to r and t, respectively.

Constraint preserving boundary conditions are imposed by analyzing the characteristic modes of the main and constraint evolution systems, as discussed in [47]. These modes and their associated characteristic speeds are summarized in Table 2.1. For illustration purposes, we also show the direction of propagation of each mode in the Schwarzschild spacetime in Painlevé-Gullstrand coordinates [131, 85, 117].

From Table 2.1 we notice that for the Schwarzschild spacetime there are four ingoing (left) and two outgoing (right) gravitational modes at the outer boundary, and therefore expect the same count to hold for perturbations thereof. Boundary conditions for the incoming modes u_1, u_2 and u_4 are fixed by the CPBC procedure. Thus, the only free incoming modes are u_3, which represents a gauge mode and u_8, which represents a physical one (see [47] for more details). Boundary conditions do not need to be specified at the inner boundary if it is located inside the event horizon, because all modes are outflow then.

Mode	Speed	$r < 2M$	$r > 2M$
$u_1 = g_{rr}$	β	left	left
$u_2 = g_T$	β	left	left
$u_3 = K_{rr} - f_{rrr}\, g_{rr}^{-1/2}$	$\beta + \tilde\alpha\, g_T$	left	left
$u_4 = K_T - f_{rT}\, g_{rr}^{-1/2}$	$\beta + \tilde\alpha g_T$	left	left
$u_5 = K_{rr} + f_{rrr}\, g_{rr}^{-1/2}$	$\beta - \tilde\alpha g_T$	left	right
$u_6 = K_T + f_{rT}\, g_{rr}^{-1/2}$	$\beta - \tilde\alpha g_T$	left	right
$u_7 = \Pi + \Phi\, g_{rr}^{-1/2}$	$\beta - \tilde\alpha g_T$	left	right
$u_8 = \Pi - \Phi\, g_{rr}^{-1/2}$	$\beta + \tilde\alpha g_T$	left	left

Table 2.1: Characteristic modes for Einstein-Christoffel system in spherical symmetry, and their direction of propagation for a Schwarzschild spacetime in Painlevé-Gullstrand coordinates with respect to the vector field ∂_r. In this gauge, all modes are outflow at the inner boundary, if it is located at $r < 2M$, while boundary conditions have to be applied to the incoming modes u_1, u_2, u_3, u_4 and u_8 at the outer boundary, assuming is is located at $r > 2M$.

2.2.2 Cauchy–perturbative matching

Since there is no radiative degree of freedom in spherically symmetric space-times, we use the massless Klein-Gordon field as a scalar analogue of gravitational waves. To emulate the setup of three-dimensional Cauchy–perturbative matching as closely as possible, the scalar wave is evolved on a fixed Schwarzschild background in a "perturbative" patch defined for $r \geq r_m$, while the fully non-linear Einstein's equations are evolved in the "Cauchy" patch, defined for $r \in [r_e, r_m]$, where r_e and r_m denotes the excision radius and the matching radius, respectively.

The fact that we are using CPBC allows us to perform a clean matching. From the analytical point of view our matching works in the following way: As mentioned above, after the CPBC procedure, only two free characteristic modes are entering the Cauchy computational domain (at $r = r_m$), denoted by u_3 and u_8. Since in a very precise sense u_3 is a gauge mode, we are free to give boundary conditions to it in a very simple way: we just set it to its initial value. Regarding u_8, we use the "perturbative" value of the same quantity coming from the perturbative domain as counterpart, and communicate these two modes (how this is done at the numerical level is explained below). Similarly, there is only one characteristic mode entering the perturbative domain, which is the linearized version of u_7. We therefore communicate the non-linear and linear versions of that mode as well.

2.2.3 Discrete techniques

Given a well-posed initial-boundary value problem for Einstein's field equations, we construct a stable and accurate discrete system by using operators satisfying the SBP property. In short, a finite difference operator, D, satisfies SBP on a computational domain $[a, b]$ discretized using grid points $i = 1, \ldots, n$ and a grid spacing h if

$$\langle u, Dv \rangle + \langle v, Du \rangle = (uv)\,|_a^b \tag{2.1}$$

holds for all grid functions u, v. Here the scalar product, is defined in terms of its coefficients σ_{ij} by

$$\langle u, v \rangle = h \sum_{i,j=1}^{n} u_i v_j \sigma_{ij}. \tag{2.2}$$

Here we use the new, efficient, and accurate high-order SBP difference operators and associated dissipation operators constructed in Ref. [61]. Thus, as mentioned, this study also serves as an extra test of those new operators.

SBP operators are standard centered finite difference operators in the interior of the domain, but the stencils are modified to yield lower-order operators in a region close to the boundaries (at the boundary itself the stencil is completely one sided). There are several types of SBP operators depending on the properties of the norm. The simplest are the diagonal norm operators. They have the advantage that SBP is guaranteed to hold in several dimensions by simply applying the 1D operator along each direction and that numerical stability can be guaranteed by discrete energy estimates in a wide range of cases. The main disadvantage is that the order of the operator at and close to the boundary is only half the interior order. We denote the

SBP operators by the interior and boundary order and consider here the diagonal operators D_{2-1}, D_{4-2}, D_{6-3} and D_{8-4}. The second type is the restricted full norm operators, where the norm is diagonal at the boundary but has a non-diagonal block in the interior. The advantage of these operators is that the order at and close to the boundary is only one order lower than in the interior, while the disadvantage is that schemes based on these operators may be unstable without the use of dissipation. The restricted full operators we use here are D_{4-3} and D_{6-5}. The subscripts donote the order of accuracy of the operator. The first number is the order in the interior and the second is the order at the boundary.

If the computational domain is split into several sub-domains ("patches"), the discrete representation requires a stable technique to communicate the solution at inter-patch boundaries. We make use of a penalty method [112], which adds a damping term to the right hand side of the evolution equation at the boundary point in a way which retains linear stability. The method has a free parameter, called δ in Ref. [112], which determines how much the difference between characteristic fields on either side of the inter-patch boundary is penalized. Different values of δ result in different amount of energy dissipation at the inter-patch boundary and can in principle be chosen so that no energy is dissipated (this is marginally stable). Usually the value of δ is chosen such that some dissipation of energy occurs. With constant values of δ the amount of dissipation decreases with resolution.

2.2.4 Numerical code

For the purposes of our discussion, a one-dimensional code which supports constraint-preserving boundaries, multiple grid patches, and the use of the aforementioned high order SBP derivative and dissipation operators has been developed. In addition, the code is able to reproduce the (single grid and without CPM matching) second-order methods of Ref. [47] for comparison. We use the methods of lines [136], and the time integration is performed by a 4th order Runge-Kutta method. The grid patches that we consider here are not intersecting, but touching. This implies, that each grid function is double valued at the patch interface coordinate since the SBP derivative operators are one sided at the boundaries. To ensure consistency without compromising (linear) stability, we make use of a penalty method as described above. Constraint-preserving boundary conditions require the calculation of derivatives of certain grid functions at the outer boundary, which we also obtain by using the SBP derivative operators.

In a black hole setting, the computational domain next to the excision boundary tends to quickly amplify high frequency noise, which can not be represented accurately on the discrete grid. This is especially true for high order accurate derivative operators. Thus, high order simulations of black holes need a certain amount of numerical dissipation to be stable. This dissipation is here provided by the SBP dissipation operators constructed in Ref. [61]. The free parameters of these operators, namely the coefficient of the dissipation and the extent of the transition region (for non-diagonal operators), are found by numerical experiment.

2.3 Results

The numerical experiments presented in this section are set up to systematically test the performance of the new techniques in several situations of increasing difficulty. We start with a series of tests evolving a Schwarzschild black hole in Painlevé-Gullstrand coordinates with either a single patch or two patches matched via the penalty method, and compare the performance of all SBP operators with the second order finite-differencing method presented in [47]. Next, to test more dynamical situations, a gauge or scalar field signal is injected in a constraint-preserving manner through the outer boundary and accreted onto the black hole. A robust stability test is then performed with noise on the incoming gauge mode u_3, and, with Cauchy–perturbative matching, on the scalar field mode u_8. Finally, a series of high-precision tests involving all techniques are presented, in which a black hole accretes a scalar field injected through the outer boundary of the perturbative patch.[4] These simulations also include a test of the long-term stability and accuracy after accretion and ring-down.

2.3.1 Schwarzschild black hole in Painlevé-Gullstrand coordinates

In our first series of tests, a Schwarzschild black hole is evolved with high-order accurate SBP operators, constraint-preserving boundary conditions and excision. Cauchy–perturbative matching is not used in these tests. To fix the coordinate

---

[4]Note that boundary conditions are used to inject a pulse into the domain. This permits to get nontrivial solutions without solving the constraints for the initial data. These outer boundary conditions are non-physical in the sense that we are injecting waves, not extracting them.

system, we make use of the horizon-penetrating Painlevé-Gullstrand coordinates [85, 117], and we fix the coordinate functions $\tilde{\alpha}$ and β of the previous section to their exact values.

For all tests, the inner boundary is located well inside the event horizon (more precisely, it is located at $r_e = 1M$), which implies that all modes are outflow. Therefore, no boundary conditions may be applied at the excision boundary. The exact boundary location is not crucial as long as it is inside the apparent horizon, but this choice facilitates comparison with [47]. Also, in dynamical situations the apparent horizon location may move significantly on the coordinate grid, and to ensure outflow conditions at the inner boundary some penetration into the black hole is advantageous. To match the setup of [47], we set the outer boundary to $r = 10M$. To ensure well-posedness of the continuum problem, boundary conditions should be applied to the incoming modes u_1, u_2, u_3, u_4, and u_8. However, three of these modes, namely u_1, u_2, and u_4, can be fixed by the use of constraint-preserving boundary conditions, as discussed in Section 2.2, which leaves the freely specifiable gauge mode u_3 and the scalar field mode u_8. Since in these initial tests we are only interested in obtaining a stationary black hole solution, the initial scalar field is set to zero, and the (scalar field) characteristic mode u_8 is penalized to zero as well. The incoming gauge mode u_3 is penalized to the exact solution.

An error function δM can be defined by use of the Misner-Sharp mass function [122]

$$M(r) := \frac{r g_T}{2} \left[1 + \frac{r^2}{g_T} \left(K_T^2 - \frac{f_{rT}^2}{g_{rr}} \right) \right], \tag{2.3}$$

where then, if the black hole mass is denoted by M, $\delta M(r) = (M(r) - M)/M$. Since the same error measure and continuum system is used in [47], we can compare the different discrete approaches directly.

2.3.1.1 One grid patch

The computational domain $r \in [1, 10]$ is represented by one coordinate patch, which is exactly the same setup as in Ref. [47]. In Figure 2.1 we compare for coarse and high resolutions, $\Delta r = M/8, M/64$, the performance of the methods used in Ref. [47], namely second order spatial derivatives with fourth order Kreiss-Oliger dissipation (which is set to zero near the boundaries) and a third order extrapolation at the boundaries, with the SBP derivative and dissipation operators D_{2-1}, D_{4-2}, D_{4-3}, D_{6-3}, D_{6-5} and D_{8-4}. The figure shows the evolution of the L_2 norm of the Misner-Sharp mass error over an evolution time of $10,000M$. In all cases displayed there is a linear growth in the error after some time. This is an artefact of the discrete representation of the constraint-preserving boundary conditions. We have also performed tests with maximally dissipative boundary conditions: these yield a discrete equilibrium after some time, and thus allow for evolutions of unlimited time. However, since these boundary conditions are not correct for most systems of practical interest, we only make use of this result to point out the source of the linear growth of errors observed, which converges away with increasing resolution.

As soon as the error gets close to 1, the code encounters an instability, which, in this case, is associated with a migration of the excision boundary outside of
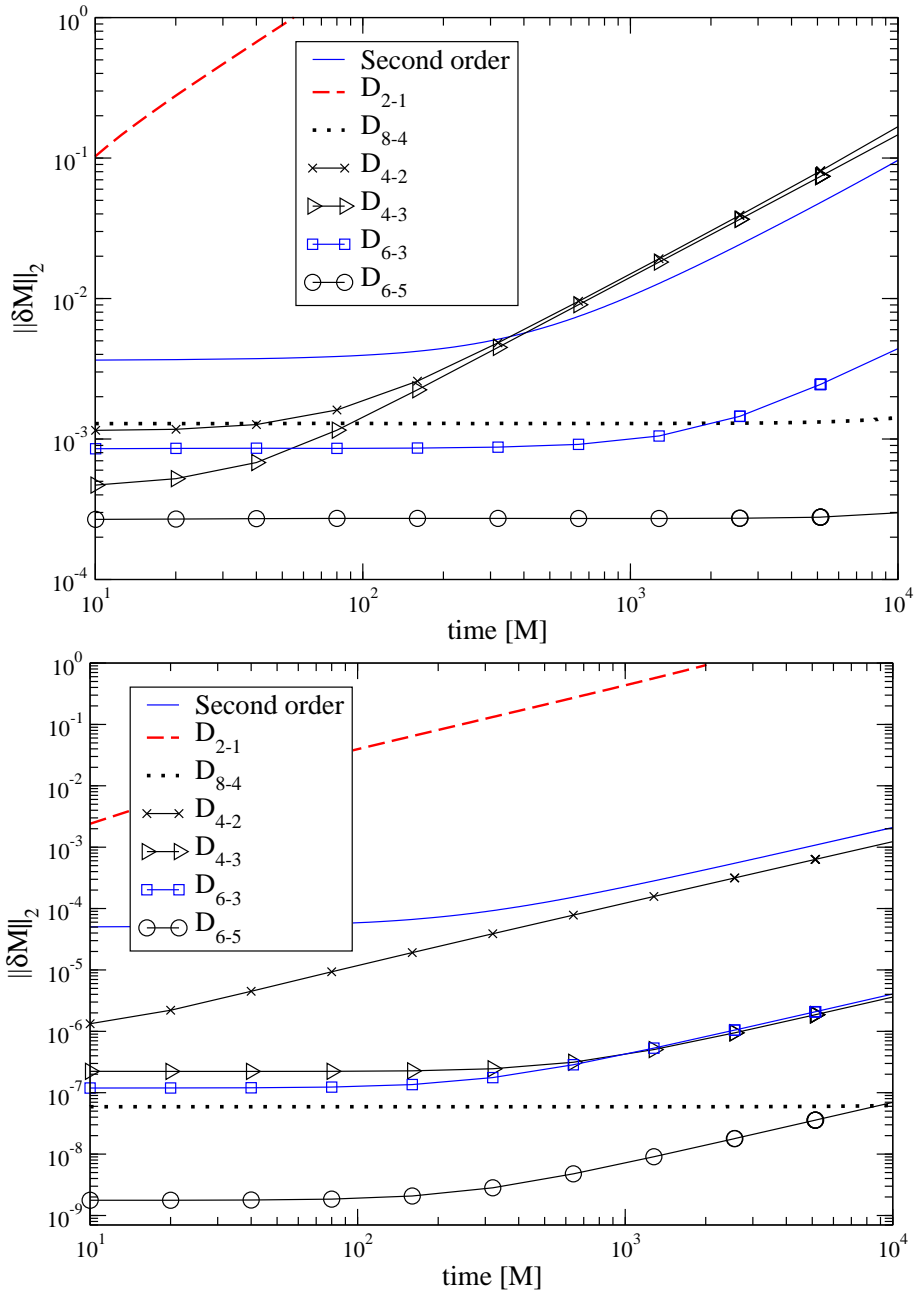
Figure 2.1: Time evolution of the relative error in the Misner-Sharp mass function when evolving a Schwarzschild black hole in Painlevé-Gullstrand coordinates with one grid patch, for different discrete methods. Two resolutions are displayed, corresponding to $\Delta r = M/8$ (upper panel) and $\Delta r = M/64$ (lower panel). The result from the method presented Ref. [47] is denoted by "second order", while new results are marked by the SBP derivative and dissipation operators used. The high-order operators D_{6-5} and D_{8-4} display superior performance already at the lowest resolution.

the black hole, and consequently ill-posedness of the continuum problem. While this migration could be theoretically avoided by choosing horizon-fixing dynamical coordinate conditions, a solution with this magnitude of error is, in any case, not of practical use.

In the present numerical code, the SBP operators are also used as one-sided derivatives for determining the constraint-preserving boundary conditions, which suggests that the operator D_{2-1}, which is only first order at the boundaries, will yield less accurate outer boundary conditions than the third order method in [47]. Figure 2.1 clearly demonstrates this fact. However, the operators D_{6-3}, D_{6-5} and D_{8-4} are significantly more accurate than the results presented in Ref. [47], and already so at the coarsest resolution. Furthermore, at $\Delta r = M/64$ the SBP operator D_{6-5} induces a solution error of less than 10^{-7} (that is, *four orders of magnitude smaller than the corresponding errors when using the second order method of [47] with the same resolution*) within $10,000M$, which appears sufficiently accurate for many practical purposes.

The long-term evolution of a Schwarzschild black hole with the operators D_{6-5} and D_{8-4} is displayed in Figure 2.2. The linear growth of errors dominates the solution at late times, but since this error significantly decreases with resolution, long evolution times can be obtained even for moderate radial grid spacings. This is naturally an interesting feature for simulations with three-dimensional spatial grids, where computational resources are still a viable concern.
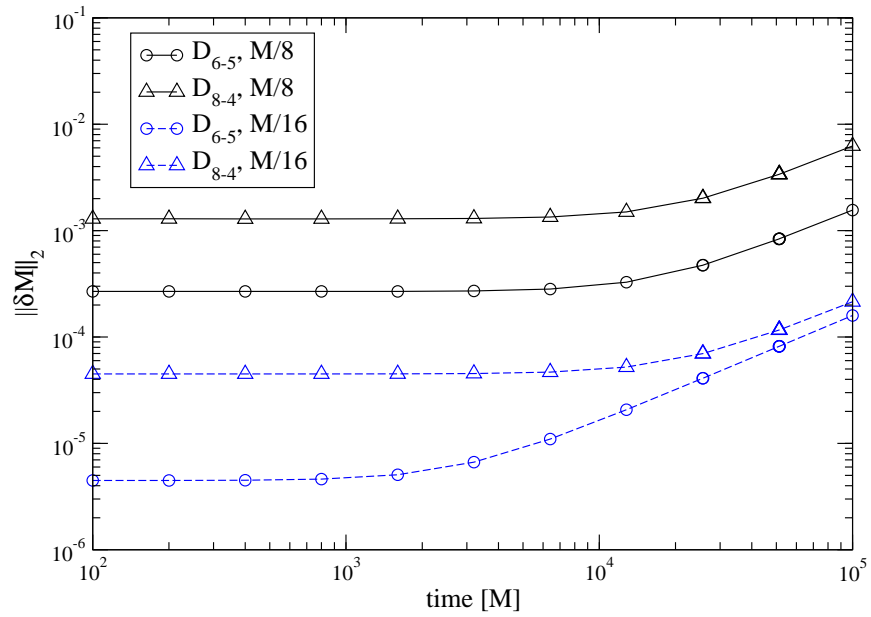
Figure 2.2: Evolution of a Schwarzschild black hole for $100,000M$. The axes show the quantities described in Figure 2.1. It is clear that even with low resolutions of $\Delta r = M/8$ and $M/16$, the operators D_{6-5} and D_{8-4} are able to evolve the black hole in a stable manner for a significant time.

2.3.1.2 Two grid patches

As dicussed in the introduction, the use of multiple coordinate patches has advantages when modeling black holes. To implement a stable interface boundary condition, the penalty method is used to ensure linear stability. Here we first investigate the performance of the SBP operators coupled to an inter-patch penalty boundary method by evolving a black hole spacetime covered by two non-intersecting spherical shells, the first one from $r = 1M$ to $r = 5.5M$, and the second one from $r = 5.5M$ to $r = 10M$. In order to provide an intermediate test towards the CPM tests below, we do a non-linear matching, communicating all characteristic modes (that is, without imposing for the moment constraint-preserving boundary conditions at the matching interfaces).

The free parameter of the penalty boundary condition δ introduced in section 2.2.3 is set to the dissipative value 0. Only the operators D_{6-5} and D_{8-4} are used for comparison to the results from the previous section.

In Figure 2.3 the performance of the multi-patch system is compared to the uni-patch results from the previous section. As expected, the use of one-sided derivatives at the inter-patch boundary reduces the total level of accuracy, but in a very small amount; furthermore, the system is still stable and convergent. The time of the onset of the linear growth observed in all evolutions varies between the grid setups and choices of discrete operator. Figure 2.4 shows the 3-metric component $g_{rr}(r)$ at the times $t = 0$ and $t = 10,000M$. The region around the inter-patch interface at $r = 5.5M$ is shown in the inset, which demonstrates that the penalty method

27
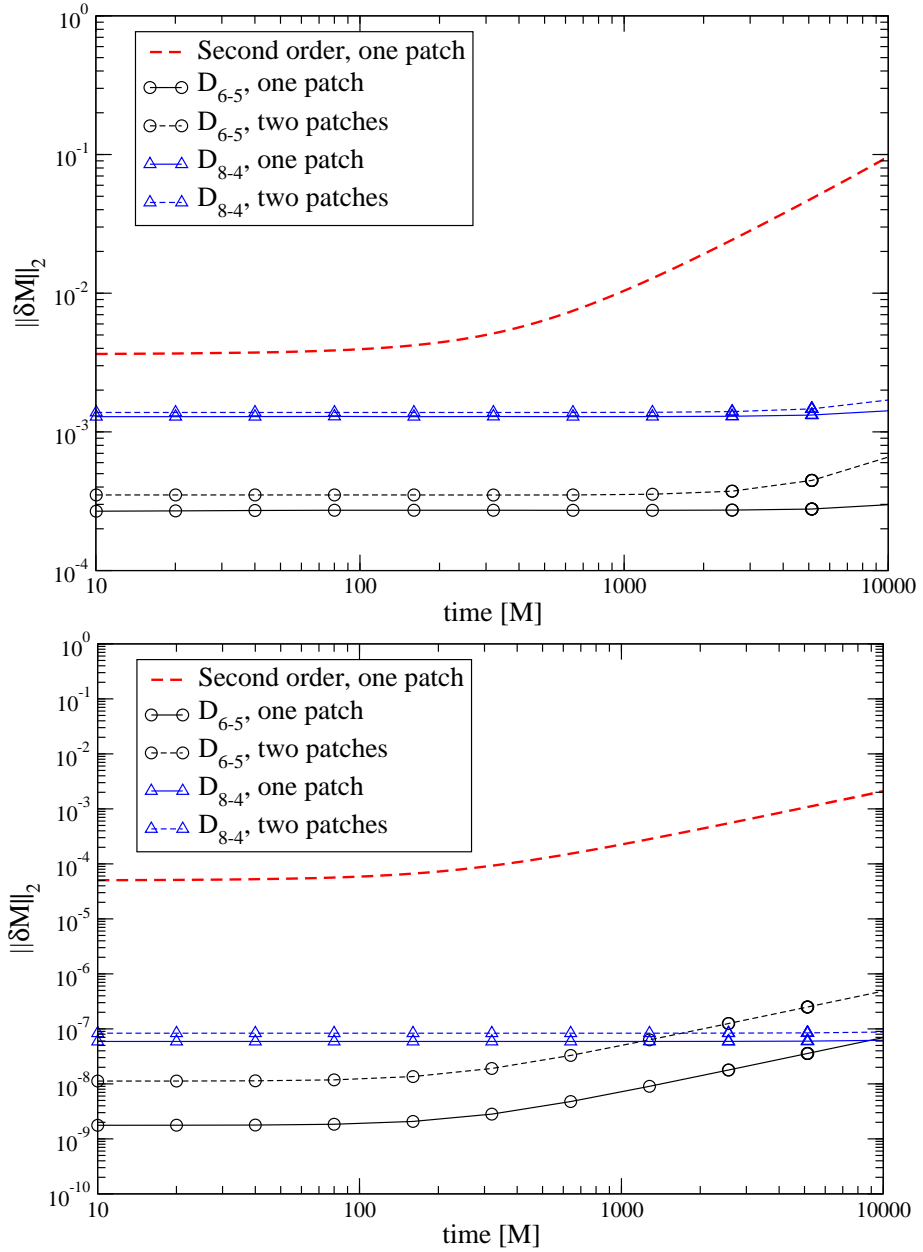
Figure 2.3: Comparison of uni-patch and multi-patch evolutions of a Schwarzschild black hole in Painlevé-Gullstrand coordinates. The graphs denoted by "one patch" and "second order" are those from Figure 2.1, while the corresponding graphs for "two patches" cover the computational domain with two non-intersecting spherical shells, the first one from $r = 1M$ to $r = 5.5M$, and the second one from $r = 5.5M$ to $r = 10M$. The one-sided derivatives at the interface boundary introduce a very small loss of accuracy. In the upper and lower panels the resolution is $\Delta r = M/8, M/64$, respectively. For the late time behaviour of D_{6-5} and D_{8-4} please also cf. Figure 2.2.
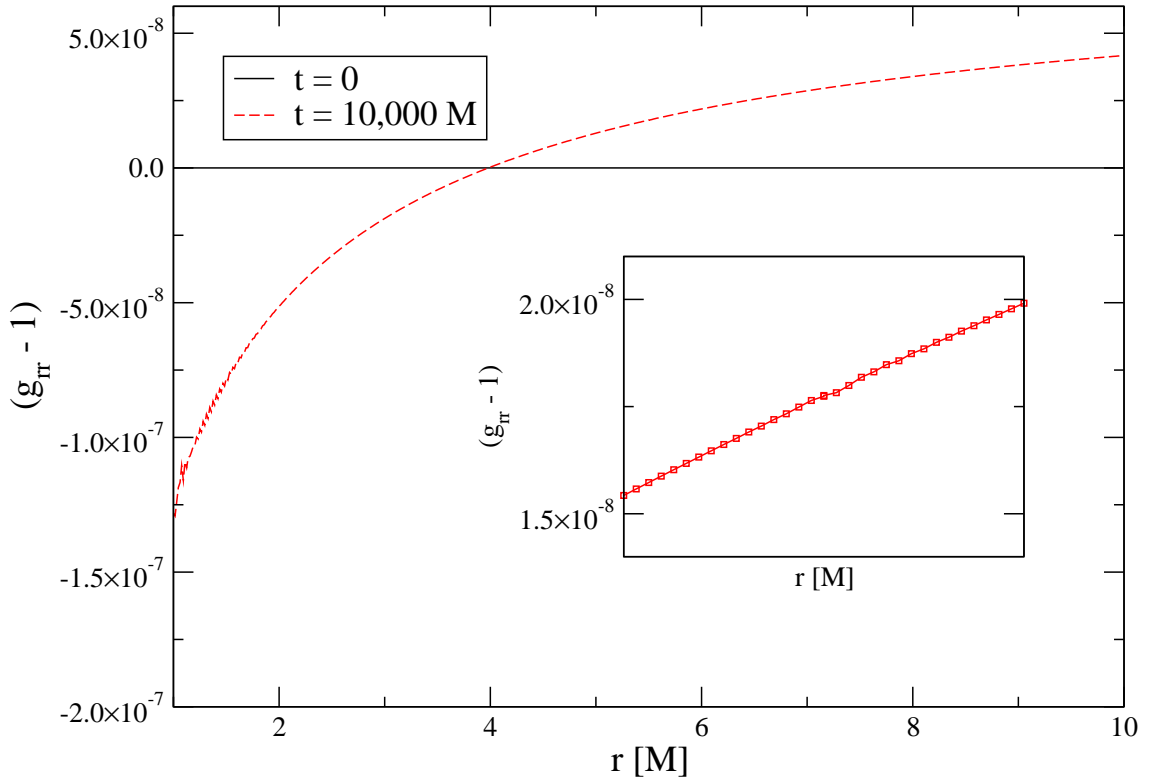
Figure 2.4: Evolution of metric function g_{rr} for a black hole in Painlevé-Gullstrand coordinates, with a resolution of $\Delta r = M/64$, two grid patches with an interface at $r = 5.5M$ and using the SBP operator D_{6-5}. The two graphs show the metric function at $t = 0$ (where $g_{rr}(r) = 1$) and at $t = 10,000M$. The inset shows the region around the interface between the grid patches.

introduces no strong visible artifacts in this part of the solution. This observation also holds for the other solution functions.

2.3.2   Gauge wave on a Schwarzschild background

The next series of tests focuses on a dynamical situation, namely the evolution of a Schwarzschild black hole in non-stationary coordinates. For this purpose, the initial data is set to a Schwarzschild black hole in Painlevé-Gullstrand coordinates as in section (2.3.1), as is the lapse and shift function at all times, but the incoming gauge mode u_3 at the outer boundary is set to a Gaussian pulse of the form

$$u_3(t) = u_3^{PG}(1 + Ae^{-(t-t_0)^2/\tilde{\sigma}^2}). \tag{2.4}$$

Here, u_3^{PG} is the exact gauge mode from the stationary solution. As in Ref. [47], we impose a strong pulse with $A = 1$, $t_0 = 5M$ and $\tilde{\sigma} = 2M$. Since the solution is now not adapted to the asymptotically timelike Killing field, the SBP operators and multi-patch techniques can be tested on a solution with wave propagation without compromising the use of the error measure $||\delta M||_2$. To facilitate comparison with Ref. [47], the outer boundary is located at $r = 30M$ in these tests.

Figure 2.5 shows results from the gauge pulse problem on a single grid patch and two grid patches, here with an inter-patch boundary at $r = 15.5M$. While in the stationary case the inter-patch boundary method only had to deal with small numerically introduced differences between the values of the geometrical quantities at the interface, the non-stationary case introduces a large pulse travelling over the bound-
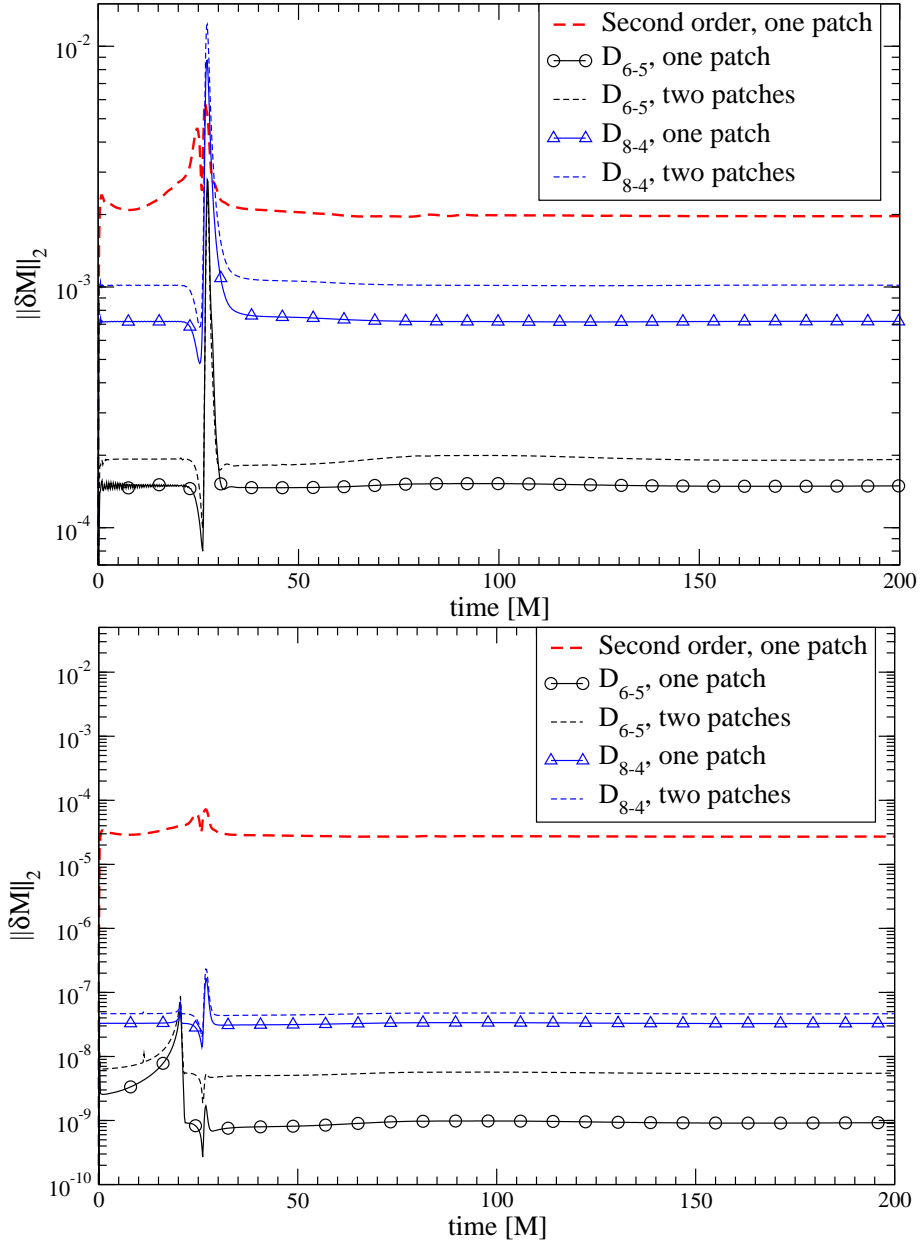
Figure 2.5: Comparison of uni-patch and multi-patch evolutions of a gauge wave travelling on a Schwarzschild background. The graphs denoted by "second order" are obtained with the methods in Ref. [47], while the corresponding graphs for "one patch" and "two patches" cover the computational domain with either one or two non-intersecting spherical shells, the first one from $r = 1M$ to $r = 15.5M$, and the second one from $r = 15.5M$ to $r = 30M$. The one-sided derivatives at the interface boundary introduce a small loss of accuracy, but the system is still stable. The upper and lower panels correspond to $\Delta r = M/8, M/64$, respectively.

31

ary, and is thus a much more severe test for accuracy and stability of the penalty method. The solution error is dominated by the ability of the discrete method to represent the propagation and accretion of the gauge pulse, and by possible artefacts introduced by the inter-patch boundary.

Judging from Figure 2.5, the high-order operators are stable and significantly more accurate than a second order method also in a dynamical situation, and even when using multiple matched domains.

2.3.3 Accretion of a scalar field pulse

Since the outer boundary has two free incoming modes, it is possible to inject a scalar field pulse in a way similar to the gauge pulse of section (2.3.2). In contrast to the gauge pulse, however, this system will result in an increase of mass of the black hole, which also implies that the Misner-Sharp mass cannot be used as a measure of the errors anymore. A possible choice for a gauge field source with compact support is

$$
u_8(t) = \begin{cases} 0 & t < t_I \\ \frac{A}{t_F^8}(t - t_I)^4 (t - t_F)^4 \sin(\frac{\pi t}{t_F}) & t \in [t_I, t_F] \\ 0 & t > t_F \end{cases}
$$

To facilitate comparisons with Ref. [47] we use an amplitude $A = 7.2$, and $t_I = 0M$, $t_F = 10M$ and set the computational domain to be $r \in [1, 50]M$.

For resolutions $\Delta r = M/20$ and $\Delta r = M/40$, the time evolution of the apparent horizon is shown in Figure 2.6. The scalar pulse leads to a significant increase

32
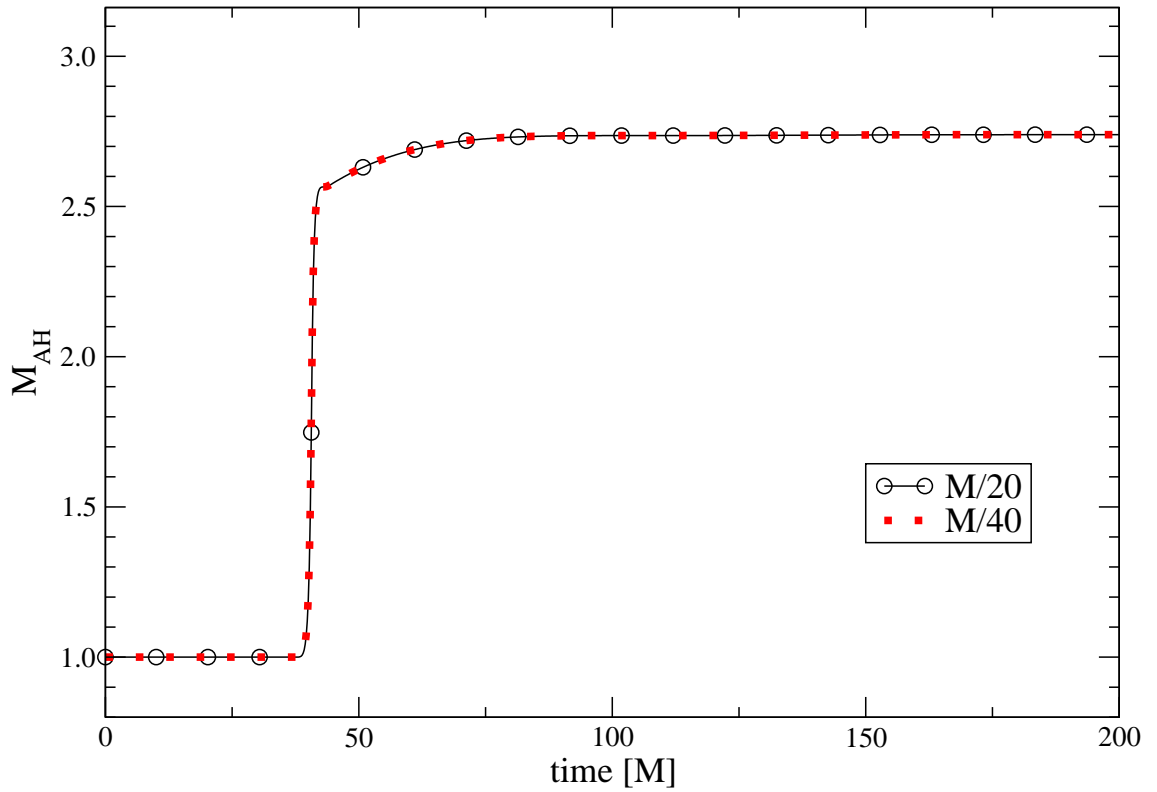
Figure 2.6: Evolution of the apparent horizon mass for the accretion of a strong scalar pulse to a Schwarzschild black hole. Shown are plots for two resolutions, $\Delta r = M/20$ and $\Delta r = M/40$, using the SBP operator D_{6-5}. The large scalar field amplitude leads to a significant increase in the black hole mass.

in the black hole mass by a factor of ≈ 2.7 after the pulse is inside the black hole. Larger amplitudes are not obtainable with the simple gauge prescription used here, but a horizon-freezing gauge condition could improve on this result. As a replacement for the Misner-Sharp error measure, we plot the L_2 norm of the Hamiltonian constraint over time in Figure 2.7. It is apparent that the high-order operators are again stable and more accurate than the second order operator. The graphs indicate a growth of the constraint near $t = 200M$, but a long-term evolution with $\Delta r = M/20$ shown in Figure 2.8 demonstrates that the system settles down to stability after the accretion.

2.3.4 Robust stability test with gauge noise

The term *robust stability test* [164, 12] typically refers to the discrete stability of a numerical system in response to random perturbations. In this case, we will use the same system as in section (2.3.1.2), but impose random noise on the incoming gauge mode u_3 with a certain amplitude. To test the discrete stability of the evolution system, we chose a large range of amplitudes from 10^{-4} to 0.3. Random perturbations of the latter amplitude is significant for a non-linear system[5].

For this multi-patch test, results in the mass error for a resolution $\Delta r = M/8$ are shown in Figure 2.9. It is apparent that strong random noise induces a stronger

---

[5]Beyond this amplitude the inner boundary tends to become partially inflow by moving the apparent horizon beyond the computational domain. More sophisticated gauge or inner boundary condition could alleviate this, but since we are interested here in a proof of principle, a simple system is preferred.
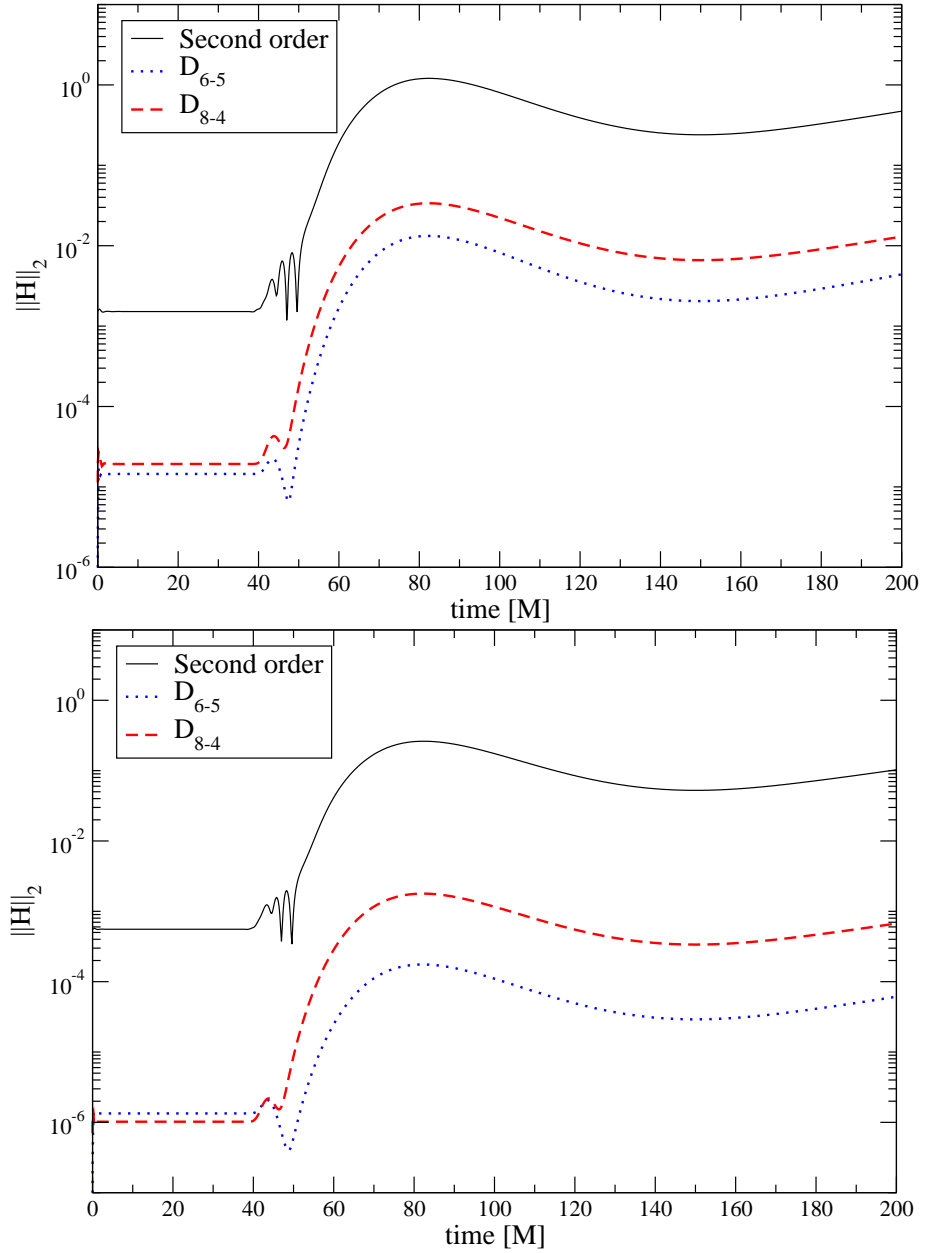
Figure 2.7: L_2 norm of the Hamiltonian constraint over time for the accretion of a strong scalar field pulse to a Schwarzschild black hole, with resolutions $\Delta r = M/20, M/40$ (upper and lower panels, respectively). The graph denoted by "second order" is obtained with the method presented in [47], and the D_{6-5} and D_{8-4} are obtained using the corresponding SBP operators.
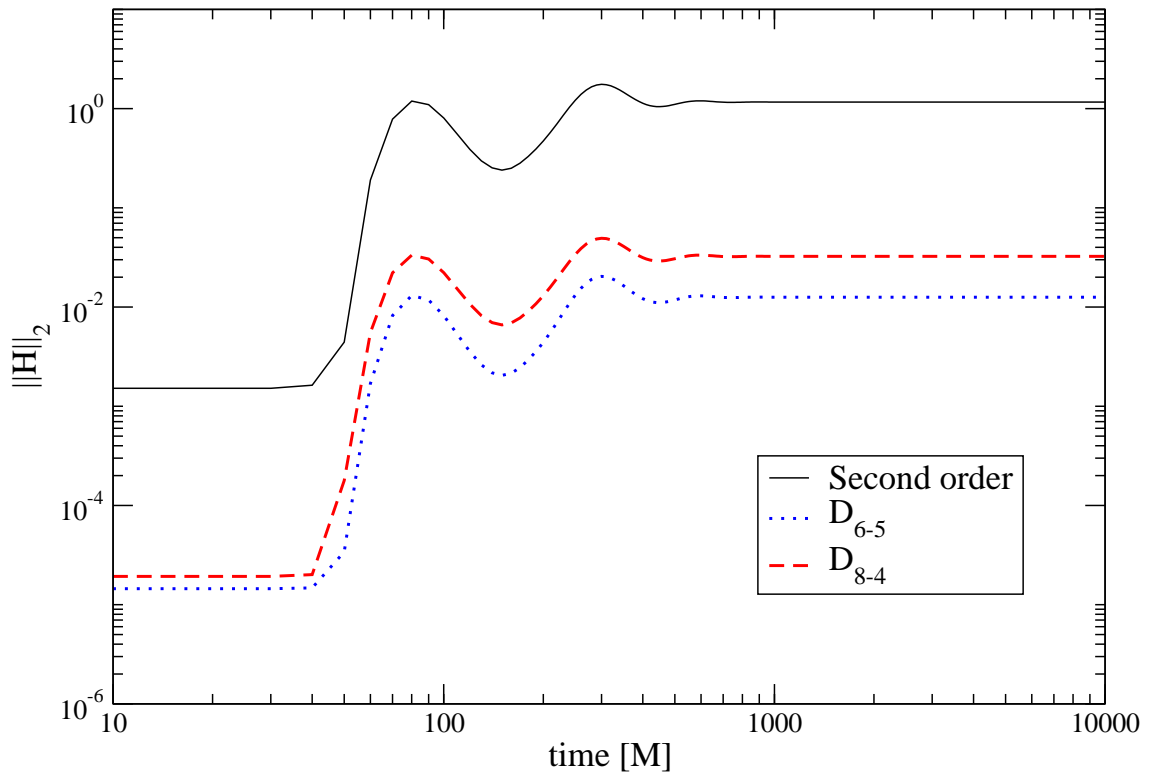
Figure 2.8: As Figure 2.7, but evolved for 10,000 M with $\Delta r = M/20$ to demonstrate the long-term behaviour after accretion of the pulse.
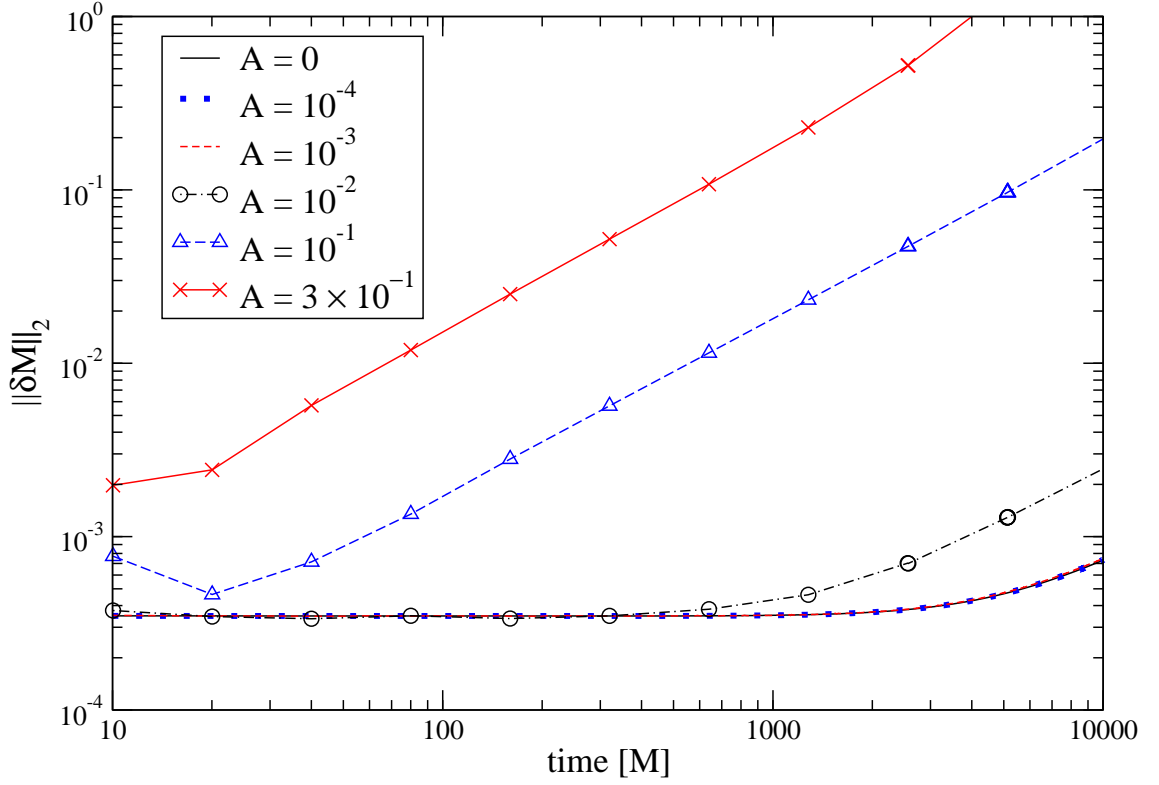
Figure 2.9: Results of a robust stability test for different random noise amplitudes. The system is a Schwarzschild black hole in Painlevé-Gullstrand coordinates, and the computational domain $r \in [1, 10]M$ is covered by two patches with a boundary at $r = 5.5M$ and a resolution of $M/8$. Random noise is superimposed on the ingoing gauge mode u_3, with an amplitude denoted by A. The graphs show the mass error with time for different random noise amplitudes, obtained with the SBP operator D_{6-5}.
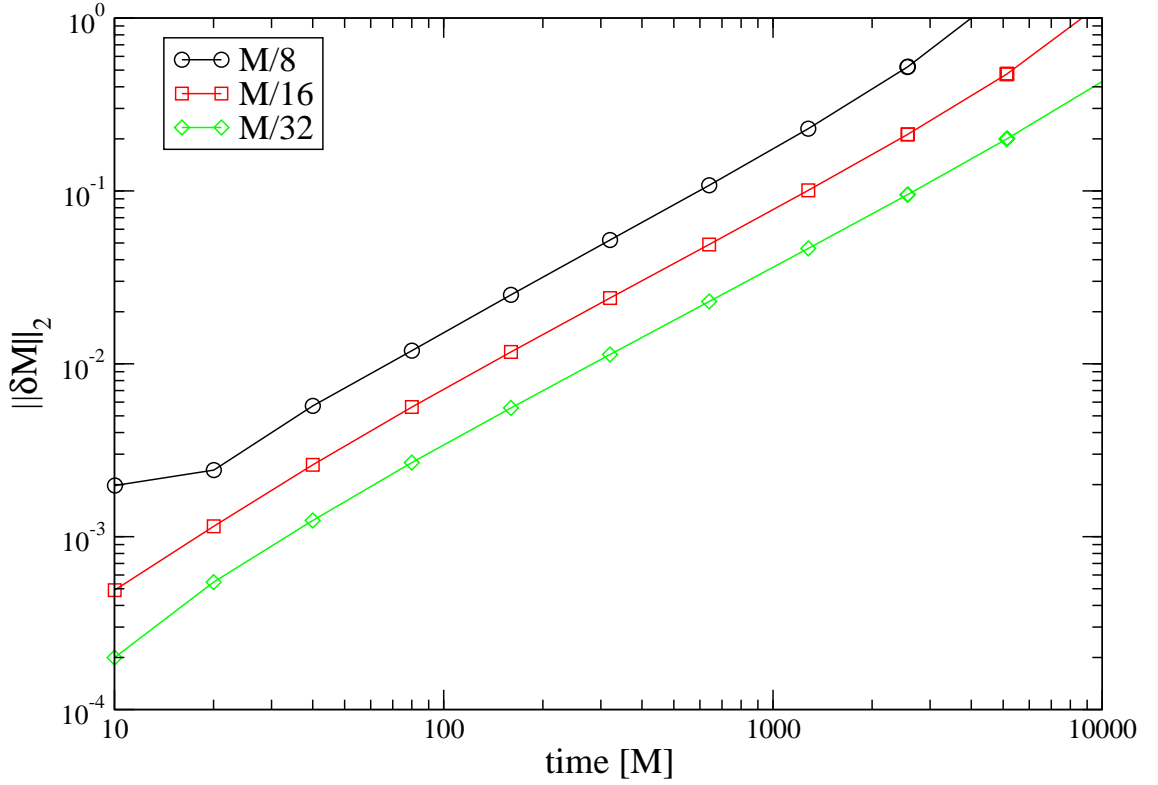
Figure 2.10: Like Figure 2.9, but for the highest random noise amplitude 0.3 and different resolutions.

growth in the solution error. However, this growth is still linear. As in all black hole evolutions in section 2.3.1, the system encounters a numerical instability as the solution error approaches 1, but this is not a consequence of the random noise, but of the inner boundary becoming partially inflow due to a coordinate motion of the apparent horizon. Also, with increasing resolution, the growth rate of the error does not increase, as shown in Figure 2.10. We conclude that this high-order evolution system is discretely stable against strong random perturbations.

2.3.5 Cauchy–perturbative matching: robust stability test with scalar field noise

We now test the stability of the system with Cauchy–perturbative matching against random perturbations in the scalar field. To this end, the computational domain is again subdivided as in section 2.3.4, but the right patch evolves the scalar field on a fixed Painlevé-Gullstrand background as explained in the introduction. The interpatch boundary is thus matching the Cauchy patch to a perturbative one, and we test the stability of the system against random perturbations by imposing random noise on the incoming scalar field mode on the outer boundary of the perturbative patch.

Since the mass error is not available for a system accreting a scalar field, the L_2 norm of the Hamiltonian constraint is used again in Figure 2.11. No exponential growth can be observed in the Hamiltonian constraint violation. The same is true when increasing the resolutions, as in Figure 2.12, which also deserves some additional comments: The robust stability test does not lead to a converging sequence of solutions if the random noise amplitude is not diminished with resolution. However, the purpose of these tests is to excite any unstable high frequency modes present in the numerical system. The absence of any mode growing with increasing resolution shows that the system with a Cauchy–perturbative matching interface is stable even against strong random noise injected into the system. This is a promising result for any effort to do three-dimensional matching between Cauchy modules and perturbative ones using multiple patches and high-order summation-by-parts operators.
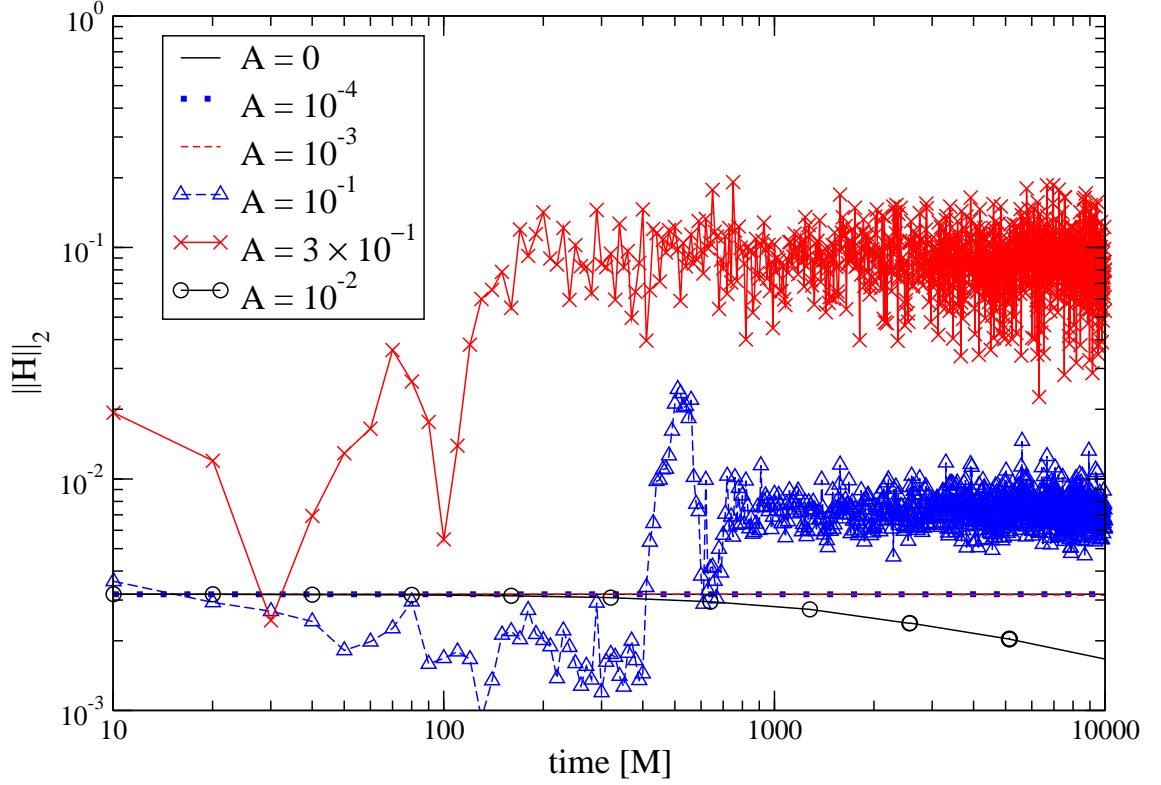
Figure 2.11: Robust stability test with Cauchy–perturbative matching. The system is a dynamically evolved Schwarzschild black hole in Painlevé-Gullstrand coordinates matched to a perturbative module at $r = 5.5M$ as described in the introduction. Random noise is imposed via the incoming scalar field mode at the outer boundary. Plotted is the L_2 norm of the Hamiltonian constraint over time for different noise amplitudes. All evolutions were done with a resolution of $\Delta r = M/8$ and the SBP operator D_{6-5}.
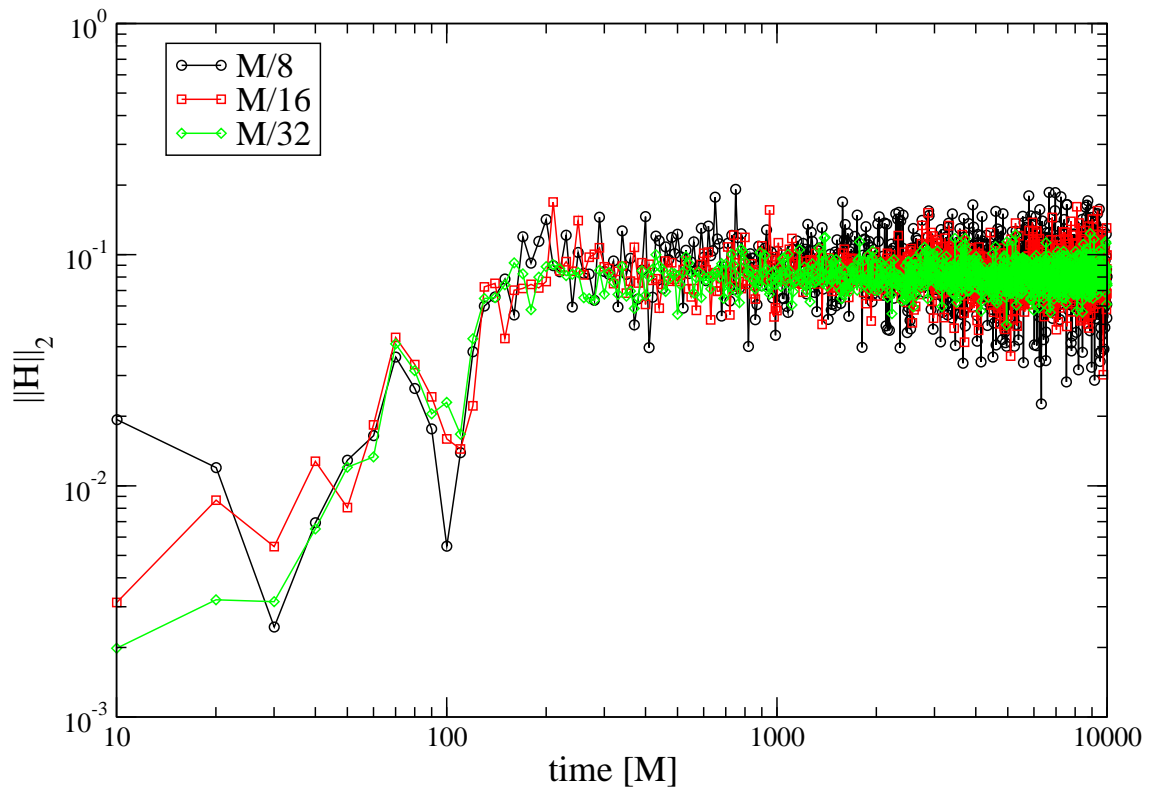
Figure 2.12: Like Figure 2.11, but for the highest random noise amplitude and different resolutions.

2.3.6 Cauchy–perturbative matching: Accretion of a "gravitational wave" and long-term evolution

Finally, using the massless Klein-Gordon field as a scalar analogue of gravitational waves in spherical symmetry, we model the accretion of a gravitational wave packet across a Cauchy–perturbative matching boundary. This test is an extension of the single-patch scalar field accretion of section 2.3.3, and makes use of all ingredients presented so far for a stable and accurate evolution of black holes with Cauchy–perturbative matching.

Since Cauchy–perturbative matching assumes the gravitational wave to be a small perturbation of a fixed background in the wave zone, the amplitude of the wave packet that we inject through the outermost boundary is chosen to be $A = 0.01$. Similarly to section 2.3.3, we describe the packet by the function

$$u_8(t) = \begin{cases} 0 & t < t_I \\ \frac{A}{t_F^8}(t - t_I)^4(t - t_F)^4 \sin(\frac{\pi t}{n t_F}) & t \in [t_I, t_F] \\ 0 & t > t_F \end{cases}$$

where for the number of half waves in the pulse we set $n = 100$. We inject the packet from $t_I = 0$ to $t_F = 100M$. The plots in Figure 2.13 display the the evolution of the grid function Φ, and specifically the behaviour of the function around the Cauchy–perturbative matching interface, which is at $r = 25.5M$. The corresponding increase in apparent horizon mass is shown in Figure 2.14. The evolution of the Hamiltonian constraint violation using the SBP operator D_{6-5} and different resolutions is shown in Figure 2.15. It is apparent that with the techniques used not only is the discrete

42
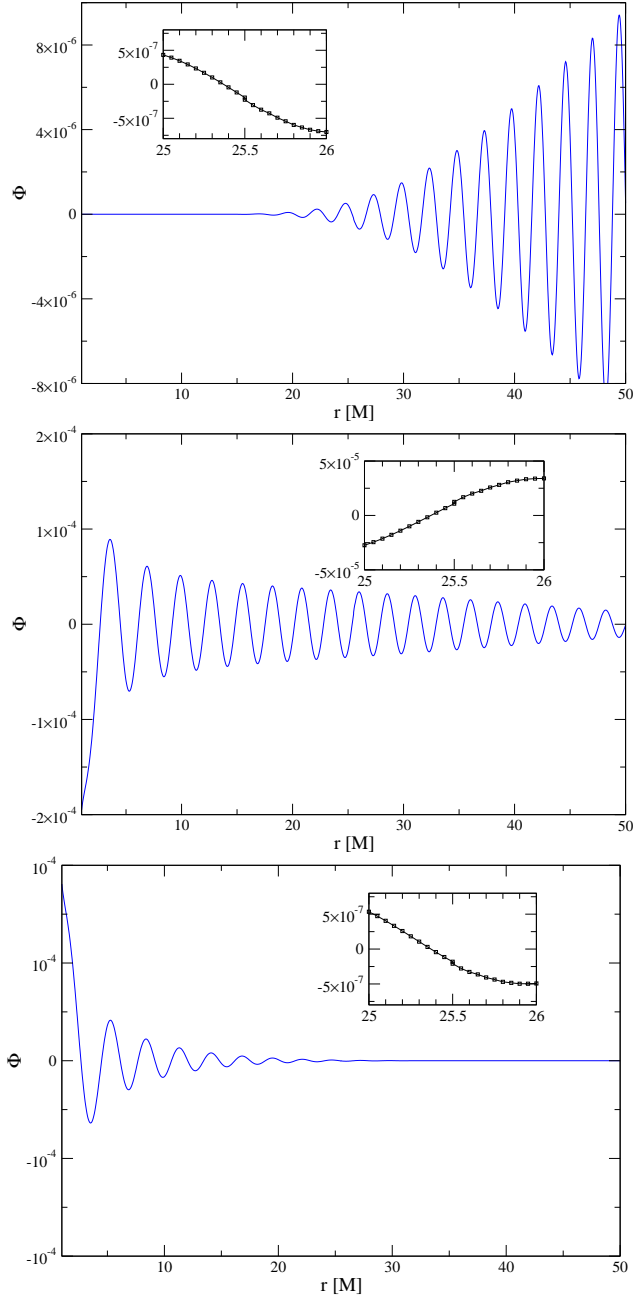
Figure 2.13: Accretion of a scalar wave packet across a Cauchy–peturbative match-
ing interface, as a scalar analog for gravitational wave accretion in three-dimensional
simulations. The packet consists of 50 waves injected from $t = 0$ to $t = 100M$, as
described in the text. Here, the grid function Φ is plotted over the radial coordi-
nate at $t = 30M, 65M, 110M$ (from top to bottom), for the resolution $\Delta r = M/20$
and the SBP operator D_{6-5}. The inset shows the behaviour of the grid function
around the matching interface, which is at $r = 25.5M$. Note that even though the
grid function is in principle two-valued on the interface, the penalties in conjunction
with high-order operators only lead to a very small mismatch.

43
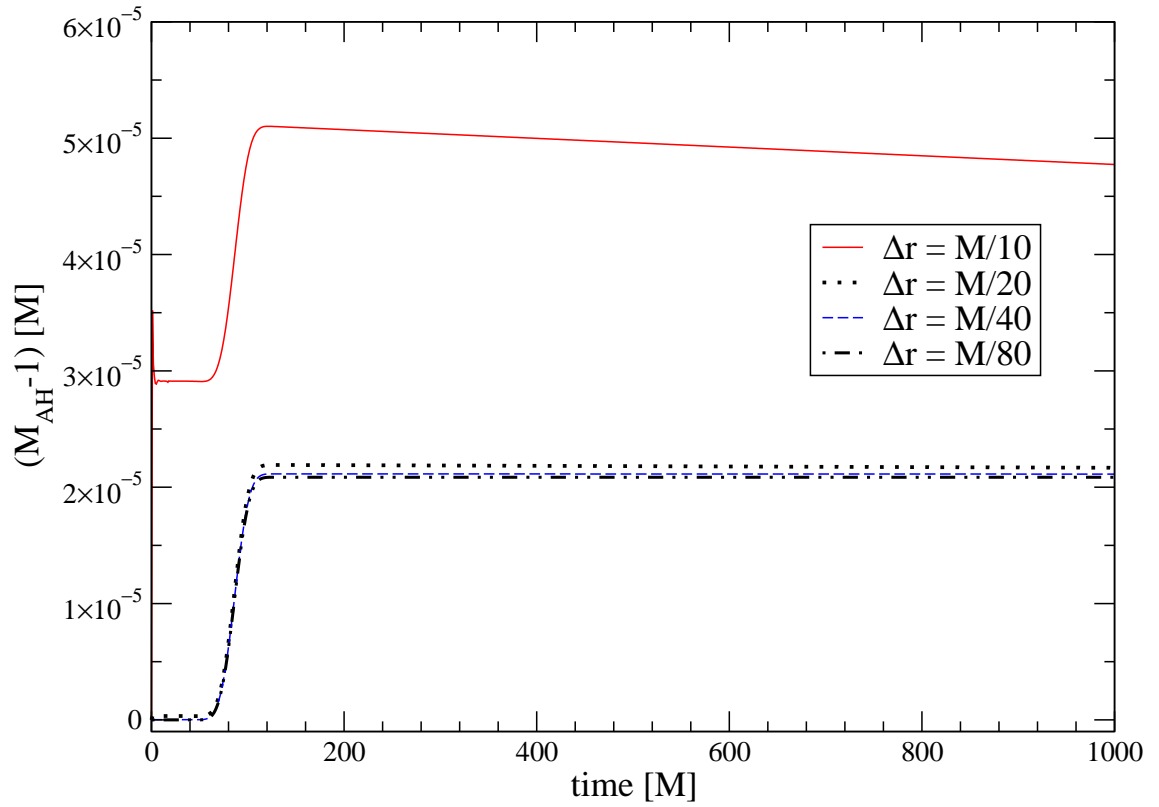
Figure 2.14: Accretion of a scalar wave packet across a Cauchy–peturbative matching interface. This plot shows the apparent horizon mass over time for evolutions with different resolutions and the SBP operator D_{6-5}.
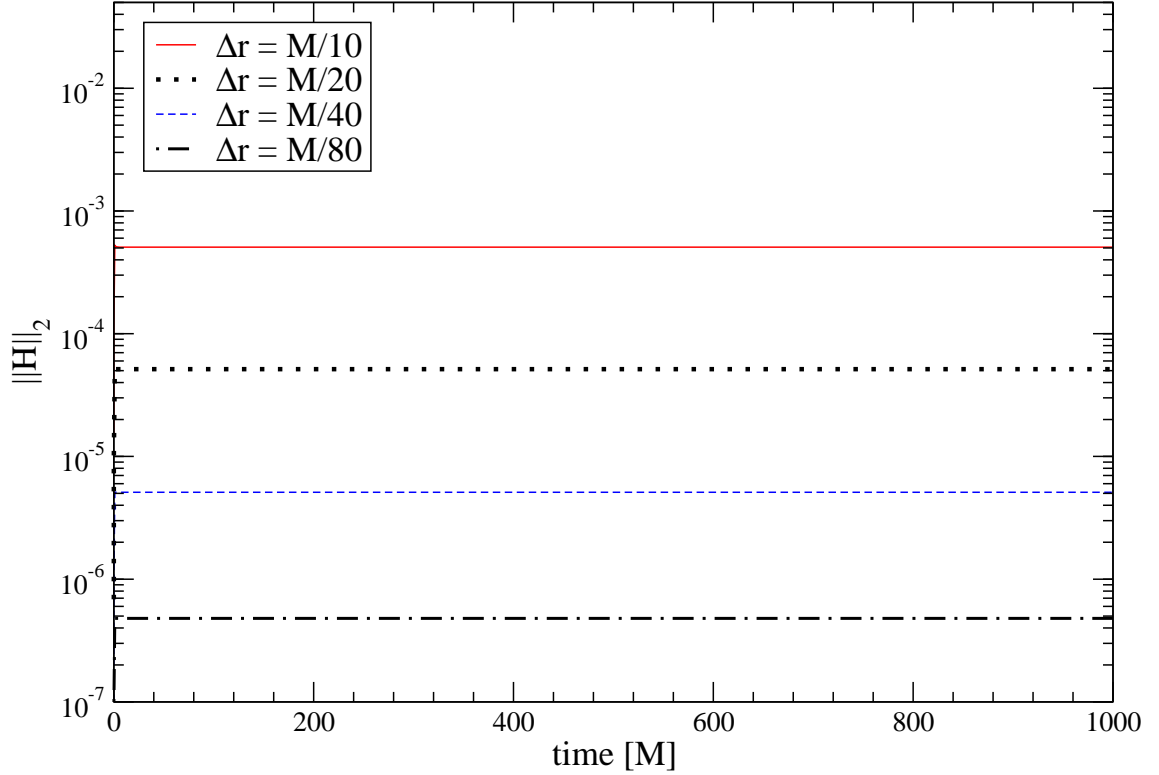
Figure 2.15: Accretion of a scalar wave packet across a Cauchy–peturbative matching interface. This plot shows the L_2 norm of the Hamiltonian constraint for different resolutions, using the SBP operator D_{6-5}. *The non-linear constraint violations introduced at the continuum by the matching are small enough that they cannot be detected in these very accurate simulations.* Please note, for comparison with Figure 2.8, that the amplitude of the Klein-Gordon signal is smaller compared to section 2.3.3.
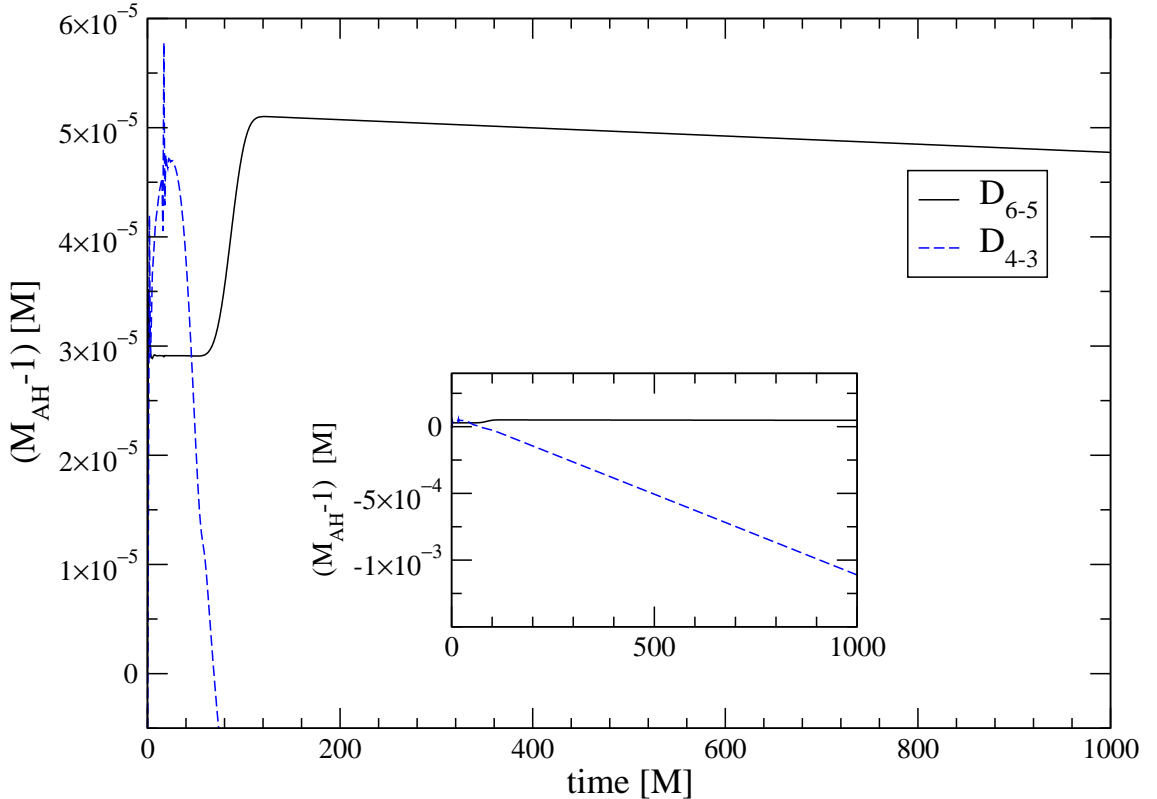
Figure 2.16: Accretion of a scalar wave packet across a Cauchy–peturbative matching interface. To demonstrate the advantage of using high-order methods, $(M_{AH}-1)$ is shown for evolutions obtained with the SBP operators D_{4-3} and D_{6-5}, with resolution $\Delta r = M/10$. The loss of mass after accretion of the wave packet with compact support in $t \in [0,100]M$ is a numerical artefact, which converges away with resolution. The inset shows that the evolution obtained with the operator D_{4-3} is not unstable, but only significantly less accurate.

system stable and accurate, *but also the amount of non-linear constraint violations introduced at the continuum by the Cauchy–perturbative matching are very small*, in Figure 2.15 they must actually be smaller than 10^{-6}.

The advantages of using high-order methods is made evident in Figures 2.16, 2.17, 2.18, and 2.19. In these plots, the performance of the SBP operator D_{6-5}, which is sixth order in the interior and fifth order at the boundaries, is compared to that of the operator D_{4-3}, which is fourth order in the interior and third or-
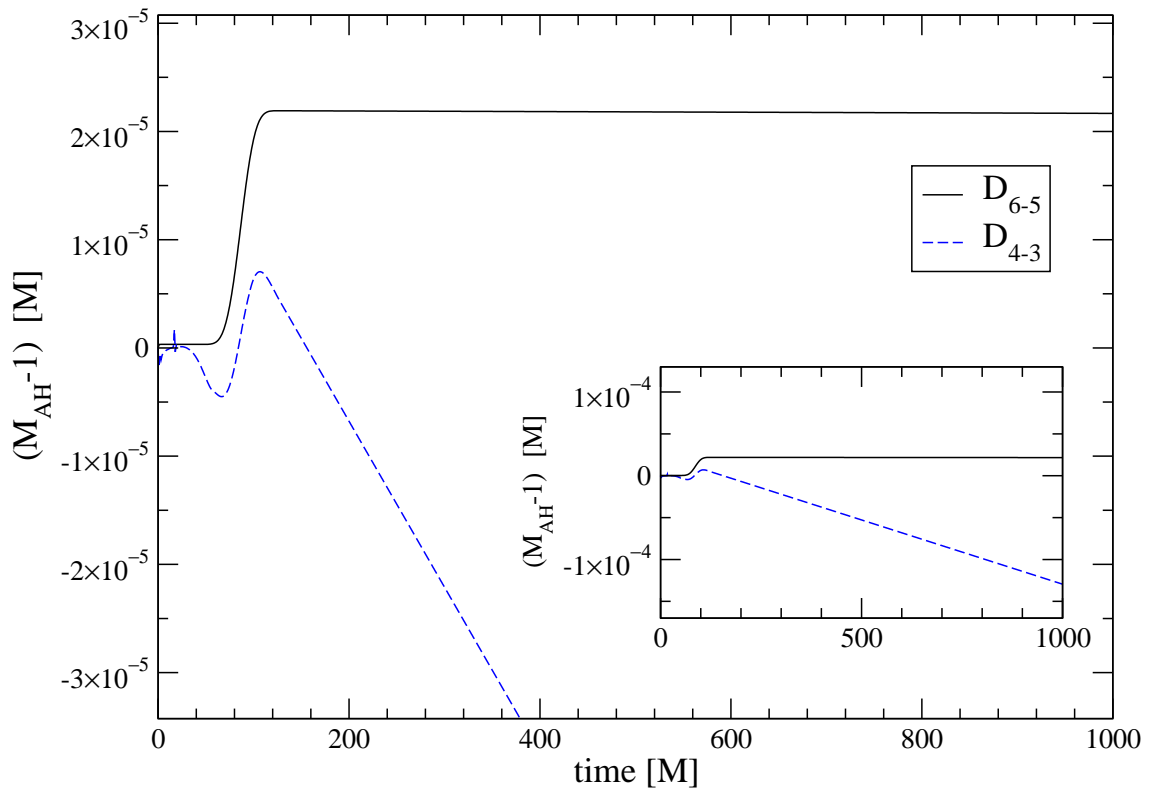
Figure 2.17: Like figure 2.16, but for a resolution of $\Delta r = M/20$.
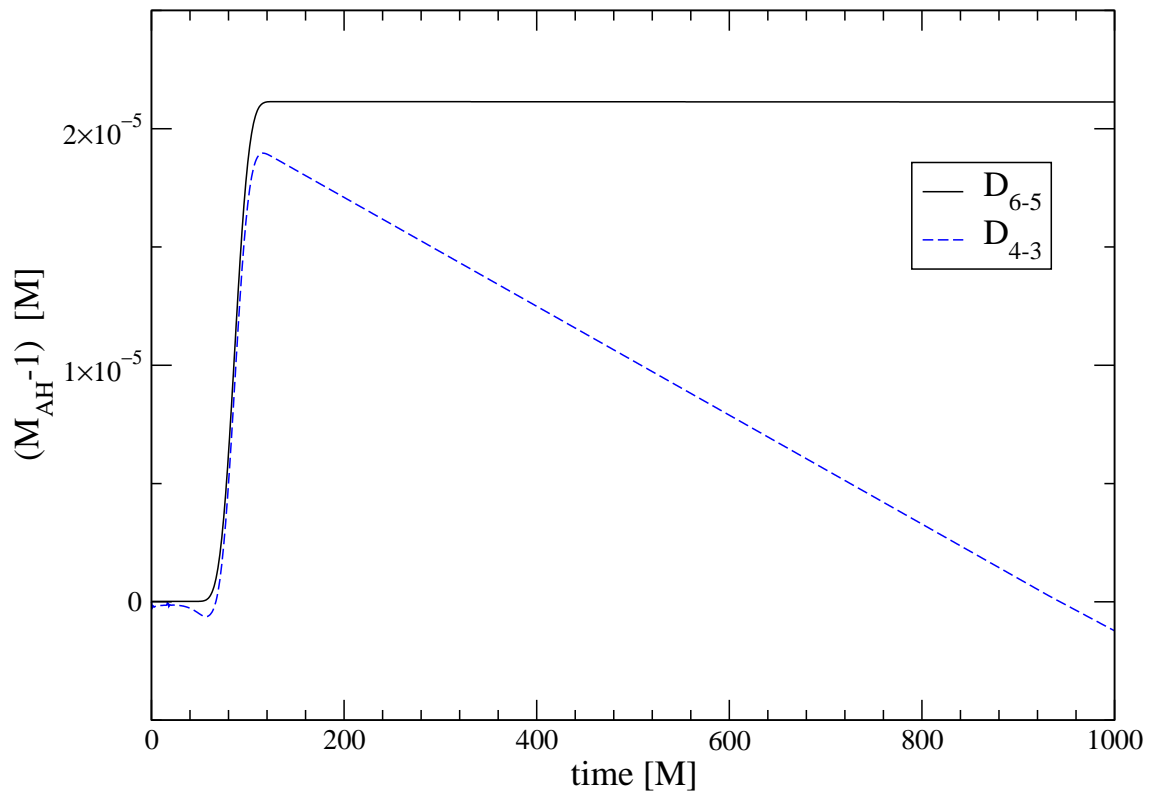
Figure 2.18: Like Figure 2.16, but for a resolution of $\Delta r = M/40$.
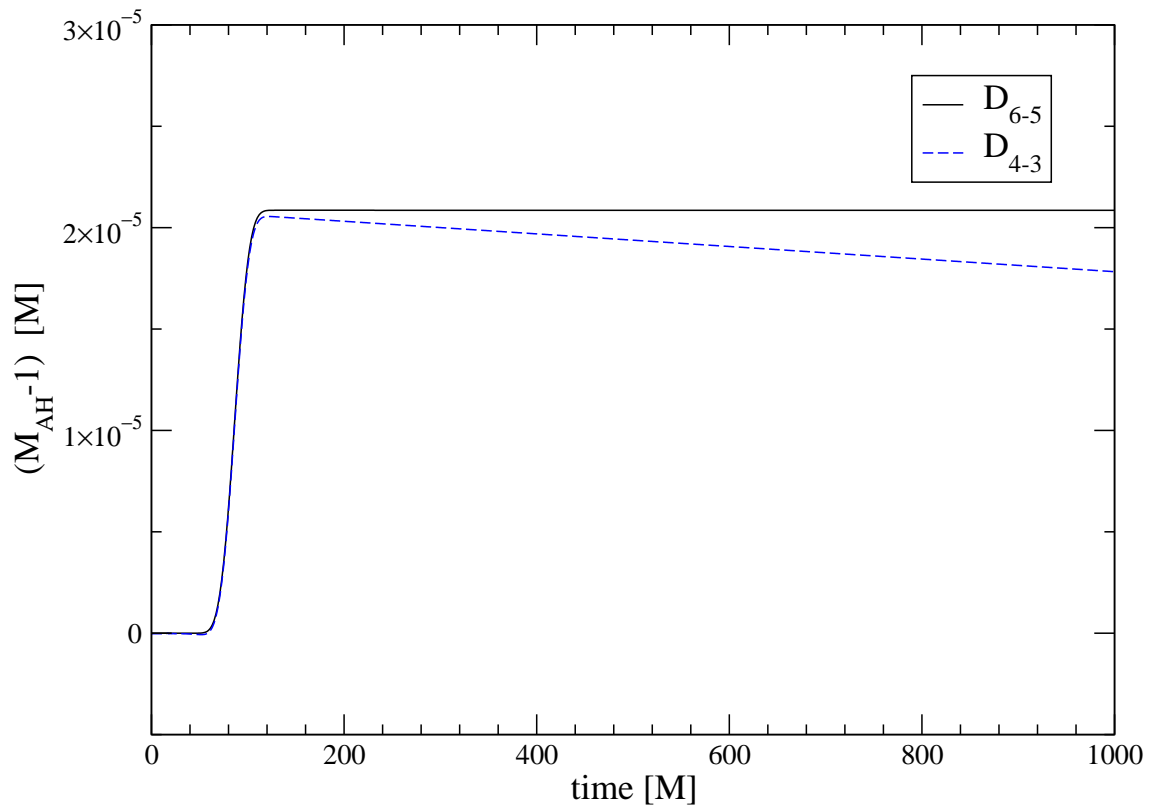
Figure 2.19: Like Figure 2.16, but for a resolution of $\Delta r = M/80$.

der at the boundaries, for different choices of resolution. Although both operators show convergence, for a mass increase of about 10^{-5}, the operator D_{4-3} is unable to reproduce the correct behaviour with reasonable grid resolutions. We consider this specifically important for three-dimensional simulations, where the necessary resources scale with n^4 if n denotes the number of grid points in each direction. Thus, for all simulations requiring a certain amount of precision, high-order operators are an essential requirement.

The long-term evolution of a Schwarzschild black hole accreting a wave packet over a Cauchy–perturbative matching interface and settling down to equilibrium is shown in Figure 2.20. The black hole is evolved for $1,000,000M$ with the lowest resolution $\Delta r = M/10$ and the SBP operator D_{6-5}. While an evolution of this length might appear to be of only technical interest, we note that modeling phenomena like hypernovae and collapsars in general relativity will require the stable evolution of a black hole for at least several seconds, which is the lower end of timescales associated with the collapsar model of gamma-ray burst engines [115]. For a stellar mass black hole, $M = M_\odot \approx 5\mu s$, that is $1s \approx 200,000M_\odot$.

2.4   Conclusions and outlook

To obtain long-term evolutions of compact astrophysical systems in three spatial dimensions, advanced numerical techniques are preferable in that they may improve stability and accuracy of the associated discrete model system. While high accuracy enables efficient use of the available computational resources, well-
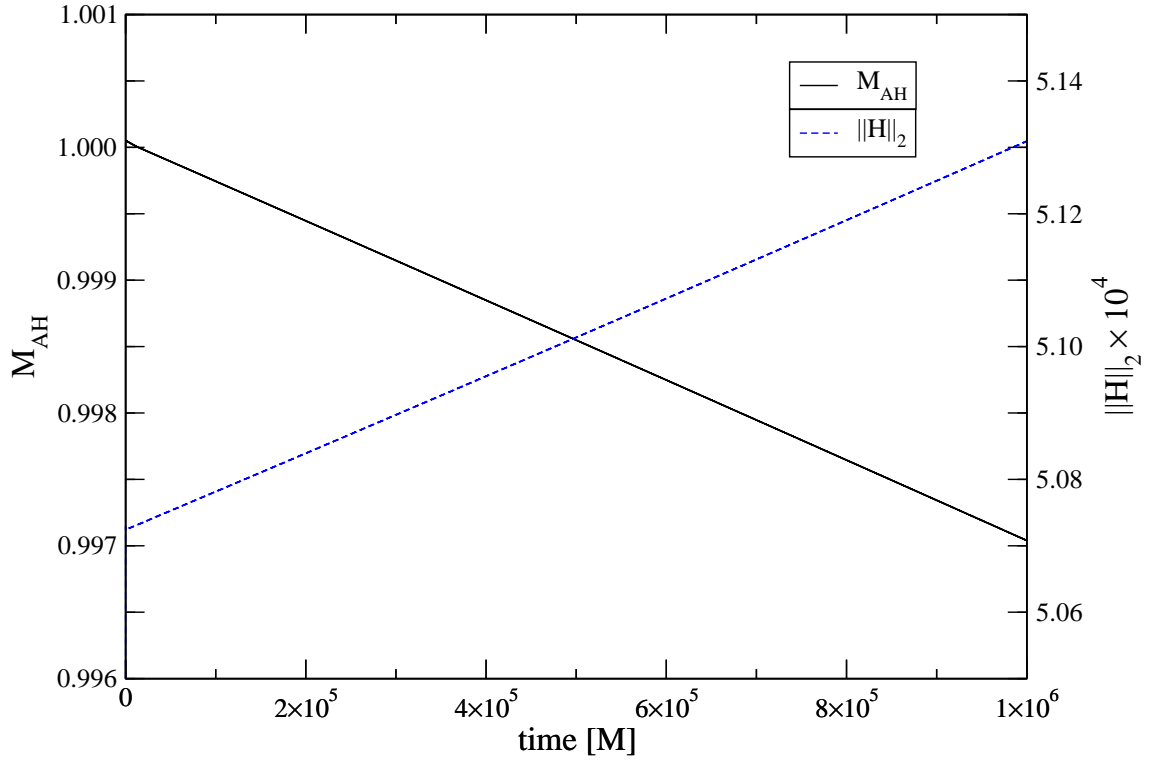
Figure 2.20: Long-term stable evolution of a Schwarzschild black hole after accretion of a scalar wave packet with Cauchy–perturbative matching. The SBP operator D_{6-5} is used with a resolution of $\Delta r = M/10$. Plotted are the apparent horizon mass and the Hamiltonian constraint over time. The apparent horizon mass indicates that the discrete evolution introduces a relative error of about 0.3% after $1,000,000M$.

posedness of the continuum model and numerical stability are requirements which can not be met by increasing computational power. A number of techniques have been suggested to address these issues [112]: Multiple coordinate patches, typically adapted to approximate symmetries of certain solution domains, combined with high-order operators are expected to increase the accuracy of any model of a stellar system. Cauchy–perturbative matching provides an efficient way to accurately model the propagation of gravitational waves to a distant observer, and to yield physical boundary conditions on incoming modes of the Cauchy evolution. Constraint-preserving boundary conditions isolate the incoming modes on the constraint hypersurface, and, finally, for evolving black holes, an excision boundary is desirable to concentrate on the behaviour of the external spacetime. Only recently the consideration of the well-posedness of the differential system and the application of theorems on discrete stability of the numerical system have provided hints for how to address the outstanding issues. In this study, we have applied all these techniques to a model system: a spherically symmetric black hole coupled to a massless Klein-Gordon field.

We find that the use of a first-order hyperbolic formulation of Einstein's field equations, combined with high-order derivative and dissipation operators with the summation-by-parts property, penalized inter-patch boundary conditions and constraint-preserving outer boundary conditions leads to a stable and accurate discrete model. Specifically, isolated Schwarzschild black holes in coordinates adapted to the Killing fields, and in coordinates on which a gauge wave is imposed, and Schwarzschild black holes accreting scalar wave pulses were taken as typical model

systems involving excision. The results show that the introduction of several co-ordinate patches and of a Cauchy–perturbative matching interface does not intro-duce significant artefacts or instabilities. Rather, the high-order methods allow the accurate long-term evolution of accreting black holes with excision and Cauchy–perturbative matching in reasonable resolutions. As an example, we have presented the evolution of such a system with the high-order SBP operator D_{6-5}, which, at a resolution of $\Delta x = M/10$, introduced an error of only 0.3% after an evolution time of $1,000,000M$.

Most systems of interest in general relativistic astrophysics will necessarily require the use of three-dimensional codes. Results from a one-dimensional study are useful in that (i) experience can be gained in a clean but non-trivial physical system, (ii) they can be easily reproduced without the need for implemention of three-dimensional codes with multiple coordinate patches and (iii) isolation of sources of difficulty in the three-dimensional setting can be obtained more easily. With the promising results from this study, we can, as a next step, apply these techniques to a three-dimensional general relativistic setting.

Chapter 3

Extracting waveforms using a gauge-invariant perturbative approach

3.1   Introduction

One of the goals of numerical solutions of Einstein's equations is the prediction and analysis of the gravitational radiation emitted in some physical process. There are many methods for computing, or *extracting*, gravitational waves from a numerical spacetime. They can be broadly divided into two groups, depending on whether the solution includes null infinity (or a portion of it), or whether the computational domain is truncated at a hopefully large but finite distance from the source. In the first case, gravitational radiation can be defined and extracted in an unambiguous, rigorous way (see e.g. [174] and references therein, and [94]). In the second case, some approximation has to be made; not only at the level of the observer being in the radiation zone, but also in the way the "gravitational radiation" is computed in terms of the spacetime metric. Due to the additional complexity of evolving Einstein's equations all the way up to null infinity, currently most simulations actually truncate the computational domain by placing an artificial outer boundary at a finite distance. This study deals with one particular approach to gravitational wave extraction from spacetimes within this second group.

In general, one expects the differences between the exact waveforms and those extracted at a finite distance to decay as the extraction radius increases. One

natural question that arises is: for a given extraction method, how far away is far enough, so that the errors in the extracted waves are dominated by the accuracy of the simulations used to obtain the numerical spacetime, and not by the extraction mechanism itself? Here we address this question in detail in a very particular scenario, but which might shed some light on the general case.

The main idea of extracting waves at a finite distance is to exploit the structure of an asymptotically flat spacetime. One reads off the quantities which are needed to compute the gravitational radiation from the numerically generated solution. The method which we consider here is based on the well-known perturbations of the Schwarzschild spacetime. See e.g. [41, 44, 18, 182, 72, 75, 52, 22, 127, 45, 128, 53] for other approaches based on the Weyl scalar Ψ_4.

One possible approach is to assume that the full metric in the region of extraction can be considered as a perturbation of a flat spacetime, and to read off such perturbations from the numerical solution. This approach is justified by the fact that the leading order of the metric at large distances (in an expansion in powers of $1/r$) is flat. If the waves are extracted at a large but finite distance from the source, it makes sense to try to decrease the errors of the approximation by further considering the next order in the expansion of the metric, which is described by the Schwarzschild solution. In doing so, the numerical metric is not considered anymore a perturbation of flat spacetime, but instead of the Schwarzschild geometry. One can consider even higher orders in this background identification, such as the spin contribution. However, an important fact to keep in mind is that all these methods should in principle give the same gravitational radiation as the radius of extraction

increases. In other words, one should be able to compute the gravitational radiation through, for example, perturbations of a flat spacetime or the Schwarzschild metric, and the radiation should contain the information about the spacetime's non-zero mass and—if present—angular momentum when the observer is at large enough distances.

If only the first or the first two orders in the asymptotic expansion of the metric are kept when identifying this distant "background" geometry, then the framework for extracting gravitational radiation is that of perturbations of flat spacetime or of the Schwarzschild geometry, respectively. One can view the former as a sub-case of the latter, so that from hereon we will just consider perturbations of the Schwarzschild spacetime. In this case, perturbations decouple into two separate sectors, which differ in the parity of the perturbations (odd or even). These two parity sectors are directly related to the real and imaginary parts of the Weyl scalar Ψ_4 (see, for example, ref. [149]). Gauge invariant formalisms for such perturbations were developed by Regge and Wheeler [142] in the fifties for the odd-parity sector and by Zerilli [177] in the seventies for the even-parity sector.

The idea of using Regge–Wheeler–Zerilli perturbation theory to extract gravitational waves from numerical spacetimes is definitely not new. It goes back to pioneering work by Abrahams and Evans [4, 3, 5] (see also [1]) and it has been used extensively since the birth of numerical relativity (see [124] for a review). For example, the accuracy of simulations of distorted black holes was tested by comparing extracted waveforms against perturbative calculations [50, 51, 32, 7, 17], and often, also technical improvements (such as excision) were tested by studying their effects

on waveforms [11, 9]. Recently, [90] reported Zerilli waveforms from unequal mass binary black hole inspirals. In hydrodynamical simulations, gravitational waves are often determined via the quadrupole formula, which usually gives more accurate information in these particular situations (unless a black hole is present), since the wave amplitude is typically very small and thus difficult to detect from the spacetime metric [159, 160, 68].

In this work we present a generalization of this approach to gravitational wave extraction with two salient features. The first is at the level of the perturbation formalism itself: we use a generalization of the standard Regge–Wheeler–Zerilli (RWZ) formalism, which is not only gauge invariant, but also covariant [76, 149, 118, 86], in the sense that it is independent of the background coordinates. The standard RWZ formalism is gauge invariant only in the sense that the background metric is fixed to the Schwarzschild geometry *in Schwarzschild coordinates*, and the formalism is invariant with respect to infinitesimal, first order changes of coordinates, which keep the background coordinates *fixed*. However, in numerical simulations of Einstein's equations, the numerical spacetime might be close to the Schwarzschild geometry in certain situations (say, at large distances), but the metric does not need to be close to the Schwarzschild metric *in Schwarzschild coordinates*. In fact, when dealing with the black hole singularity through black hole excision, one uses coordinates that are well defined in a neighborhood of the horizon, and which are therefore clearly not of Schwarzschild type.

This first salient improvement (the use of a generalized formalism) is independent of the details of the numerical implementation. The second improvement is

tied to our particular numerical approach, which uses high order methods (typically higher than four) for high accuracy, and uses multiple blocks with adapted grids, non-trivial topologies, and smooth boundaries. The use of high order methods for both the evolution of Einstein's equations and for the wave extraction procedure itself, combined with the use of shells of "spherical" patches or blocks, allows us to extract gravitational waves in a simple, fast, and accurate way. In particular, *we can keep both the angular and radial resolutions fixed* and place the outer boundaries at large distances, using considerably less computational resources than what would be needed with Cartesian grids, even when using mesh refinement. In addition, no interpolation to spheres is needed to extract waves on spherical shells.

For weak perturbations of a Schwarzschild black hole we can actually obtain the exact solution by evolving the generalized Regge–Wheeler equation. Since this is a wave equation in $1 + 1$ dimensions, we can solve it with almost arbitrarily high accuracy. For all practical purposes, we consider it to be an exact solution, against which we can compare the extracted waveforms from our three-dimensional evolutions. We evolve weak perturbations of a Schwarzschild black hole in Kerr–Schild coordinates, using the fully nonlinear Einstein equations. We find that the assumption in the standard method that the background is in Schwarzschild–like coordinates increases the error in the extracted waves (as compared to extracting with the correct background) by between one and two orders of magnitudes. This is true even with observers as far away as $80\,M$, and even for the coarsest resolutions that we use. Furthermore, we explicitly see that the errors in the standard method do not converge to zero with increasing resolution at any fixed extraction radius,

while they do with the generalized method. The errors only decrease (as $1/r$, as we discuss in sect. 3.4) as the observer radius is increased. That is, if one does not use the correct background coordinates, these errors are dominated by the extraction procedure and not by the accuracy of the simulations. We compare the quasinormal frequencies of the waves extracted the above methods against the results predicted by perturbation theory.

The presentation goes as follows. In sect. 3.2 we describe in a self-contained way the generalized perturbation formalism, restricted to the odd-parity sector (we will present a similar treatment for the even parity sector elsewhere), and our construction of the Regge–Wheeler function from a numerical spacetime. We also use the inverse problem (that is, the generation of a perturbed metric from any given Regge–Wheeler function) to construct initial data that automatically satisfies the Einstein constraints when linearized around the Schwarzschild spacetime, which does not necessarily need to be given in Schwarzschild coordinates. This is the data that we later evolve and use in our numerical tests.

In sect. 3.3 we briefly describe our numerical techniques, our formulation of Einstein's equations, and our outer boundary conditions. Finally, we present our numerical results in sect. 3.4. We first show that our extracted covariant and gauge invariant Regge–Wheeler function coincides very well with the expected one from perturbation theory (which we obtain by solving the 1+1 generalized Regge–Wheeler equation) when we use the generalized formalism to identify the background correctly. After that, we compare our covariant and gauge invariant extracted waveforms with those obtained by the traditional approach, which assumes that the

background is either the Minkowski spacetime in Minkowski coordinates, or the Schwarzschild spacetime in Schwarzschild coordinates. In sect. 3.5 we discuss these results in the broader context of gravitational wave extraction for generic spacetimes.

For completeness, in Appendix A we describe in detail our conventions for tensor spherical harmonics decompositions.

3.2 Odd-parity perturbations of Schwarzschild and wave extraction

This section summarizes the results of the generalized formalism relevant for our analysis. We closely follow the notation and presentation of ref. [149].

3.2.1 The background metric and tensor spherical decomposition of the perturbations

The generalized formalism assumes that the total metric can be written as

$$g_{\mu\nu}^{\text{tot}} = g_{\mu\nu} + \delta g_{\mu\nu} \tag{3.1}$$

where $g_{\mu\nu}$ describes the Schwarzschild geometry and $\delta g_{\mu\nu}$ is, in some sense, a "small" correction. Further, it is assumed that the four-dimensional manifold can be decomposed as the product of a two-dimensional manifold $\mathcal{M}$ parametrized with coordinates x^a ($a = 0, 1$) and a unit 2-sphere S^2 with coordinates x^A ($A = 2, 3$), such that the background Schwarzschild metric takes the form

$$ds^2 = \tilde{g}_{ab}(t, r) \, dx^a dx^b + f^2(t, r) \, \hat{g}_{AB} \, dx^A dx^B \,. \tag{3.2}$$

60

Capital Latin indices refer to angular coordinates (θ, ϕ) on S^2, while lower-case ones refer to the (t, r) coordinates. Here $\hat{g}_{AB}$ is the standard metric on the unit sphere, $\tilde{g}_{ab}$ denotes the metric tensor on the manifold $\mathcal{M}$, and f^2 is a positive function. If one uses an areal radius coordinate, then $f = r$, but we do not make such an assumption. Actually, as we discuss below, the fact that our formalism is general enough to allow for $f = f(t, r)$ has practical advantages in the wave extraction procedure. For simplicity, the metric on the unit 2-sphere S^2 is assumed to be in standard coordinates: $\hat{g}_{AB} = \mathrm{diag}(1, \sin^2 \theta)$. Summarizing, we are assuming that the background Schwarzschild metric is given in a coordinate system in which there is no angular shift, but there can be a radial shift. Note that there is no assumption about the shift in the perturbation.

From a numerical relativity point of view, it is usually convenient to deal with the variables that appear in the $3 + 1$ split of spacetime. To this end, we follow the notation of ref. [149] and explicitly expand the components of the background Schwarzschild metric as

$$
\begin{aligned}
ds^2 \;=\;& (-\alpha^2 + \gamma^2 \beta^2) dt^2 + 2\gamma^2 \beta dt\, dr + \gamma^2\, dr^2 \\
& + f^2 (d\theta^2 + \sin^2 \theta\, d\phi^2)
\end{aligned}
\tag{3.3}
$$

where α and $\beta \equiv \beta^r$ are the background lapse and radial shift vector, respectively, and $\gamma^2 \equiv \tilde{g}_{rr}$. Since the background is spherically symmetric, it is convenient to expand the perturbations in spherical harmonics,

$$
\delta g_{\mu\nu} \;=\; \sum_{\ell=1}^{\infty} \sum_{m=-\ell}^{\ell} \delta g_{\mu\nu}^{(\ell,m)}\,.
\tag{3.4}
$$

In the odd-parity sector there is no perturbation for $\ell = 0$. The dipole term, $\ell = 1$, corresponds to the linearization of the Kerr metric using the angular momentum of the spacetime as a parameter. Thus, for gravitational wave extraction we only need to consider perturbations with $\ell \geq 2$. These quantities can be parametrized according to

$$\delta\beta_A^{(\ell,m)} = b^{(\ell,m)} S_A^{(\ell,m)} \qquad (3.5)$$

$$\delta g_{rA}^{(\ell,m)} = h_1^{(\ell,m)} S_A^{(\ell,m)}$$

$$\delta g_{AB}^{(\ell,m)} = h_2^{(\ell,m)} S_{AB}^{(\ell,m)}$$

$$\delta K_{rA}^{(\ell,m)} = \pi_1^{(\ell,m)} S_A^{(\ell,m)}$$

$$\delta K_{AB}^{(\ell,m)} = \pi_2^{(\ell,m)} S_{AB}^{(\ell,m)} \, .$$

Using the covariant derivative $\hat{\nabla}_A$ compatible with the metric $\hat{g}_{AB}$ on the unit sphere S^2 and its associated Levi–Civita tensor $\hat{\epsilon}_{AB}$ (with non-vanishing components $\hat{\epsilon}_{\theta\phi} = \sin\theta = -\hat{\epsilon}_{\phi\theta}$), we define $S_A = \hat{\epsilon}_A^B \hat{\nabla}_B Y$ (the first index in $\hat{\epsilon}$ raised with the inverse of $\hat{g}$) and $S_{AB} = \hat{\nabla}_{(A} S_{B)}$. Here, $Y \equiv Y^{(\ell,m)}$ are the standard spherical harmonics. The quantities S_A and S_{AB} form a basis on S^2 for odd-parity vector and symmetric tensor fields, respectively. The perturbation on the components of the extrinsic curvature are denoted by δK_{rA} and δK_{AB}. For completeness, we give a detailed and self-consistent description of how to use these to decompose vectors and tensors into spherical harmonics in Appendix A.

From now on, we suppress the superindices (ℓ, m) and the sum over them, since modes belonging to different pairs of (ℓ, m) decouple from each other in the perturbation formalism.

3.2.2 Extraction of the Regge–Wheeler function from a given geometry

To define the background metric, we extract the $\ell = 0$ component (that is, the spherically symmetric part) of the numerical solution $g_{\mu\nu}^{\text{tot}}$. This is done by decomposing the metric $\tilde{g}_{ab}$ of the two-dimensional manifold $\mathcal{M}$ into spherical harmonics. These metric components behave like scalars under a rotation of coordinates. Thus, the background metric is computed as

$$\tilde{g}_{ab} = \frac{1}{4\pi} \int g_{ab}^{\text{tot}} d\Omega, \tag{3.6}$$

where $d\Omega$ is the standard area element on S^2. The function f can be computed through $f = \sqrt{A/4\pi}$, with

$$A = \int \sqrt{\hat{g}^{\text{tot}}}\, d\theta\, d\phi, \tag{3.7}$$

where the integration is performed over the extraction 2-sphere, and $\hat{g}^{\text{tot}}$ is the determinant of g_{AB}^{tot}.

Similarly, we compute the perturbed quantities by extracting the $\ell \geq 2$ components of the numerical metric $g_{\mu\nu}^{\text{tot}}$, in the way explained in Appendix A.

Once we have obtained the multipoles $b, h_1, h_2, \pi_1, \pi_2$ defined above in eq. (3.5) and the background quantities f, α, γ, β defined in eq. (3.3), we can find the generalized gauge-invariant Regge–Wheeler (RW) function Φ_{RW}. It is given by [149]

$$\Phi_{RW} = \frac{2f}{\lambda \alpha \gamma} \left(\alpha\, \pi_1 - \frac{\partial_0 f}{f} h_1 \right) \tag{3.8}$$

where $\partial_0 \equiv \partial_t - \beta \partial_r$ and $\lambda = (\ell - 1)(\ell + 2)$. Notice from eq. (3.8) that the *only* multipole components appearing in the RW function Φ_{RW} are h_1 and π_1, so that

there is no need to compute the others.

Previous approaches to compute waveforms with the standard RWZ formalism have typically been considerably more involved than what we have just described. We briefly sketch the standard approach here. Einstein's equations are usually solved using Cartesian coordinates on a Cartesian grid. The numerically obtained metric is first transformed to polar-spherical coordinates. Performing the multipole decomposition on a given coordinate sphere requires a numerical integration over that sphere, which in turn requires interpolating the metric to the spherical surface, which does not coincide with the grid points of the Cartesian grid. Integrating over the sphere also allows computing the areal radius and its radial derivatives. These quantities are then used to transform the metric in a second step to its final form in "Schwarzschild-like" coordinates. This is done by first changing from the coordinate radius to an areal radius (which requires the numerically calculated radial derivatives), and then identifying the (t, r) components of the metric in this new coordinate system, which is assumed to be a perturbation of the Schwarzschild metric in Schwarzschild coordinates. With all this in place, the waveforms are then computed using standard RWZ formulae.

In our case, the multi-block grid structure naturally allows for spherical surfaces. Hence, no interpolation is required. The generalized perturbation formalism allows us to compute the RW function Φ_{RW} without transforming the metric to Schwarzschild coordinates. In particular, the transformation to an areal radial coordinate is not required at all. Thus, our extraction procedure amounts simply to numerical integrations at a given value of the radial coordinate to compute the

multiples, and then using eq. (3.8) to compute the RW function. An additional improvement is that our high order accurate derivative operators are naturally associated with a high order accurate discrete norm, leading to an integration procedure which has the same accuracy as our derivative operators.

3.2.3 (Re)construction of the metric from the Regge–Wheeler function

It can be seen (see, for example, ref. [149] for more details of what follows) that for any slicing of Schwarzschild of the type given in eqs. (3.2) or (3.3), that we can construct a perturbed four-metric from the RW potential. The perturbation coefficients of the linearized metric, as defined in eq. (3.1), become

$$\delta g_{r\theta} = \left[\frac{\gamma}{\alpha}\left(-f\dot{\Phi}_{RW} + \beta f\Phi'_{RW} + \Phi_{RW}(\beta f' - \dot{f})\right) + \frac{fk' - 2kf'}{f}\right]\frac{Y_\phi}{\sin\theta} \quad (3.9)$$

$$\delta g_{r\phi} = -\left[\frac{\gamma}{\alpha}\left(-f\dot{\Phi}_{RW} + \beta f\Phi'_{RW} + \Phi_{RW}(\beta f' - \dot{f})\right) + \right.$$
$$\left. \frac{fk' - 2kf'}{f}\right]\sin\theta Y_\theta \quad (3.10)$$

$$\delta g_{\theta\theta} = \frac{2k}{\sin^2\theta}\left[-\cos\theta Y_\phi + \sin\theta Y_{\theta\phi}\right] \quad (3.11)$$

$$\delta g_{\theta\phi} = k\left[\cos\theta Y_\theta + \sin^{-1}\theta Y_{\phi\phi} - \sin\theta Y_{\theta\theta}\right] \quad (3.12)$$

$$\delta g_{\theta t} = \left[\frac{1}{\gamma\alpha}\left(-\gamma^2\beta f\dot{\Phi}_{RW} + f(\gamma^2\beta^2 - \alpha^2)\Phi'_{RW} + \right.\right.$$
$$\left.\left. (-\alpha^2 f' - \dot{f}\beta\gamma^2 + f'\gamma^2\beta^2)\Phi_{RW}\right) + \frac{f\dot{k} - 2k\dot{f}}{f}\right]\frac{Y_\phi}{\sin\theta} \quad (3.13)$$

$$\delta g_{\phi\phi} = 2k\left[\cos\theta Y_\phi - \sin\theta Y_{\theta\phi}\right] \quad (3.14)$$

$$\delta g_{\phi t} = -\left[\frac{1}{\gamma\alpha}\left(-\gamma^2\beta f\dot{\Phi}_{RW} + f(\gamma^2\beta^2 - \alpha^2)\Phi'_{RW} + \right.\right.$$
$$\left.\left. (-\alpha^2 f' - \dot{f}\beta\gamma^2 + f'\gamma^2\beta^2)\Phi_{RW}\right)\frac{f\dot{k} - 2k\dot{f}}{f}\right]\sin\theta Y_\theta \quad (3.15)$$

65

Here dots and primes denote derivatives with respect to time and radius, respectively. It is $Y_\phi = \partial_\phi Y$, $Y_\theta = \partial_\theta Y$, and as before we are skipping the (ℓ, m) superindices. γ, α, β, and f are defined in eq. (3.3). It can be seen that the function k is a pure gauge term and completely arbitrary; in particular, we can make it vanish (resulting in the so called Regge–Wheeler gauge) through a first order coordinate transformation.

The generalized RW equation is

$$\ddot{\Phi}_{RW} \;=\; c_1 \dot{\Phi}'_{RW} + c_2 \Phi''_{RW} + c_3 \dot{\Phi}_{RW} + c_4 \Phi'_{RW} - \alpha^2 V \Phi_{RW} \tag{3.16}$$

with the coefficients c_i and the potential V given by

$$c_1 \;=\; 2\beta \tag{3.17}$$

$$c_2 \;=\; \frac{1}{\gamma^2} \left(\alpha^2 - \gamma^2 \beta^2 \right) \tag{3.18}$$

$$c_3 \;=\; \frac{1}{\gamma\alpha} \left(\gamma\dot{\alpha} - \gamma\beta\alpha' + \alpha\beta\gamma' - \alpha\dot{\gamma} + \gamma\alpha\beta' \right) \tag{3.19}$$

$$c_4 \;=\; \frac{1}{\gamma^3\alpha} \left(-\gamma^3\beta\dot{\alpha} - \alpha^3\gamma' + \gamma^3\beta^2\alpha' - 2\gamma^3\alpha\beta\beta' + \gamma^3\alpha\dot{\beta} + \gamma^2\alpha\beta\dot{\gamma} + \right.$$
$$\left. \gamma\alpha^2\alpha' - \gamma^2\alpha\beta^2\gamma' \right) \tag{3.20}$$

$$V \;=\; \frac{1}{f^2} \left[\ell(\ell+1) - \frac{6M}{f} \right]. \tag{3.21}$$

When the background metric is Schwarzschild in Schwarzschild coordinates, this generalized RW equation coincides of course with the standard equation. Below, in sec. 3.4, we use high-resolution solutions of this generalized $1+1$ equation as "exact" solutions , against which we compare the extracted RW function from our three-dimensional distorted black hole simulations.

66

3.3 Formulation of the equations, boundary conditions, initial data, and numerical methods

3.3.1 Evolution equations

The numerical simulations shown below were performed by evolving a first order symmetric hyperbolic reduction of the Generalized Harmonic formalism, as constructed in ref. [113]. In this formulation, the coordinates x^μ are chosen to satisfy the (generalized) harmonic condition[1] [74]

$$\nabla^\sigma \nabla_\sigma x^{(\mu)} = H^{(\mu)}(t, x^i), \tag{3.22}$$

where the gauge source functions $H^{(\mu)}(t, x^i)$ are freely specifiable functions of the spacetime coordinates, and ∇_μ is the covariant derivative associated with $g_{\mu\nu}$. Here we omit the label "tot" from the metric (3.1) for the sake of simplicity. The reduction from second to first order is achieved by introducing the first derivatives of the metric $g_{\mu\nu}$ as independent quantities. Following ref. [113], we introduce the quantities

$$Q_{\mu\nu} = -n^\sigma \partial_\sigma g_{\mu\nu} \tag{3.23}$$

$$D_{i\mu\nu} = \partial_i g_{\mu\nu}, \tag{3.24}$$

where $n_\mu = -\alpha \nabla_\mu t$ is the (future directed) timelike unit normal vector to the hypersurface $t = x^0 = $ const. Thus, the evolution equations for $Q_{\mu\nu}$ are given by the Generalized Harmonic formalism, while the evolution equations for $D_{i\mu\nu}$ are

---

[1]In this subsection we use the Latin indices $i, j, k, \ldots$ to denote three-dimensional spatial quantities, while Greek indices continue to represent the four-dimensional ones.

obtained by applying a time derivative to their definition (3.24) and commuting the temporal and spatial derivatives. Finally, the metric $g_{\mu\nu}$ is evolved using the definition of $Q_{\mu\nu}$, eq. (3.23). In addition, in the spirit of refs. [37, 87], the constraints of this system are added to the evolution equations in such a way that the physical solutions (i.e., those satisfying the constraints) are an attractor in certain spacetimes. In those situations, small constraint violations will be damped during the evolution. The whole construction of this formulation of the equations is described in detail in [113].

The standard $3 + 1$ components of the metric (i.e., the lapse function α, the shift β^i, and the intrinsic metric γ_{ij}) can be obtained via the relations

$$\alpha^2 = -1/g^{tt} \tag{3.25}$$

$$\beta_i = g_{ti} \tag{3.26}$$

$$\gamma_{ij} = g_{ij}. \tag{3.27}$$

The extrinsic curvature is defined in terms of the intrinsic metric as

$$K_{ij} = \frac{1}{2\alpha}(\partial_t - \mathcal{L}_\beta)\gamma_{ij}. \tag{3.28}$$

It can be recovered from the fields $Q_{\mu\nu}$, $D_{i\mu\nu}$ via

$$-2\alpha K_{ij} = \alpha Q_{ij} + D_{itj} + D_{jti}$$
$$- \gamma^{km}\beta_m(D_{ijk} + D_{jik}). \tag{3.29}$$

In our simulations below we also monitor the Hamiltonian and momentum ADM

constraints, namely,

$$\mathcal{H} = \frac{1}{2}\left(^{(3)}R - K_{ij}K_{ij} + (trK)^2\right) \qquad (3.30)$$

$$\mathcal{M}_i = \nabla_k\left(K_i^k - \delta_i^k trK\right), \qquad (3.31)$$

where $^{(3)}R$ is the Ricci scalar associated to the three-dimensional space-like metric γ_{ij}.

We impose maximally dissipative boundary conditions at the outer boundary. While these conditions guarantee well-posedness of the associated initial value problem, and thus numerical stability with our particular discretization, they are physically incorrect in the sense that they do not include back-scattered radiation from outside the simulation domain. For that reason, in the simulations shown below we place the outer boundary at large enough distances so that our extracted waves are causally disconnected from boundary effects.

3.3.2 Multi-block approach

We use multi-block (also called multi-patch or multi-domain) methods for our numerical calculations. These have several advantages over single-domain methods:

Smooth boundaries. They provide smooth outer and inner boundaries, which is in general required [157] for a well-posed initial boundary value problem.

Constant resolution. They allow us to use constant radial and angular resolutions. This is not possible with mesh refinement methods. The way in which mesh refinement is typically used leads to a decreasing radial resolution, which makes it

difficult to extract accurate gravitational wave information in the wave zone of a binary black hole system. (See sect. 3.5, where we list typical wave extraction radii and resolutions.)

No time-stepping restrictions. They do not lead to a deterioration of the Courant-Friedrichs-Lewy (CFL) factor[2] for co-rotating coordinates. (For example, [42] reports that the CFL factor had to be reduced on the outermost refinement levels. The same was done later in [63].)

Adapted to symmetries. They can be adapted to the symmetries of a system. Obviously, adapted coordinates can reduce the discretization error significantly. In our case, we use on each block one radial and two angular coordinates to model the geometry of a single black hole. For binary black hole systems, one can use blocks that are roughly spherical near the individual holes and far away in the wave zone, with a transition region in between. Fig. 5 in [155] shows a possible multi-block system for this.

No coordinate singularities. They have no coordinate singularities. Spherical or cylindrical coordinates have singularities on the z axis which may cause problems. An alternative approach which avoids these singularities would be to use a pseudo-spectral decomposition into spherical harmonics. This was used in [151] to evolve scalar fields on a Kerr background, in [101, 152] to evolve Einstein's, and in [83,

---

[2]The CFL factor is denoted as the ratio between the time step Δt and the spatial grid spacing Δx.

84, 135, 15, 14, 114] to set up initial data for various black hole and neutron star configurations.

Of course, using multiple blocks adds to the complexity of an implementation. However, the properties of multi-block systems for hyperbolic equations are by now well understood, and we describe our particular approach in [111] and [61], and in some detail in [155]. In this particular study we use a *six-block system* to discretize the geometry of a single black hole, which is depicted in fig. 3.1. We use the same tensor basis on each block, namely a global three-dimensional Cartesian coordinate system. We found that this greatly simplifies the inter-block boundary conditions, since all components of tensorial quantities are then scalars with respect to the block-local coordinate systems.

We use the *penalty method* to enforce the inter-block boundary conditions. The penalty method for finite differences is described in [56, 57, 129], and we describe our approach and notation in [111, 61, 155]. In short, the penalty method works as follows. The individual blocks do not overlap, but they have their boundary points in common. The evolution equations are first discretized on each block independently using one-sided derivatives near the block boundaries. Then a correction term is added to the right hand side of the time derivative of each characteristic variable at the boundary points, penalizing the difference between the left and right eigenmode values u^l and u^r on the boundary points:

$$\partial_t u^l \quad \rightarrow \quad \partial_t u^l + \frac{S^l}{h^l \sigma^l} \left(u^r - u^l \right) \tag{3.32}$$

$$\partial_t u^r \quad \rightarrow \quad \partial_t u^r + \frac{S^r}{h^r \sigma^r} \left(u^l - u^r \right). \tag{3.33}$$
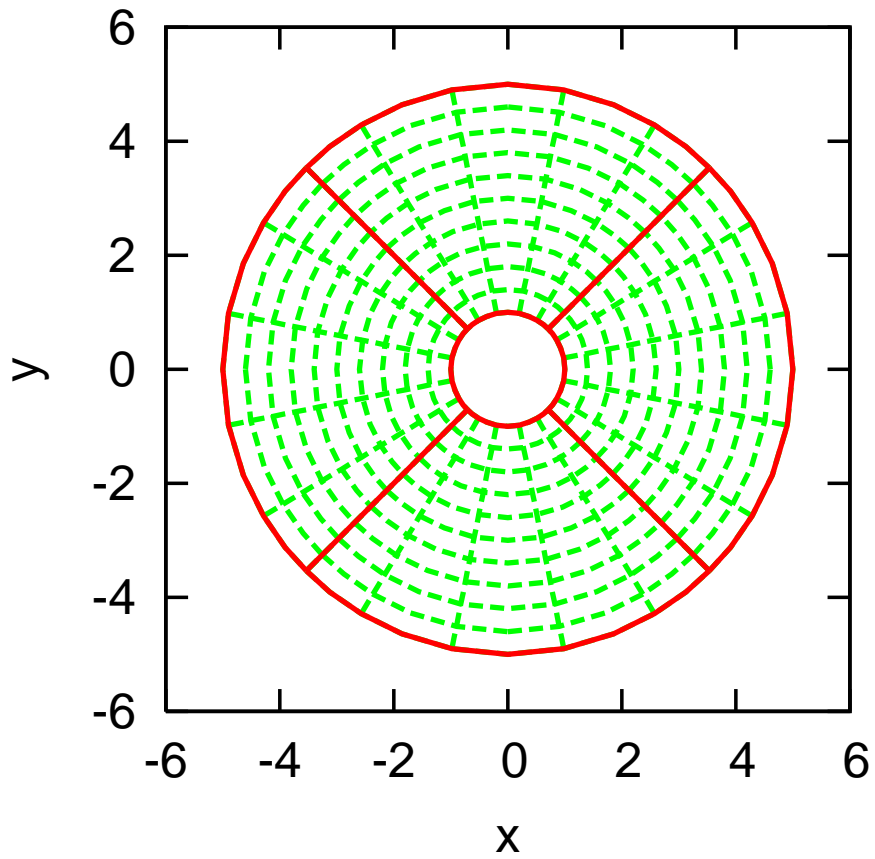
Figure 3.1: The equatorial plane of an example six-block geometry, cutting through four blocks. Note that the blocks do not overlap. All six blocks are made up identically. The outer and inner boundaries are smooth spheres. The outer boundary in our typical simulations is actually located much further out than shown here.

Here h^l and h^r are the grid spacings on the two blocks, which may be different. These penalty terms ensure continuity between the two blocks in the continuum limit and numerical stability in the semi-discrete case if the relevant parameters are appropriately chosen. The quantities σ^l and σ^r depend on the coefficients of the differencing operators that are used on the two blocks.[3] The parameters S^l and S^r determine how much (if any) dissipation is introduced across the block boundary. To ensure stability, they must be chosen in a very specific way depending on the characteristic speeds of the evolution system.

We have implemented this in the Cactus framework [82], using the Carpet driver [156] and the CactusEinstein toolkit.

3.3.3 Initial data

If the RW function Φ_{RW} satisfies the RW equation (3.16), then the perturbed metric constructed in sect. 3.2.3 satisfies the linearized Einstein equations. Furthermore, it can be explicitly shown that this metric initially satisfies the linearized constraints around the Schwarzschild geometry for *any* initial values $\Phi_{RW}(t = 0, r)$ and $\dot{\Phi}_{RW}(t = 0, r)$.[4] We take advantage of this property and construct initial data in a simple way as a test our new wave extraction method. For our simulations

---

[3]To be exact, σ^l and σ^r depend on the coefficients of the discrete norms that are used in the blocks, but the differencing operators and the norms are usually chosen together to satisfy *summation by parts*. See [48, 49, 110], and especially [61].

[4]When constructing initial data for the $3 + 1$ quantities, one also needs to take time derivatives of the four-metric; where second time derivatives of Φ_{RW} appear, we use the RW equation to trade these for space derivatives.

below, we use Kerr–Schild coordinates for the Schwarzschild background, and for the distortion we set $\ell = 2$, $m = 0$, and choose

$$
\begin{aligned}
\Phi_{RW}(t = 0, r) &= 0, & &\text{(3.34)} \\
\dot{\Phi}_{RW}(t = 0, r) &= A\, e^{(r - r_0)^2/\sigma^2}
\end{aligned}
$$

with parameters r_0 and σ. This corresponds to a Gaussian pulse of width σ centered at $r = r_0$.

If we assume that we can Taylor–expand (a suitable norm of) the discrete non-linear constraints in terms of the perturbation amplitude A for any fixed grid spacing h, we have

$$
\begin{aligned}
\mathcal{C}(A, h) &= \mathcal{C}(A, h)|_{A=0} & &\text{(3.35)} \\
&\quad + A\, \frac{\partial \mathcal{C}(A, h)}{\partial A}\bigg|_{A=0} \\
&\quad + \frac{A^2}{2}\, \frac{\partial^2 \mathcal{C}(A, h)}{\partial A^2}\bigg|_{A=0} + \mathcal{O}(A^3).
\end{aligned}
$$

Since in the continuum the linearized constraints are satisfied, the first two terms in the above expansion vanish for $h \to 0$, but otherwise are of the order of the truncation error. For small enough A the first term (that is, the background contribution) dominates, and the term $\mathcal{C}(A, h)$ appears to be independent of A. For large enough A, on the other hand, the quadratic term in the expansion given by eq. (3.35) will dominate.

Fig. 3.2 presents numerical evidence that this expected behavior is indeed the case. We set up numerical data according to eq. (3.34), with perturbation amplitudes A between 10^{-6} and 10^{-1}. The radial domain extent is $1.8 \leq r \leq 7.8$,
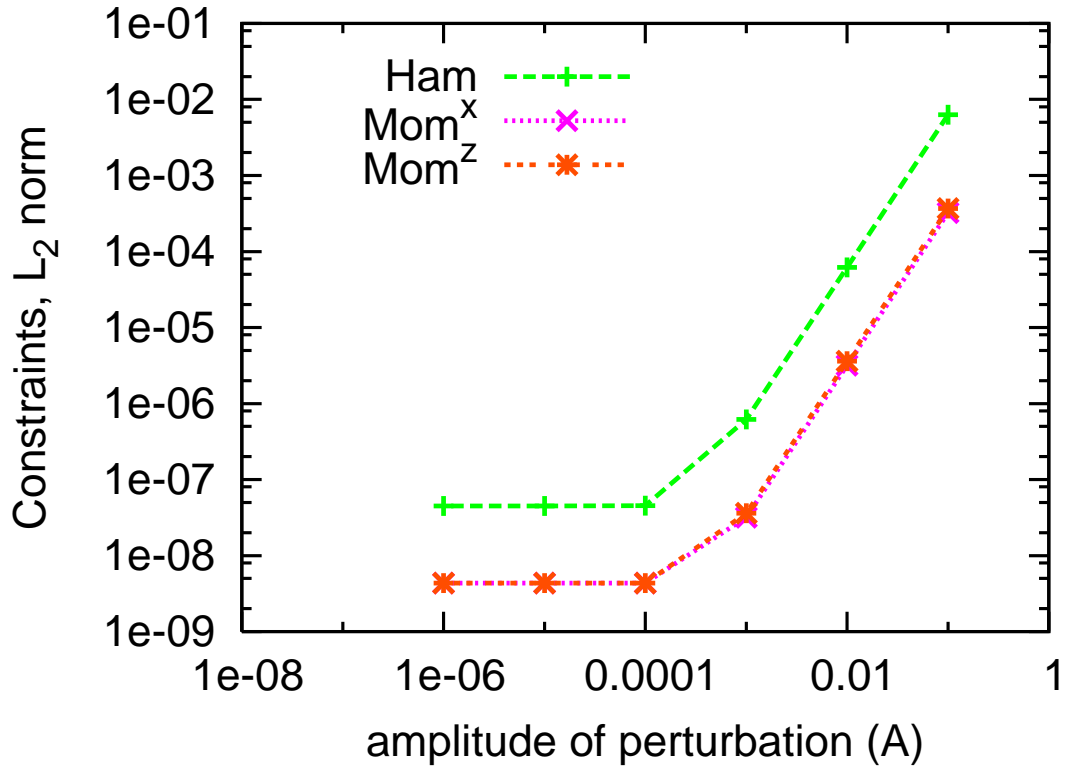
Figure 3.2: Discrete constraint violations for various perturbation amplitudes A at a fixed (high) resolution. We show the L_2 norm for the Hamiltonian constraint and for two components (x and z) of the momentum constraint (which turn out to be very close to each other, as the plot shows). The numerical resolution is 109×109 grid points per block in the angular directions and $\Delta r \approx 0.0148$ in the radial direction. The behavior is as expected and as described in the main text: for sufficiently small amplitudes, the background contribution dominates the discretization error in the constraints, which then appear to be independent of A. For large enough amplitudes, the constraint violation has a quadratic dependence on A (with an exponent of 2.01 ± 0.01 for the resolution shown in this figure), since for our initial data only the linearized constraints (around Schwarzschild) are satisfied.

the perturbation is centered around $r_0 = 4.8\,M$ and has a width of $\sigma = 1.0\,M$. We then compute the discrete Hamiltonian and momentum constraints $\mathcal{H}$ and $\mathcal{M}^i$ for these initial data sets, using the same (high) resolution, namely 109×109 grid points on each block in the angular direction and 406 points in the radial direction, corresponding to $\Delta r \approx 0.0148\,M$. Due to the symmetry of our six-block structure and the axisymmetry of the initial data, two components of the discrete momentum constraints coincide, $\mathcal{M}^x = \mathcal{M}^y$, and we therefore do not show the latter. The behavior of the constraints in the L_2 and the L_∞ (not shown in the figure) norms agrees with eq. (3.35): for small amplitudes A, the discrete constraints at a fixed resolution appear to be independent of A, while for large amplitudes they show the expected quadratic dependence on A. We also show that the discrete constraint violations of our initial data sets have the expected dependence on resolution. For small amplitudes and coarse resolutions, the contribution of the quadratic term in eq. (3.35) is sufficiently small, so that the constraints seem to converge towards zero. However, for any given amplitude A a fine enough resolution h reveals that the convergence is actually towards a small but non-zero value, determined by the quadratic term in the expansion eq. (3.35). This behavior is shown in fig. 3.3. As an illustration we show there a convergence test for $\mathcal{H}$ by comparing initial data for different resolutions. The highest resolutions are identical to those used in fig. 3.2. The other four resolutions shown are $73 \times 73 \times 271$, $49 \times 49 \times 181$, $25 \times 25 \times 91$, and $17 \times 17 \times 61$ grid points per block, corresponding to $\Delta r \approx 0.0222\,M$, $0.0333\,M$, $0.0667\,M$, and $0.1\,M$, respectively.
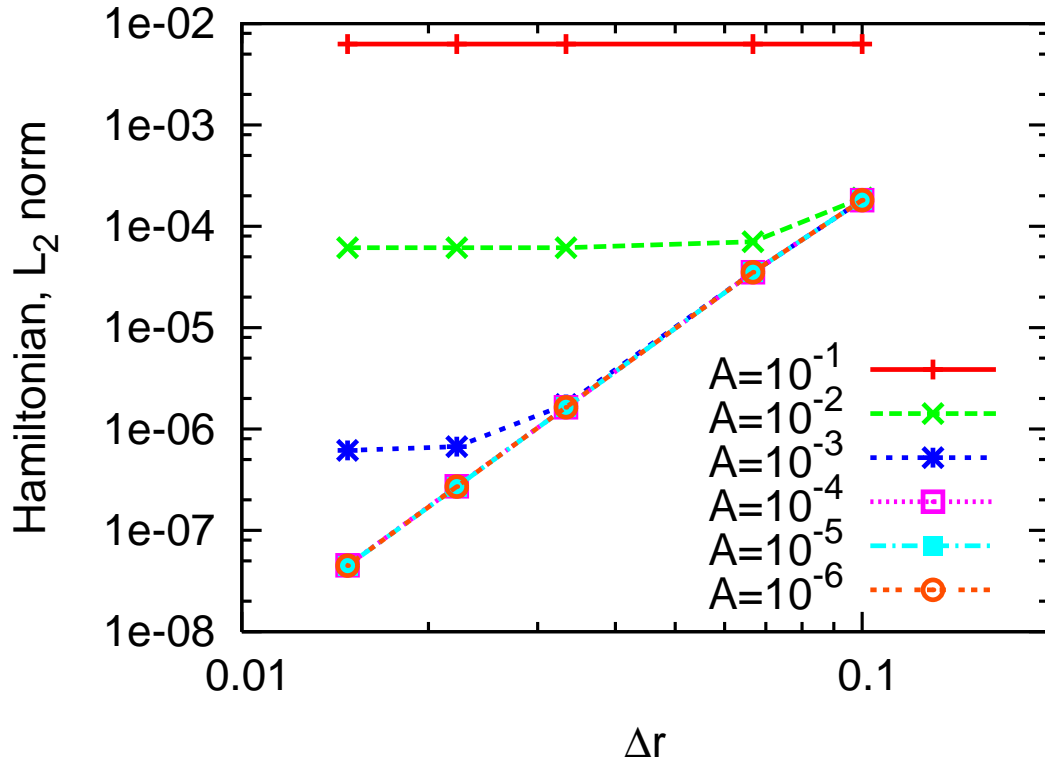
Figure 3.3: L_2 norm of the Hamiltonian constraint for different amplitudes A of the perturbation and for different resolutions h. The coarsest resolution uses 17×17 points per block in the angular directions and $\Delta r = 0.1\, M$ in the radial direction. We increase the resolution in all directions, up to 109×109 points in the angular directions and $\Delta r \approx 0.0148\, M$ in the radial direction. Since only the linearized constraints are satisfied, the non-linear constraints do not converge to zero. For sufficiently large perturbation amplitudes and for sufficiently fine resolutions, the non-linear effects become visible, and the constraint violations converge to a constant value which depends on the amplitude A. As shown in the previous figure, this dependence is quadratic, as expected.

3.4 Numerical studies

3.4.1 Description of the simulations

We use the D_{8-4} operator constructed in [61], a summation by parts operator [106, 107] which is eighth order accurate in the interior and fourth order accurate at the boundaries, optimized to minimize its spectral radius and boundary truncation errors. Fifth order global convergence is expected [88, 89]. We integrate in time with a fourth order Runge–Kutta integrator with adaptive time stepping as described in [136].

In order to test both the long term stability and the convergence of our code, we first evolve a Kerr black hole in Kerr–Schild coordinates with spin $j = 0.5$. Fig. 3.4 shows the L_2 norm of the Hamiltonian constraint vs. time for two different resolutions. The radial domain extent is $1.8\,M < r < 11.8\,M$. The coarse resolution corresponds to $\Delta r = 0.2\,M$ and 16×16 points per block in the angular directions, and the fine resolution increases the number of points in all directions by a factor of 1.5. We see approximate fifth order convergence, as expected.

In the simulations discussed below, we place our inner boundary at $r = 1.8\,M$ and our outer boundary at $r = 251.8\,M$. This allows for observer locations up to $r = 80\,M$, which are still causally disconnected from the outer boundary for times long enough to follow the ringdown, namely up to $t = 280\,M$. We set up initial data according to eq. (3.34) with $A = 0.01$, $\sigma = 1.0\,M$, and $r_0 = 20\,M$, where M is the mass of the black hole when the perturbation is switched off. Our coarse resolution uses 16×16 points per block in the angular directions and 1251 points in the radial

78
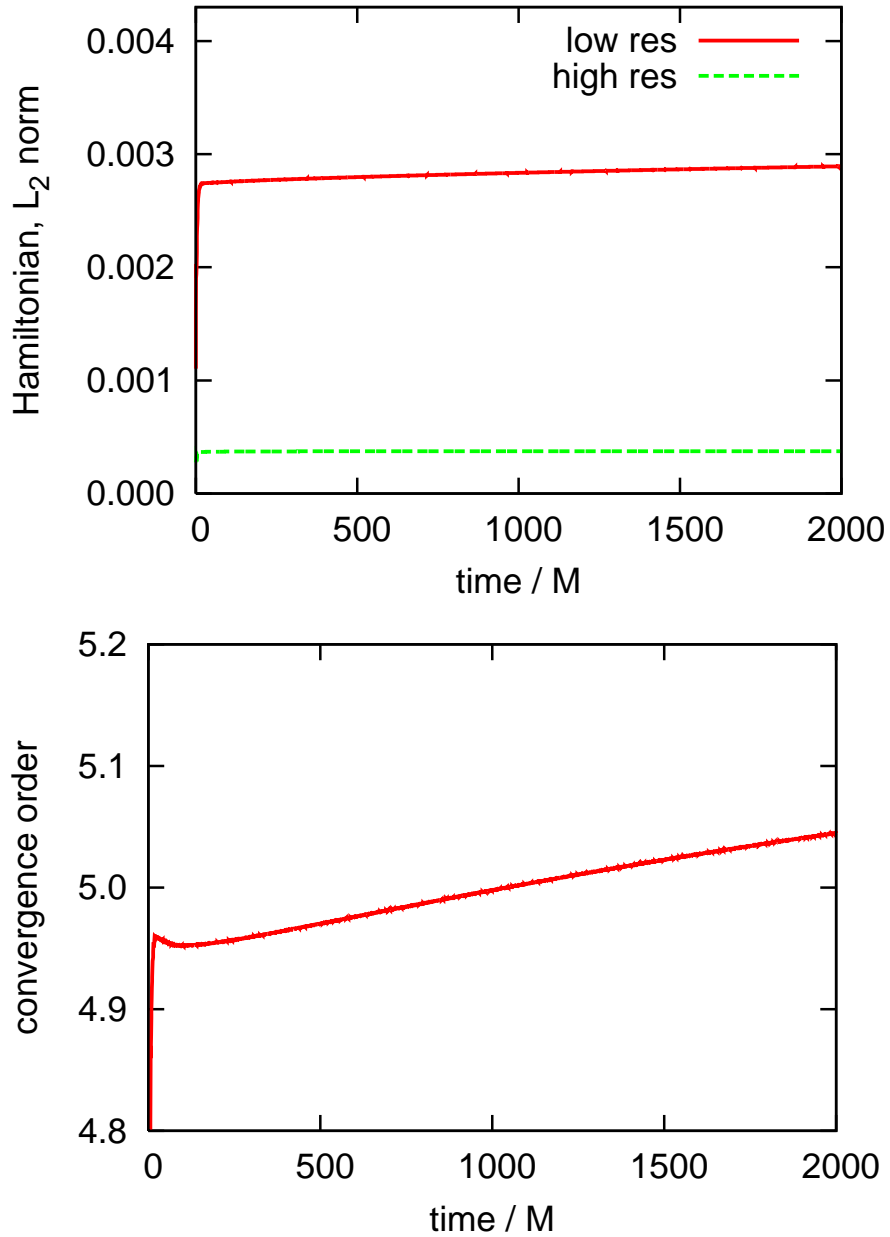
Figure 3.4: L_2 norm (top panel) and convergence factor (bottom panel) for the Hamiltonian constraint for evolutions of a Kerr black hole with spin $j = 0.5$. The coarse resolution corresponds to 16×16 points per block in the angular directions and $\Delta r = 0.2\,M$ in the radial direction. The fine resolution a factor of 1.5 higher in all directions. We see fifth order convergence, as expected for the difference operators used.

direction, corresponding to $\Delta r = 0.2\,M$. Our fine resolution uses 1.4 times as many grid points in all directions.

One of the goals of the analysis that follows is to study the effect of the choice of the background metric on the accuracy of the waveforms. Since for this scattering problem solutions in closed form are not known, we compare the waves which we extract from our three-dimensional simulations to results obtained with an independent fourth order accurate one-dimensional code which solves the Regge–Wheeler equation (3.16). These 1D results were obtained with a resolution of $\Delta r = 0.0125\,M$. The relative difference in this Regge–Wheeler function to a result from twice this resolution lies roughly between roundoff error and 10^{-7}, which is far below the numerical errors that we expect from our 3D simulations. Therefore, we consider these 1D results in the following to be exact for all practical purposes.

3.4.2 The standard and generalized RW approaches: numerical comparisons

We now analyze the results of evolving distorted black holes as described above and extracting gravitational waves with different methods.

Fig. 3.5 shows Regge–Wheeler functions for observers at $r = 20\,M$, $40\,M$, and $80\,M$, extracted with both our generalized approach and the standard one. The data have been scaled by a factor of 100 to normalize to an initial data amplitude $A = 1$ in eq. (3.34). Recall that we used weak waves of amplitude $A = 0.01$ for these simulations to avoid non-linear effects, and to be able to compare with the

exact solution, which is only known in the linear regime.

Five waves are shown in fig. 3.5 for each observer location. Apart from the exact solution, we show two results obtained from our generalized approach, which coincide with each other in the continuum limit. They differ in how the background metric is computed: in one case we use the exact expressions for the Kerr–Schild background, and in the other case these coefficients were numerically calculated by extracting the $\ell = 0$ part of the metric, as explained in sect. 3.2.2.

Finally, two waveforms were extracted using the standard approach with two different assumptions for the background, as found in the literature: a Minkowski spacetime in Minkowski coordinates, and a Schwarzschild spacetime in Schwarzschild coordinates. We want to highlight an interesting feature which can easily be seen in eq. (3.8). For any observer location, the waves extracted with these two background should differ only by a factor which is constant in time:

$$\Phi_{RW}^{\text{Min}} = \kappa \Phi_{RW}^{\text{Sch}}, \tag{3.36}$$

where $\kappa^2 = g_{rr}^{\text{Sch}}$ is radial component of the Schwarzschild metric in Schwarzschild coordinates. Such a simple relationship is a direct consequence of the vanishing radial shift for these backgrounds. We confirmed this expected behavior numerically with high accuracy: at all times and for all observers we recover this expected ratio between the two waves to double precision roundoff error.

Figure 3.5 suggests that, as expected, the differences between waves extracted with different methods decrease as the extraction radius increases. At $r = 80\,M$, the
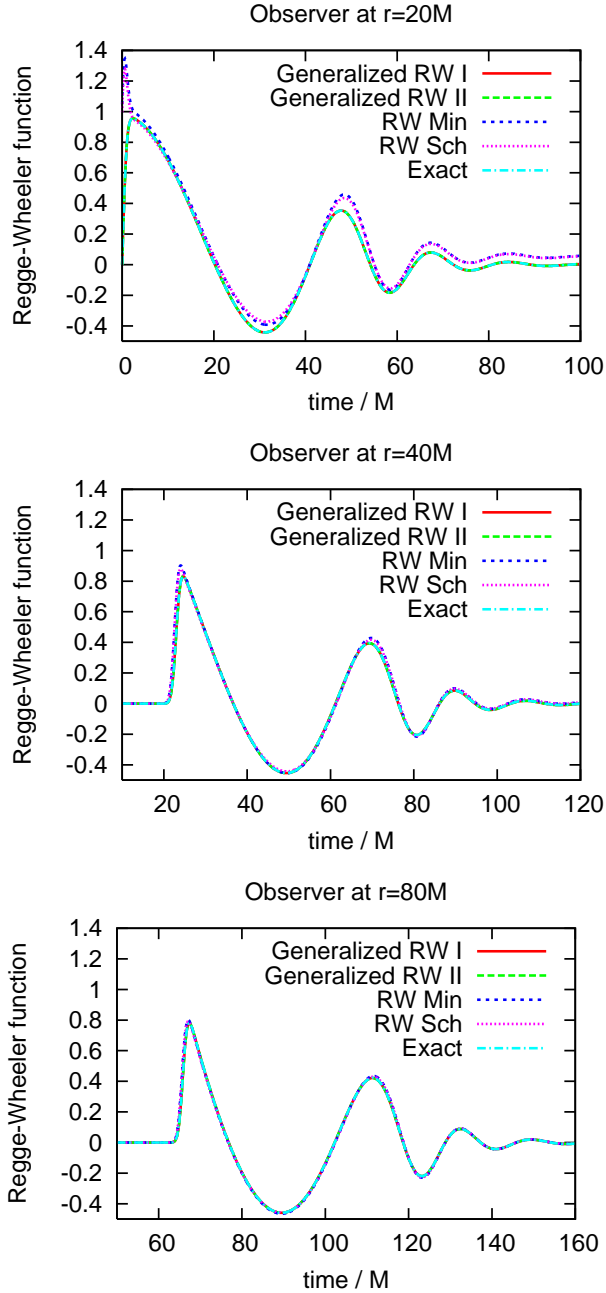
Figure 3.5: Extracted waveforms for observers at $20\,M$, $40\,M$, and $80\,M$. Shown is the Regge–Wheeler function obtained from the standard RW approach and our generalized one. For the former we assumed both a Minkowski background and a Schwarzschild background in Schwarzschild coordinates, labeled as *RW Min* and *RW Sch*, respectively. For the generalized approach we show the results for two cases, in which the background metric is dynamically computed from the numerical solution (*Generalized RW I*), and where we prescribe it analytically (*Generalized RW II*). Also shown is the exact waveform. These simulations were performed with a resolution of 16×16 grid points in the angular directions on each block and $\Delta r = 0.2\,M$ in the radial direction. See the main text for more details.

curves show excellent agreement in the L_e norm[5]. For a more thorough comparison, we look at the differences between the extracted waves and the exact solution in fig. 3.6. For consistency with fig. 3.5, we also scaled the errors relative to the initial amplitude of the perturbation.

Perhaps the most notable feature in fig. 3.6 is that the differences between the waves obtained from generalized approach either with a numerically obtained background metric or with the exact (Kerr–Schild) background metric are smaller than the difference to the exact solution. For all practical purposes we can therefore consider them identical to each other, and for the rest of the study we leave the latter out of the discussion.

Fig. 3.6 also shows that the standard approach—with either a Minkowski or Schwarzschild background—leads to errors which are considerably larger than the errors in our generalized approach, even for an observer at $r = 80\,M$. For the specific resolution that we used for fig. 3.6, the errors at $r = 20\,M$ with the standard method are roughly three orders of magnitude larger than the errors with the generalized method. For $r = 40\,M$ and $80\,M$, the ratio of the errors is of the order 10^3 to 10^1 and 10^2 to 10^0, respectively.

The previous discussion only analyzes the errors introduced by the standard method at a fixed resolution. Next we discuss the dependence of these results on the resolution. It turns out that the difference between the different methods is even more striking for higher resolutions. By construction, the generalized wave extraction method should give the exact waveform in the continuum. At the discrete

---

[5]Also denoted by $L_{\mathbf{eyeball}}$
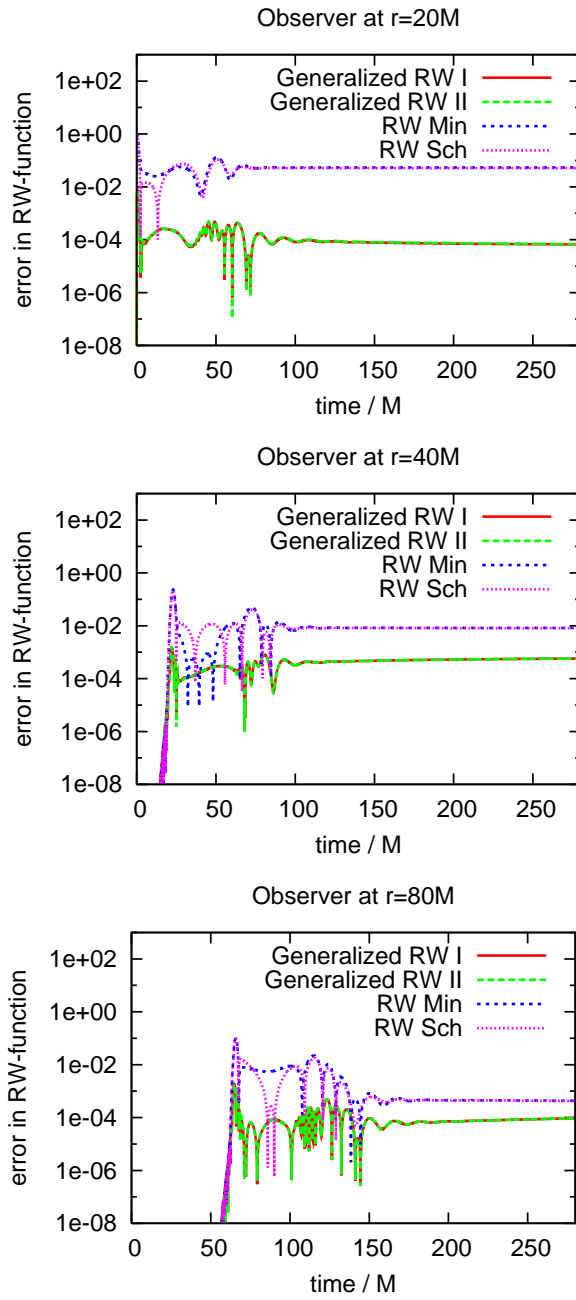
Figure 3.6: Errors for the waveforms shown in fig. 3.5.

level, its associated errors should converge away with increasing resolution. Fig. 3.7 shows that this is actually the case. On the other hand, the errors in the standard approach do *not* converge to zero, as shown in fig. 3.7. In other words, the accuracy of the extracted waves with the standard method is dominated by the extraction procedure and not by the numerical resolution.

Fig. 3.7 as well as the second panel of fig. 3.6 show another interesting feature. Contrary to expectation, assuming Schwarzschild–like coordinates instead of a Minkowski background does not necessarily lead to smaller errors in the waveforms. For example, for an observer at $r = 40M$ and during the time interval of about $25M < t < 50M$, the errors are actually up to one order of magnitude larger for the Schwarzschild–like coordinates. However, as can be seen from fig. 3.6, this feature depends on the observer location. We assume that this feature is only a coincidence.

The plateau in the errors seen in the last $100\,M$ to $200\,M$ in fig. 3.6 is due to an offset in the waveform. We found that, once the wave function decays to a small enough amplitude, it no longer oscillates around zero, but instead oscillates around a certain offset. This can be seen more clearly from the top panel in fig. 3.5. This offset is present for both the standard and the generalized extraction methods; however, there are important differences. The first is that the offset for the generalized extraction converges to zero with increasing resolution, unlike for the standard method. The other is that the offset for the generalized method is orders of magnitude smaller than for the standard method. As we will discuss in the next subsection, that has direct consequences when attempting to extract quasinormal frequencies. This offset is reminiscent of the one that is present in RWZ waveforms
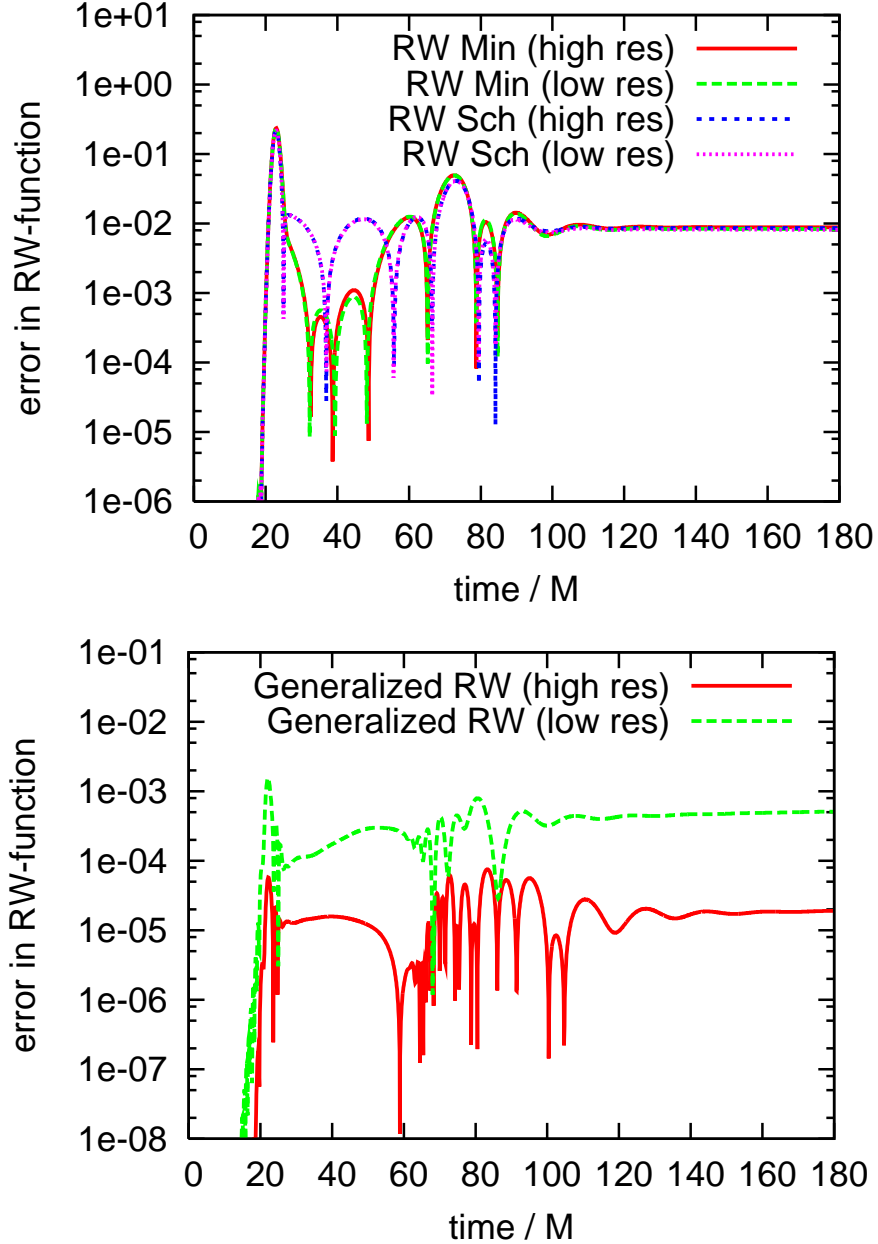
Figure 3.7: Shown is a convergence test for the simulations presented in the previous two figures. The plots labeled with "low res" coincide with the ones shown in the previous figures, while the plots labeled with "high res" correspond to 1.4 times that resolution. The error in the generalized wave extraction method, which by design gives the correct waveform in the continuum for these simulations, converges towards zero as expected. On the other hand, the errors in the standard wave extraction method are almost unaffected by the increased resolution. This indicates that these errors are dominated by the extraction method itself, not by the numerical truncation error. These results correspond to an observer at $40\,M$, but they look similar for the other extraction radii that we consider in this study.

when there is spin [8, 33].

The oscillatory feature of the wave can be followed for a longer time if the offset is subtracted from the waveform by hand, that is, if the wave is shifted along the vertical axis so that it oscillates around zero at late times. We do so by fitting the data to an exponentially decaying wave with an offset. (Details about the fit are given in the following subsection) The actual values that we determined for the offset are given in table 3.1. As expected, the offset is decreasing with increasing radius for both standard RW wave extraction methods. This offset is mainly a result of the wrong assumption about the background metric, not of numerical error. There is no such clear dependence on the radius when using the new generalized extraction. Here the offset originates solely from truncation error, and converges to zero with increasing resolution. This behavior can also be seen in fig. 3.7.

In fig. 3.8 we show the difference between the waveforms shifted by different offset values and the exact solution, for the same observers as before. As can be seen from the figure, our qualitative statements about the accuracies of the different wave extraction methods remain unchanged, if you consider the time span during which the amplitude of the wave is significant.[6] We conclude that the main errors in fig. 3.6 are *not* caused by an overall offset in the whole waveform.

---

[6] Of course, because we subtract the offset by hand to decrease the errors at late times, we can naturally follow the oscillatory part of the wave for longer times before.

Extraction Method	Observer	Offset
Generalized RW	$20M$	-7.1×10^{-5}
Generalized RW	$40M$	5.6×10^{-4}
Generalized RW	$80M$	8.9×10^{-5}
RW Min	$20M$	-5.4×10^{-2}
RW Min	$40M$	-8.3×10^{-3}
RW Min	$80M$	-4.4×10^{-4}
RW Sch	$20M$	-5.1×10^{-2}
RW Sch	$40M$	-8.1×10^{-3}
RW Sch	$80M$	-4.3×10^{-4}

Table 3.1: Values of the offset for different wave extraction methods and observers at $20M$, $40M$ and $80M$.
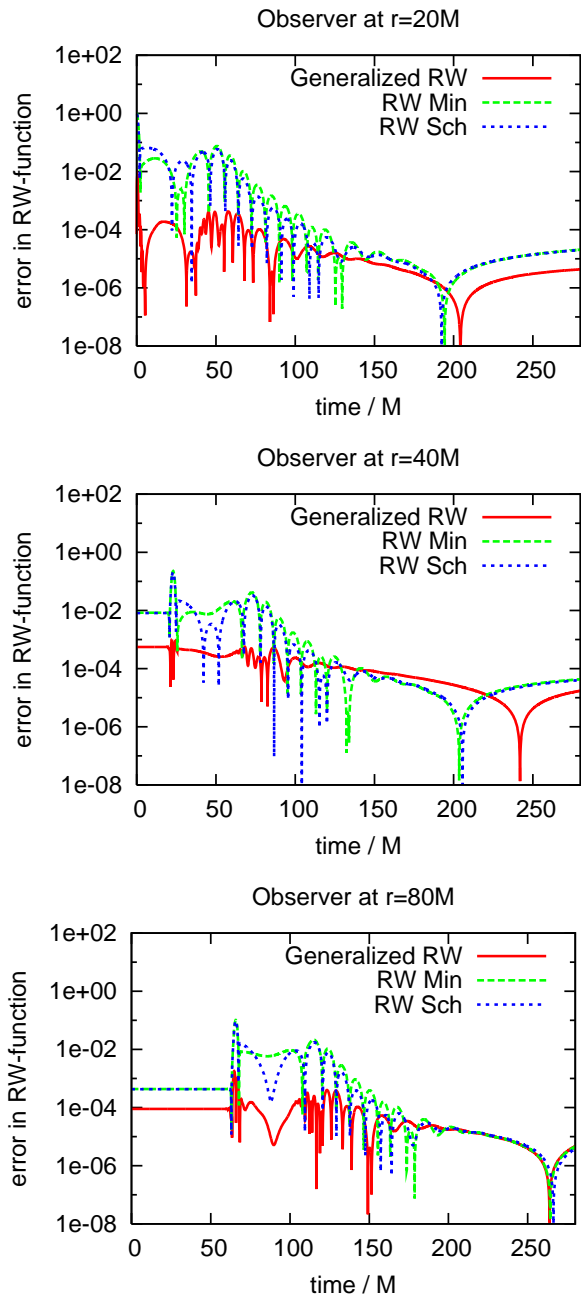
Figure 3.8: Shown are the same quantities as in fig. 3.6, except that an offset is subtracted from each waveform before calculating the errors. See the main text for details.

3.4.3   Quasinormal frequencies

We now turn our attention to extracting quasinormal frequencies from the waveforms just discussed. The primary goal is to find out whether these frequencies are affected by the choice of a specific wave extraction method, which may have some presumably small but non-vanishing systematic error for any finite extraction radius, and if so, by how much. We used data from the lower resolution run that we already analyzed in the previous section. The accuracy of the frequency does not change significantly if we use the higher resolution run instead.

The angular part of the initial data is a pure $\ell = 2$, $m = 0$ mode. Since the background has no angular momentum, there is no mode–mode coupling at the linear level, while nonlinear coupling can be neglected for the current study, because we only evolve weak perturbations. Therefore the only dominant multipole mode present in the data at all times should be the one injected initially. At the numerical level, $\ell = 4$ modes can be generated by our six-block grid structure. However, in [64] it was found that in the absence of angular momentum, these modes not only converge to zero with resolution, but are also very small for the resolutions considered in this study. In the above reference and in [25] it was also shown that overtones are not significantly excited unless the black hole is very rapidly rotating. Based on all this, we only fit for a single $\ell = 2$, $m = 0$ mode:

$$\Psi_{RW}^{fit} = \mathcal{A}\sin(\omega_r t + \chi)\, e^{\mathrm{i}\omega_i(t-t_0)} - \xi \tag{3.37}$$

where $\mathcal{A}$ is the excitation amplitude, $\omega = \omega_r + \mathrm{i}\omega_i$ is the complex quasinormal mode frequency, χ is a phase shift, ξ is the offset and t_0 is the starting time of

the quasinormal ringing regime. The latter is not unambiguously defined (the so called "time-shift problem"), and as a consequence neither are the amplitudes of quasinormal modes. In ref. [64] it was proposed to minimize the uncertainties due to this time-shift problem by looking at carefully chosen relative amplitudes (see that reference for details). In order to fit numerical data to eq. (3.37), we fix t_0 to an educated guess[7] and then fit for ω, $\mathcal{A}$, χ, and ξ. Any difference in t_0 is absorbed in $\mathcal{A}$ (in which we are not interested at this point) and does not change the other extracted parameters. We find the time-window of optimal fitting by looking for a local minimum in the relative residual between the original waveform and its fit. In ref. [64] it was found that such a local minimum is usually quite sharp and therefore gives a good criteria for choosing the window of time where the quasinormal ringing dominates. Similarly, we use the uncertainties in this minimum to quantify the errors in the parameters obtained in the fit. More details about the fitting procedure that we use to extract quasinormal parameters are given in ref. [64].

In the previous subsection we discussed the presence of an offset in the extracted waves with the standard method. If such an offset is not taken into account when fitting for the quasinormal frequencies (i.e., for a fixed $\xi = 0$), eq. (3.37) does not represent the behavior of the numerical data well enough, and no reasonable results can be obtained from the fit. This is especially the case at medium to late time intervals when the amplitude becomes smaller than the offset, so that the wave does not cross zero any more. When one tries to fit for these cases, the obtained

---

[7]For example, taking into account where the initial data and observer are located, and assuming a propagation speed of one.

Extraction Method	ω	relative error
Generalized RW	$0.3736 - 0.0890\mathrm{i} \pm (3 + 3\mathrm{i}) \times 10^{-4}$	$1.9 \times 10^{-4} + 4.5 \times 10^{-4}\mathrm{i}$
RW Min	$0.3733 - 0.0889\mathrm{i} \pm (3 + 3\mathrm{i}) \times 10^{-4}$	$9.9 \times 10^{-4} + 6.7 \times 10^{-4}\mathrm{i}$
RW Sch	$0.3733 - 0.0889\mathrm{i} \pm (3 + 3\mathrm{i}) \times 10^{-4}$	$9.9 \times 10^{-4} + 6.7 \times 10^{-4}\mathrm{i}$

Table 3.2: Quasinormal frequencies of the $\ell = 2, m = 0$ mode as measured by an observer at $r = 20\,M$. Results are given for waveforms resulting from the different extraction methods we use. The predicted frequency from perturbation theory, which we assume to be exact because our perturbation amplitude is small, is $\omega_{\mathrm{exact}} = 0.37367 - 0.08896\mathrm{i}$ [109]. The uncertainties in the extracted frequencies originate from variations in them depending on which interval of the waveform is used for the fit. The relative error is defined as $|(\omega - \omega_{\mathrm{exact}})/\omega_{\mathrm{exact}}|$.

frequency has no relation at all to the correct QNM frequency. For example, at $r = 20M$ the offset in the waves obtained from the standard RW wave extraction is of order 10^{-2} for both a Minkowski background and for Schwarzschild–like coordinates. Without taking the offset into account, the value of ω_r that the fit determines lies between 10^{-14} and 10^{-4}, and ω_i is of order 10^{-3} to 10^{-6} (compare to table 3.2). In contrast, the offset resulting from the generalized RW wave extraction is of order 10^{-5} for this resolution. This is small enough that the problems described above do not play a noticeable role.

Table 3.2 shows the complex quasinormal frequencies that we obtained from the generalized and from the standard RW methods. As mentioned above and discussed in detail in ref. [64], the error bars are estimated from changes in the frequency when changing the time interval that we use for the fit of the waveform. We assume that the predicted frequency from perturbation theory for the fundamental

$\ell = 2$, $m = 0$ mode is exact because we use a small amplitude for our perturbation. This frequency is known to be $\omega_{\text{exact}} = 0.37367 - 0.08896i$ (see for example [109]). The frequency obtained from the new generalized wave extraction is consistent with this exact value within the accuracy to which we can obtain these numbers from the fit itself. For the standard wave extraction method, we only find agreement to three significant digits in the real part, but better agreement with the exact value in the imaginary part of the waveform. Note that, since the waveforms only differ by a constant factor (see subsec. 3.4.2), the frequencies obtained with a Minkowski and a Schwarzschild background agree to roundoff error. The reason for the lower accuracy in the real part of ω might be due to the fact that the waveforms are slightly distorted due to the wrong assumption for the background metric. This causes a larger residual between the data and the fit—it is about a factor of two larger than with the generalized wave extraction—and some degradation in how accurately certain fitting unknowns like ω can be determined. That may also explain the larger relative error for the waves extracted with the standard RW wave method, which is shown in the right column of the same table. There the relative error is defined as $|(\omega - \omega_{\text{exact}})/\omega_{\text{exact}}|$.

3.5   Final comments

When considering methods for extracting gravitational waves from numerical spacetimes at a finite distance, one question of direct interest is: How sensitive is the accuracy of the extracted waveforms to both the extraction method and observer

location? In particular, how far away is "far enough" when extracting gravitational waves?

It is in general not easy to pose such a question in a precise way, since in order to quantify this one needs an exact waveform to compare with. This exact waveform is in principle only well defined at future null infinity. However, there are some particular scenarios of interest where the concept of "exact waveforms" at a finite distance can be given a well defined and precise sense. That is the case, for example, for perturbations of Kerr black holes (actually, of Petrov type D spacetimes): the Weyl scalar Ψ_4 is defined everywhere in an essentially gauge and tetrad invariant way [59]. Similarly, for perturbations of Schwarzschild black holes, the Regge–Wheeler and Zerilli functions are defined in a gauge invariant way everywhere as well. In fact, there is a one-to-one mapping between these functions and Ψ_4; see e.g. [149].

Therefore the above question can be posed in a setting that might not be the most general one, but it is one in which a precise, quantitative answer can be found. The concrete setting that we chose for the current study is that of weak perturbations of Schwarzschild black holes. Furthermore, in this study we restricted our treatment to odd parity perturbations (the even parity sector will be presented elsewhere). One of the standard methods that has been widely used for extracting gravitational waves from such spacetimes is through the standard Regge–Wheeler– Zerilli perturbation formalism. This formalism provides a gauge invariant treatment of perturbations of a background geometry defined by the Schwarzschild spacetime *in Schwarzschild coordinates.* That is, the formalism is invariant with respect to

94

linear coordinate transformations *which leave the background coordinates fixed*. If one extracts waves using this formalism from a perturbation of Schwarzschild in, say, Kerr–Schild coordinates, the extracted waves at a finite distance will not be correct, even if extracted with infinite numerical precision. There is a systematic error in such an extraction, due to the incorrect identification of the background coordinates. Of course, one expects this error to decrease as the extraction radius increases. In the spirit of the above discussion, the question that we asked ourselves was: how far away must the observer be, so that the difference between the exact waveform and the extracted one is negligible, if the extraction method has a systematic error? For this study we chose a very specific interpretation of "negligible systematic errors in the waveforms", namely, that they are smaller than or comparable to the errors in these waveforms due to the numerical discretization.

In order to provide a quantitative answer to this question, in this study we first proceeded to generalize the standard Regge–Wheeler extraction approach by using a perturbation formalism that allows for quite general slicing conditions for the Schwarzschild background. With this generalization, if one calculated with infinite resolution, one would extract the exact waveforms for *any* (not necessarily large) finite extraction radius. This holds even if the Schwarzschild background is, for example, given in a time dependent slicing, or one in which the coordinates in a neighborhood of the horizon are well defined, as is usually the case in numerical black hole evolutions.

After summarizing the basics of the generalized formalism, we described our numerical implementation of the generalized extraction mechanism and our way of

solving Einstein's equations. For the latter we used multiple blocks and high order methods, both of which present several advantages. Of particular interest to this study is that, due to the adaptivity that multiple blocks provide, the outer boundary can be placed at large distances, with much smaller computational costs than with Cartesian grids and mesh refinement. We made use of this specific advantage and performed three-dimensional non-linear simulations of weakly distorted Schwarzschild black holes, from which we extracted waves at distances larger than most current state of-the-art three-dimensional simulations of Einstein's equations.

Then we studied the dependence of the extracted waveforms on the extraction method. More precisely, we compared the standard RW method with our generalized one. We found that, even for the coarsest resolutions that we used, the errors in the waveforms from the standard method were dominated by the extraction procedure and not by the numerical accuracy of the spacetime metric. Furthermore, by increasing the resolution we could explicitly demonstrate that the errors in the standard method do not approach zero, while they do with the generalized one. While this is obviously the expected behavior on analytical grounds, we emphasize that we could explicitly see these differences even with an extraction radius which is significantly larger than those typically used in current state-of-the-art three-dimensional simulations.

What is not clear, however, is whether the wave zone resolution currently used by mesh refinement codes is sufficient to see the differences that we have demonstrated in this study. For example, the spatial resolutions in the wave zone of current binary black hole inspiral and coalescence simulations are usually much coarser than

96

the resolutions that we used above. Some radial resolutions h in the wave zone of binary black hole system simulations are: [20] $h = 0.5\,M$, [90] $h = 0.5\,M$ (but the extraction is performed very close in at $R = 16M$) [19] $h = 0.75\,M$ (but $h = 1.5\,M$ for calculating the radiated angular momentum J), [139] $h = 0.85\,M$, [161] $h = 0.87\,M$ [44] $h = 0.82\,M$, [41] $h = 0.56\,M$, [81] $h = 0.56\,M$. Some of these codes are 4th order accurate, but many have at least certain components that are only 2nd order accurate.[8]

One of the interesting features of the waveforms that we extracted in this study with the standard method is that we were able to "post-process" them in order to remove an offset at late times. By doing so, we could accurately extract the quasinormal frequencies. However, we explicitly demonstrated that the large errors in the standard method were not due to an overall offset in the whole wave. Even after removing the offset "by hand", errors of roughly the same order in the waves remained at early and intermediate times in the ringing regime. In addition, this post-processing made use of the fact that we knew the qualitative behavior of the exact solution in the quasinormal ringing regime. In particular, we knew that it had to oscillate around zero, and we also knew what the frequencies they were supposed to have. It is not clear that one could apply such a post-processing to

_____

[8]While it is currently common practice to report the finest resolution (near the horizons) and the coarsest resolution (near the outer boundary) in such simulations, the resolution in the wave zone, i.e., at the location where the gravitational waves are extracted, is often not explicitly listed, and can sometimes not be inferred. Some publications also do not report at which coordinate radius the wave information is extracted.

decrease systematic errors in a more general scenario, where the characteristics of the expected waveforms are either completely unknown or not known with so much detail.

Concluding, in this study we considered weak perturbations of Schwarzschild black holes, for which—as mentioned above—one can construct the Regge–Wheeler and Zerilli functions (or, equivalently, Ψ_4) in an unambiguous way *everywhere*. In a more generic case (say, a collision of compact objects) this is not possible, and all gravitational wave extraction methods are inherently approximate at a fixed finite distance. The results of this study suggest that, depending on the accuracy of a given simulation, different choices in the extraction procedure at a fixed and finite distance may result in relative differences in the waveforms that are actually larger than the numerical errors of the solution. These differences will in general decay with radius, but in a very slow way; typically as $1/r$ (which is, in fact, the decay we found in our simulations). For example, in order to decrease the systematic errors for an observer at $40\,M$ shown in fig. 3.7 by, say, two orders of magnitude, by just moving the observer out and extracting at a single extraction radius, the latter would have to be located at $\simeq 4,000\,M$. This means that, if similar uncertainties show up in other simulations for differing extraction methods, as the results of this study suggest (and which can be tested), then decreasing those uncertainties by extracting waves at a *fixed* location and moving the observer further out does not seem feasible, and other ideas would have to be explored.

Chapter 4

Orbiting binary black hole evolutions with a multipatch high order

finite-difference approach

4.1 Introduction

Mergers of binary compact objects (neutron stars or black holes) are expected

to be the main sources of gravitational waves for the ground-based interferometric

detectors LIGO, GEO, VIRGO, and TAMA. Neutron star-neutron star and black

hole-neutron star binaries are also interesting because they are leading candidates

for explaining the production of short-duration gamma-ray bursts and because grav-

itational wave signals from these events may encode information about the neutron

star equation of state [130, 141, 171]. Such a merger can be accurately modeled only

by the numerical evolution of the full Einstein field equations coupled (if a neutron

star is present) to an evolution of the neutron star matter.

Because of advances in numerical relativity in recent years, stable evolutions

can now be performed for most binary cases. Accuracy and speed are now the press-

ing numerical challenges: how to achieve the minimum error given limited time and

computational resources. A good code should converge rapidly with increasing reso-

lution to the exact solution. Its speed should scale well with the number of processors

used in order to make good use of parallelization. Also, an efficient use of resources

will require a grid well adapted to the problem at hand. This includes using a grid with the most appropriate shape. For example, it is reasonable to suppose that excision inner boundaries and outer boundaries should be spherical. A good grid will also use higher resolution where it is most needed. For example, although the grid must extend out into the wave zone to extract the gravitational wave signal, lower resolution is needed in the wave zone than is needed in the vicinity of a black hole or neutron star. The need for high resolution in neutron stars and black hole accretion disks can become particularly acute in cases of hydrodynamic or magnetohydrodynamic instabilities, such as convective, Kelvin-Helmholtz, or magnetorotational instabilities. In such cases, the length scale of the unstable modes can be much smaller than the radius of the star or disk, and the evolution will be qualitatively wrong if the instability is completely unresolved.

One technique that has been successfully used to deal with this problem is adaptive mesh refinement (AMR) [176, 16]. These AMR codes generally use overlapping Cartesian meshes of varying levels of refinement, with the finer meshes being used only where they are determined (by some algorithm) to be needed. We present a different method of achieving efficient grid coverage, one that is algorithmically simpler and that possesses some unique advantages.

This different technique for evolving binary compact systems involves using multiple grid patches, each patch having its own shape, curvilinear coordinates and resolution. The basic ideas behind these multipatch methods have been worked out in earlier papers [112, 62, 154]. In these references some particular patch configurations using cubes and cubed-spheres were used. The cubed-sphere patches were

used to construct grids with exactly spherical inner excision boundaries and outer boundaries. These methods are, hence, ideal for calculations that involve excision. (Using AMR with excision introduces a number of complications.) These techniques were then successfully used to simulate perturbed Kerr black holes [64, 132]. Multiple patches in cubed-sphere arrangement have also been used to evolve the shallow water equations [147] and to simulate hydrodynamic flows in black hole accretion disks [103, 181, 73].

Another multipatch approach has been used by the Cornell-Caltech group to evolve Einstein's equations for binary black hole [153] and black hole-neutron star [67] systems. In the binary black hole case derivatives in these simulations are computed pseudospectrally, rather than using finite differencing. While pseudospectral methods produce accurate results very efficiently for binary black hole evolutions, they are much less cost effective for systems involving matter. One reason for this is that the discontinuities that naturally appear in the fluid flow at shocks and stellar surfaces destroy the exponential convergence of spectral methods. In fact, the Cornell-Caltech group found it necessary to evolve the fluid variables using finite differencing, while evolving the field variables pseudospectrally. This required two independent grids: the finite difference gridpoints used to evolve the fluid, and the collocation points of the pseudospectral code used to evolve the metric. For the two grids to communicate, variables had to be interpolated from one grid to the other each timestep, a process which consumed about one third of the CPU time in each simulation. Another problem with pseudospectral techniques is that they usually do not scale well to large numbers of processors. In regions with-

out discontinuities, where spectral convergence is not lost, one cannot, for example, split one large domain into two domains with half the number of collocation points each without a significant loss in accuracy. On the other hand, accurate simulations of binary neutron star or black hole-neutron star mergers are not practical without many processors.

It would therefore seem preferable to evolve both the fluid and the metric with finite differencing. This could significantly improve the scalability, allowing simulations on hundreds or thousands of processors. It would also remove the need for two separate grids and the expensive interpolation between them. Multipatch techniques are the natural finite difference version of the Cornell-Caltech pseudospectral evolution algorithm. As a first step in that direction, here we evolve a binary black hole system using multipatches together with high order finite-differencing operators. We show that our code converges rapidly, scales well to thousands of processors, and can stably simulate several orbits of the inspiral.

4.2   Evolution equations

At the continuum level, the techniques used here are exactly those ones previously used by the Caltech-Cornell collaboration in binary black hole simulations. We use the first order form of the generalized harmonic system presented in [113]. The evolution variables in this formulation are the 4-metric g_{ab} and its first derivatives in space and time $\partial_c g_{ab}$. (The indices run from 0 to 3.) We use the constraint preserving boundary conditions of [113, 144, 145]. The evolution of the gauge is determined

by the gauge source functions $H_a = -g^{cd}\Gamma_{acd}$, which are freely specifiable functions of space and time. In this study, the gauge is set by choosing H_a to be constant in time in a coordinate system that comoves with the holes. This comoving coordinate system is determined using the same dual frame and control tracking mechanism as was used for the spectral binary black hole evolutions [152]. This technique uses two coordinate frames, which we label $x^{\bar{i}}$ and x^i. The coordinate frame $x^{\bar{i}}$ is set to be an asymptotically flat, inertial frame. All tensor components are evaluated with respect to this frame. The gridpoints are fixed in the computational frame x^i. By means of a mapping between the frames, the computational coordinates can be made to approximately comove with the system. For the runs presented here, we track the binary using a simple combination of rotation and radial scaling:

$$\bar{t} = t \tag{4.1}$$

$$\bar{x} = a[x\cos(\theta) - y\sin(\theta)] \tag{4.2}$$

$$\bar{y} = a[x\sin(\theta) + y\cos(\theta)] \tag{4.3}$$

$$\bar{z} = az \, , \tag{4.4}$$

where θ and a are functions of time which are evolved using a feedback mechanism to keep the location of the black holes fixed in the computational domain.

The differences between the simulations presented here and the earlier spectral simulations are in the type of domain decomposition, and in the numerical techniques used to compute the right-hand sides of the evolution equations (e.g. how spatial derivatives are approximated). Our handling of these issues is described below.

103

4.3   Initial Data

The initial data that we use here consists of a snapshot at a given time of the highest resolution 16-orbit simulation done by the Caltech-Cornell collaboration, which corresponds to the run 30c1 reported in Refs. [30, 153]. The starting time $t = 0$ in our simulations corresponds to the instant $t = 2887\,M$ of the 16-orbit simulation (with M being the sum of the irreducible masses of each black holes). From that point, the black holes orbit for about 6 orbits before merger, although our runs stop before the merger takes place.

This way of specifying the initial data has the advantage that there is no junk radiation present in the computational domain at our starting time. Since the domains and points used here are different from those used in the spectral simulation, we spectrally interpolate the initial data to the multipatch domain.

The outer boundary of our domain is a sphere of radius $r = 144\,M$. This value is actually mapped to $r' = 105\,M$ by the dual-frame coordinate transformation, which scales and rotates the inertial coordinates into the comoving ones. The coordinate transformation is a simple rescaling of the radial coordinate $r' = a(t)r$ by a time dependent factor, and a rigid rotation about the z axis. Since the binary system has been evolving before our $t = 0$ time, the scale factor has a value $a = 0.727$ and the rotation angle is $\theta = 57.95$ radians at the beginning of our simulations. The black hole coordinate separation at the beginning of the 30c1 run is $14.44\,M$. At our time $t = 0$ the initial coordinate separation is $10.5\,M$.

4.4　Multi-block domain

4.4.1　Structure

We use two types of basic building patches to cover the whole computational domain. One is simply a cuboid with a Cartesian coordinate map. The other is a combination of six patches that we call a *juggling ball*. A juggling ball can assume two different configurations. The first of them is shown at the top of Fig. 4.1. It consists of a cube whose interior has been excised by a sphere. We will refer to it as an *inner* juggling ball because it is the one that we use to excise the interior of each black hole and to cover its immediate surroundings. The second configuration is shown at the bottom of Fig. 4.1 and consists of a sphere whose interior has been excised by a cube. We will call it an *outer* juggling ball because it is the one that covers the region away from the black holes, reaching to the outer boundary. Both types of juggling balls use a radial coordinate that adjusts smoothly to their geometry. Each surface of constant radial coordinate is endowed with six two-dimensional coordinate maps, in the same fashion as the cubed sphere [147]. In essence, the juggling ball is a collection of six patches, each of them topologically equivalent to a cube.[1]

The basic layout of the full domain used here is shown in Fig. 4.2. The centers of the excised spheres (which will be inside each black hole) are located along the x axis at $x = \pm a$. Here we have used two inner juggling balls, one around each black hole. Their individual outer boundaries are cubes with sides of length $2a$. When

---

[1]The name juggling ball was chosen because some real juggling balls have a set of six quadrilateral-shaped designs on their surface.
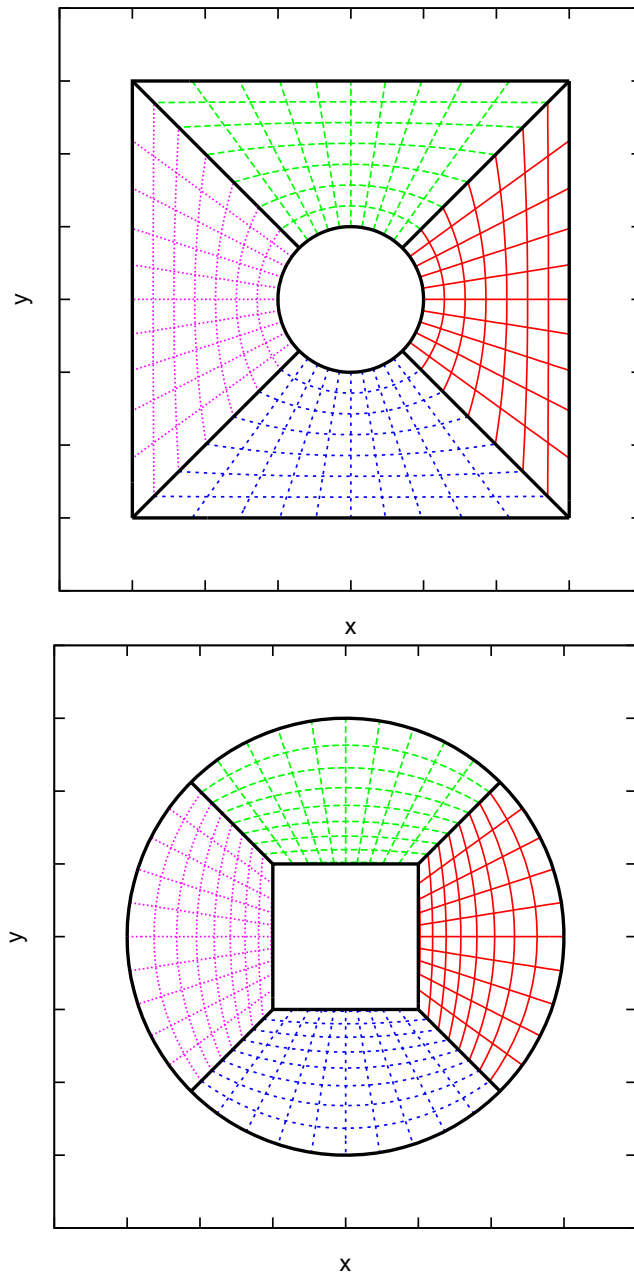
Figure 4.1: Equatorial cross-section of an inner juggling ball (top). Black lines denote the block boundaries. Colored lines represent the coordinate grid of each block. Equatorial cross-section of an outer juggling ball (bottom).

they are put together, we end up with a cuboid of dimensions $4a \times 2a \times 2a$, with the longest side along the x axis. We surround this structure with six cuboid patches of dimensions $4a \times 2a \times a$, aligning them along the y and z axes. After doing so, we end up with a cubical domain with sides of length $4a$. To complete the patch system we add an outer juggling ball whose cubical interior holds the two inner juggling balls plus the six cuboids. The outer juggling ball enables us to shape the outer boundary into a sphere, in which case moving the boundary further out requires an increase in the number of grid points that scales as $O(N)$ (as opposed to $O(N^3)$).

The total number of patches in this basic configuration is 6 cuboidal patches + 6 $\times$ (3 juggling balls) = 24 patches.

None of the patches used here overlap with any other (in which case they are usually called *blocks*). A given block communicates with adjacent ones only by the two-dimensional common surface between them. Accordingly, we handle parallelization by assigning one block per processor, in this way minimizing communication between processors.

In this basic 24-block domain case, we would use exactly 24 processors, which is a fairly small number for a binary black hole simulation. In order to achieve higher resolutions by increasing the amount of points per block, we subdivide the existing blocks into smaller pieces. Since the topology of each block is cubical, it is straightforward to subdivide them. The guiding principle that we use to accomplish the subdivision is to keep the same number of points per block for every single block. Although this condition is not necessary, it is convenient because it balances the computational load across all the processors.
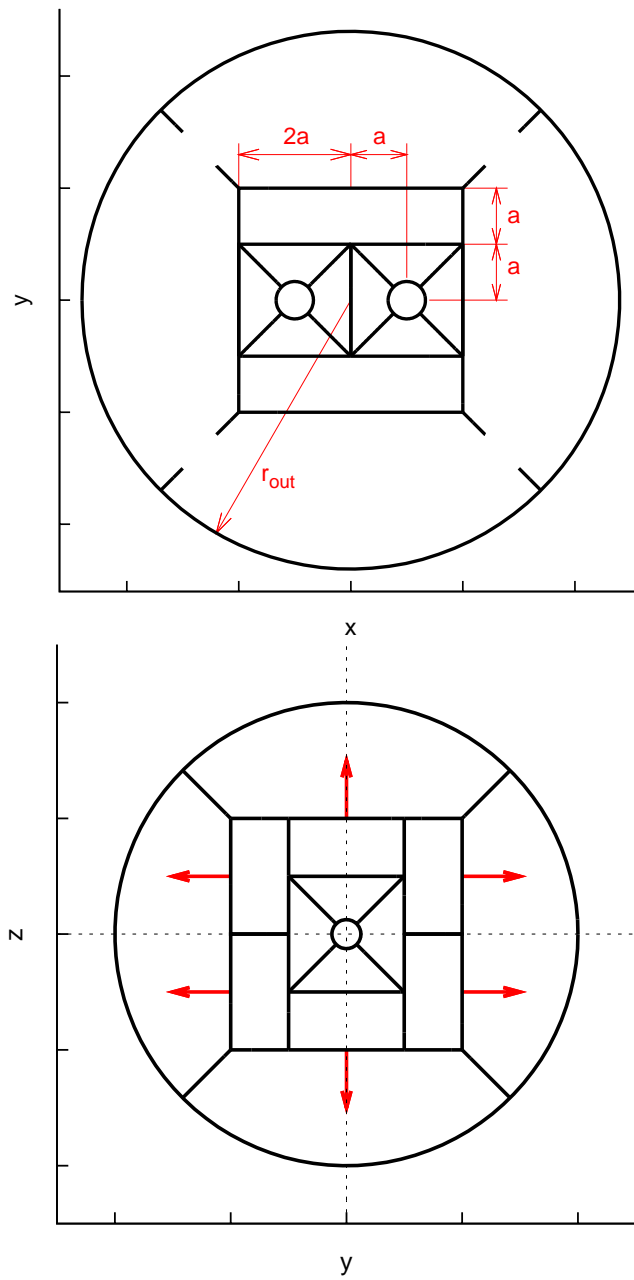
Figure 4.2: Equatorial cut of the computational domain (top). Schematic figure showing the direction considered as radial (red arrows) for the cuboidal blocks (bottom).

For the runs presented here, we used 192- and 384-block domains. The first case is obtained by subdividing the inner juggling balls uniformly in the radial direction 7 times. The 6 cuboids are split by a factor of 2 and the outer juggling ball is divided 4 times in the radial and twice in each transverse direction. The 384-block case is derived from the 192-block one by further split of each block in the radial direction by a factor of 2.

Figure 4.3 shows the multipatch structures used in this study.

4.4.2   Numerical techniques

In our simulations we use the D_{8-4} summation-by-parts (SBP) finite difference operator and its associated dissipation constructed in [62]. The naming convention is meant to indicate that the derivative is 8th order accurate in the bulk of each block but only 4th order accurate near inter-block boundaries. The derivative in the interior of each block is a centered one and is modified near boundaries so as to satisfy the SBP property with respect to a diagonal norm; this is the cause of the drop in convergence. Information across sub-domains is communicated using characteristic variables and a penalty method (see [112, 62, 154] for more details).

The combination of these techniques guarantees numerical stability, but at the expense of the drop in convergence order near boundaries. For example, in the D_{8-4} case there are eight points near *each* boundary where the scheme is fourth order. For technical reasons explained below, in the simulations presented here, we use a rather large number of blocks and processors (192 and 384), with a very small load on each.
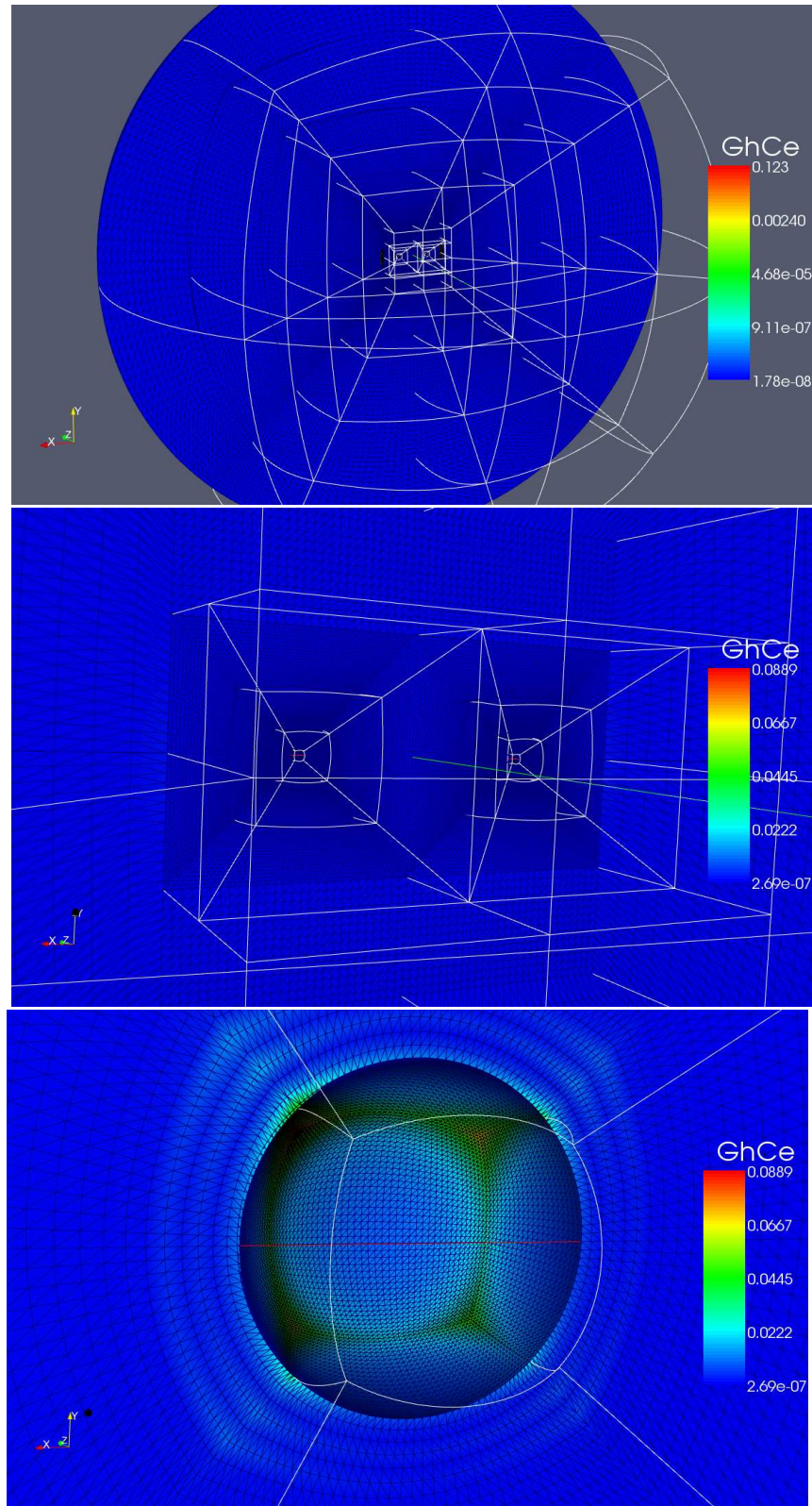
Figure 4.3: Computational domain used in the simulations of this study.

As a consequence, the scheme is fourth order nearly everywhere and we expect our simulations to be 4th order convergent. This is indeed what our simulations below show.

4.4.3   Resolution

One of the features that a multipatch method offers is the flexibility to increase only the radial resolution while keeping the angular resolution constant. Given that the angular profile of the waveforms is dominated by a few low-ℓ modes, once a sufficient angular resolution is used the truncation error will be dominated by the radial resolution.

The approximate spherical symmetry in the vicinity of each black hole and at large distances from them allows the radial direction to be naturally defined for each juggling ball block. However, for the cuboidal blocks there is some arbitrariness in how to choose the radial direction. In practice, a radial direction for these blocks is useful only to define the direction along which resolution will be increased. In Fig. 4.2 the radial directions for the cuboidal blocks are indicated with arrows.

We use an angular resolution of $\pi/58$ around each black hole and twice as much in the outer blocks. That is, there are 116 points along an equatorial line around each black hole and twice that number in the distant wave region. This is somewhat inefficient since the solution is over-resolved in the angular directions compared to the radial one (especially in the wave region). The motivation behind this choice was to allow the grid points at the boundary faces of adjacent blocks to be

$N_r \times N_{\mathrm{ang}} \times N_{\mathrm{blocks}} = N_{\mathrm{total}}$	speed (h^{-1})	CPU (h)
$19 \times 29^2 \times 192 = 145^3$	2.83	67844
$22 \times 29^2 \times 192 = 153^3$	1.86	103226
$16 \times 29^2 \times 384 = 173^3$	2.42	158678

Table 4.1: Speed and CPU time for three resolutions. N_r and N_{ang} are the radial and angular number of points per block, respectively, as described in the text. The speed is expressed in units of the total irreducible mass per hour.

in one-to-one correspondence with each other. In this way the communication of the characteristic modes at the inter-patch boundaries does not require interpolation.

In Table 4.1 we show the total number of points in the whole domain and per block for the simulations of the present study. We increase resolution only along the radial direction, by the same number of points in all the domains. In our setup all blocks have the same number of points. Since parallelization is handled by assigning one block per processor, this guarantees a homogeneous load distribution.

The number of points shown in Table 4.1 is actually not large for a fully three-dimensional (i.e. no symmetries imposed) finite-difference simulation. For example, we can compare these numbers to a binary black hole evolution with around the same number of orbits using Cartesian grids and adaptive mesh refinement [91]. A typical state-of-the-art simulation uses six refinement levels around each black hole with 64^3 points on each level, and four coarse grid levels with 128^3 points. This amounts to a total of $2 \times 6 \times 64^3 + 4 \times 128^3 \approx 226^3$ points. In the case of non-spinning, equal-mass black holes one can make use of the symmetry of the problem
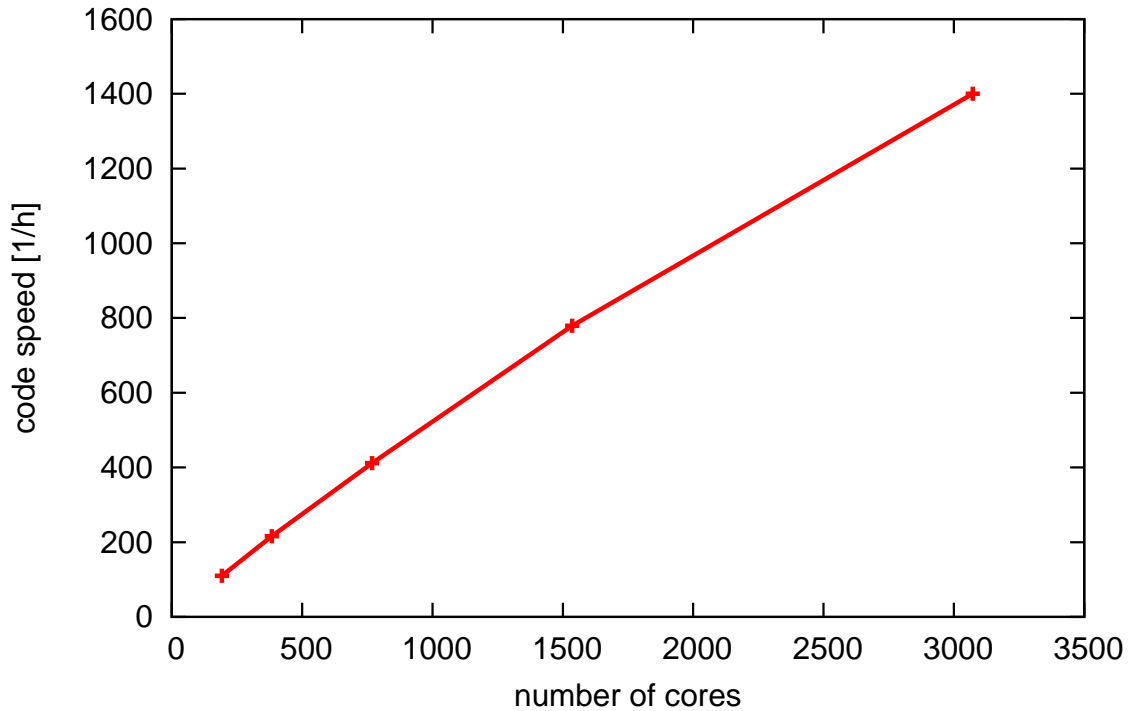
Figure 4.4: Strong scaling test for a single black hole. The speed of the code depends essentially linearly on the number of processors, almost perfect scaling. Here we keep the global amount of points fixed. The performance becomes faster as the whole domain is distributed among more processors.

and reduce the total number of points to $6 \times 64^3 + 128^3 \approx 154^3$.

We have tested the performance of our multipatch parallelization scheme for the evolution of a single black hole. In Fig. 4.4 we show a strong scaling test for up to $3,000$ processors (cores), in which the total number of points is kept fixed while increasing the number of processors. We see that the speed of the code has a linear dependence on the number of processors. Similarly, in Fig. 4.5 we show a weak scaling test, where the load per processor is kept fixed while increasing the number of processors used. The drop in speed in this case is about 15% over a range of 10
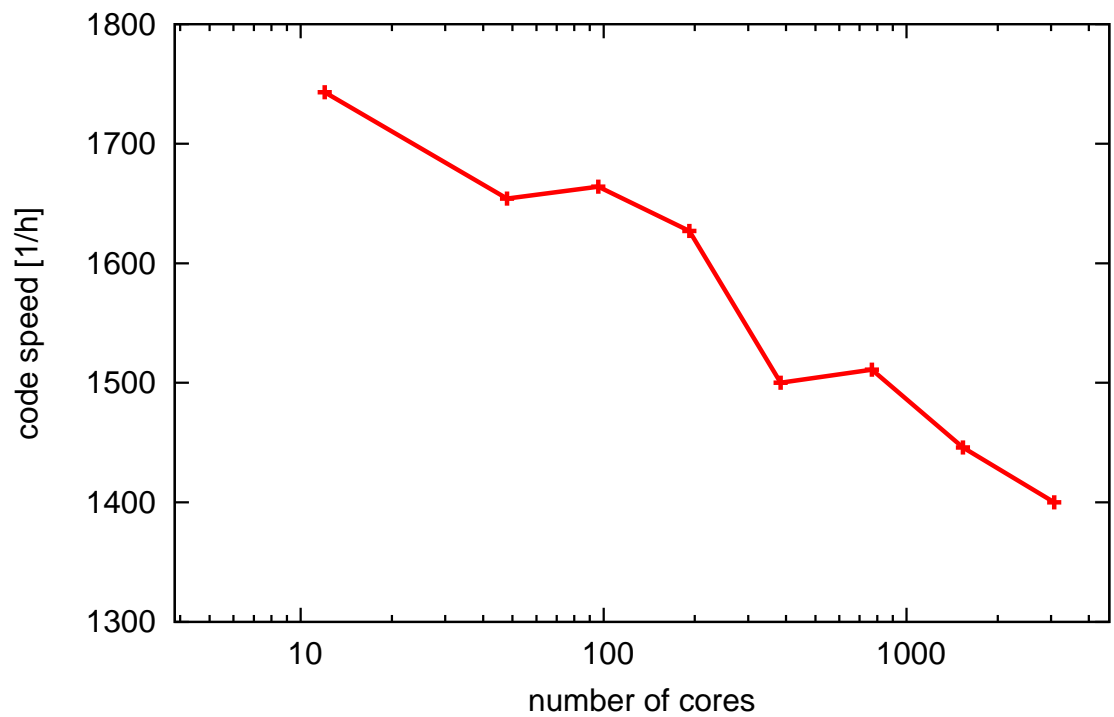
Figure 4.5: Weak scaling test for a single black hole. There is only a 15% drop in speed as the number of processors is increased while keeping the load per processor fixed. The decrease in speed is due to the larger amount of communication between processors.

to 3,000 processors. We have not attempted to go beyond this number of cores.

The phase errors in the waveforms shown in the next section are rather large compared to state-of-the-art simulations (in particular, compared to an AMR one such as the one mentioned above). Since the code scales well and the number of points used here (shown in Table 4.1) is reasonable for a finite-difference evolution, in principle we could improve the accuracy of the simulations shown in the next section while still using modest computational resources. What has prevented us from doing so is a purely technical obstacle. The computational infrastructure used here, SpEC, was originally designed for pseudo-spectral evolutions, which are extremely efficient in terms of memory. For that reason SpEC currently stores in memory many more variables than are actually needed for evolving the system. As a result, in our FD simulations because of memory constraints we actually end up using a few cores per node and a rather large number of nodes. We plan to improve SpEC's use of memory soon to eliminate this limitation. However, for the demonstrations shown here, the current resolutions are sufficient.

4.5 Results

Figure 4.6 shows the location of the centroids of the apparent horizons for the highest resolution simulation. The black holes complete about six orbits before reaching the merger regime.
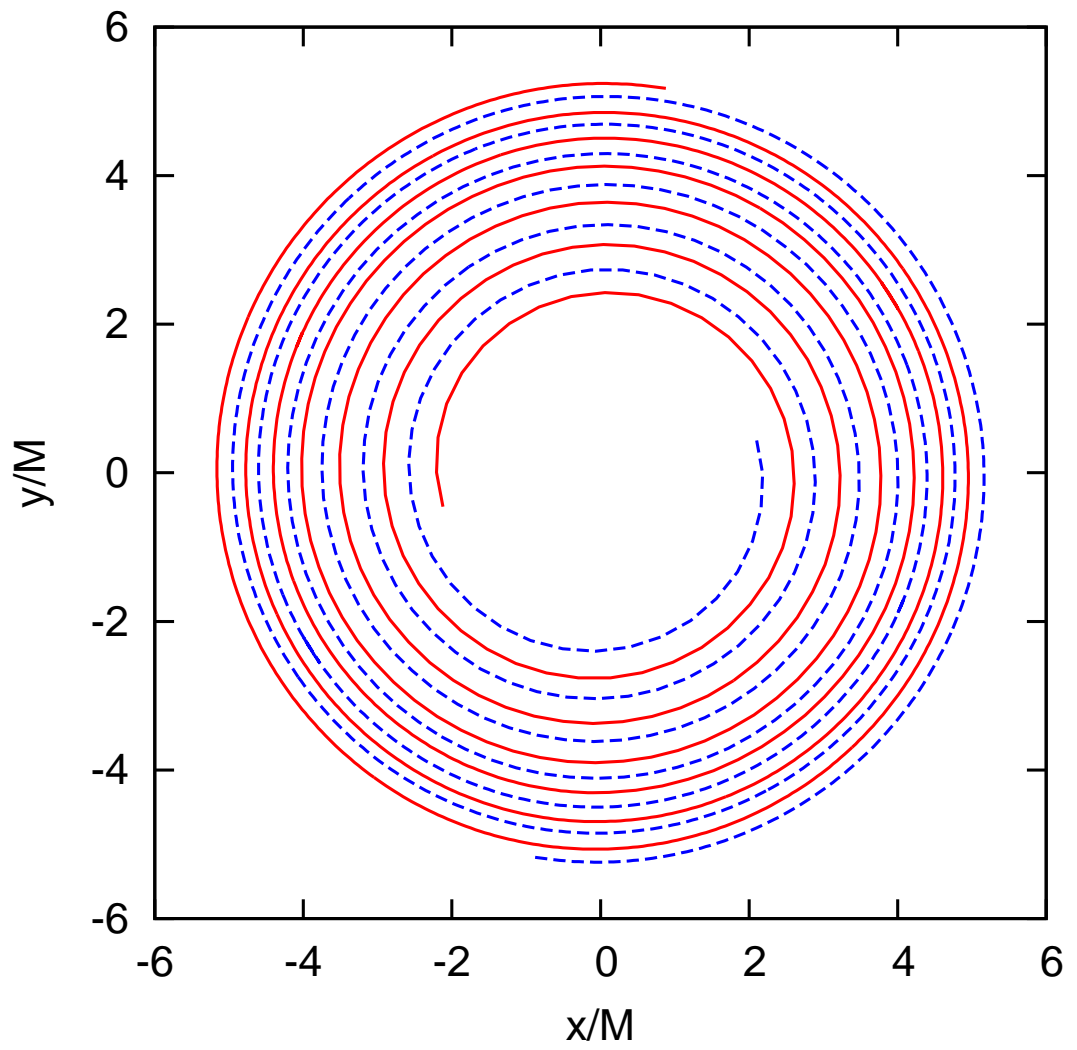
Figure 4.6: Black hole orbits.
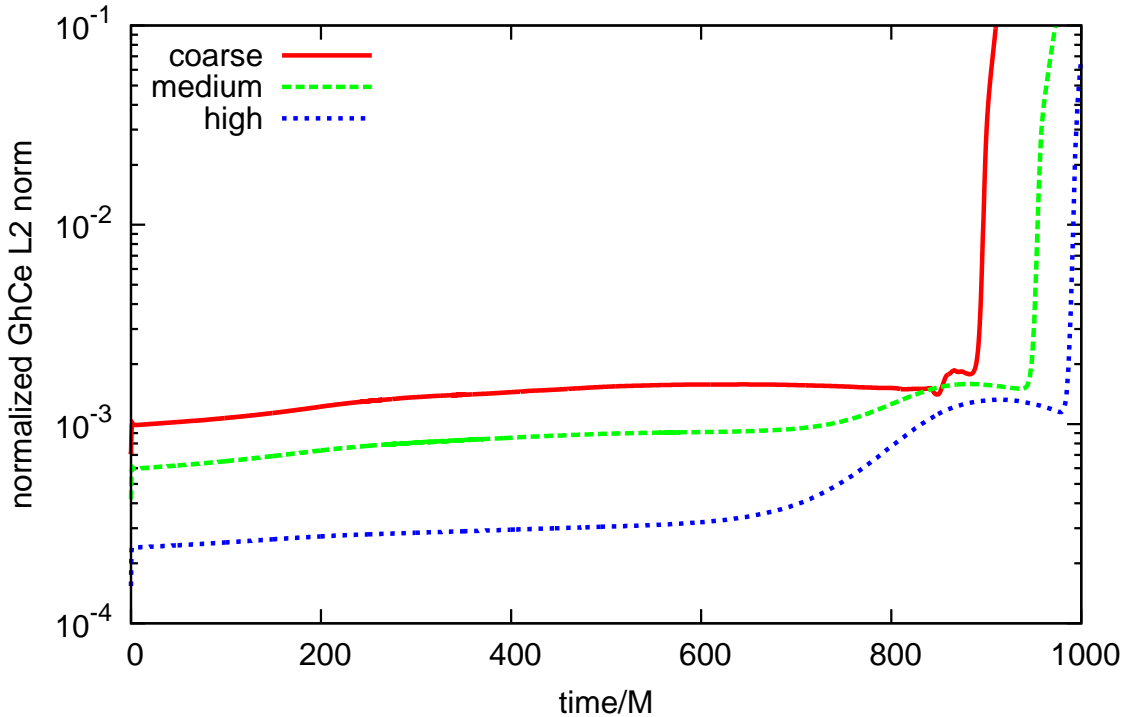
Figure 4.7: L^2 norm of the normalized constraints.

4.5.1 Convergence of the constraints

A way of checking the consistency of the numerical solution is monitoring the constraint violations, since they are not enforced during the evolution. In Fig. 4.7 we plot the L^2 norm of all the constraint fields of the first order generalized harmonic system, normalized by the L^2 norm of the spatial gradients of the dynamical fields, as defined in [113]. We show three runs with different resolutions.

Figure 4.8 shows the convergence exponent of the L^2 norm of the normalized constraint violations, which is around four, as expected (cf. Sec. 4.4.2). The convergence exponent n is defined as

$$\frac{\beta^n - 1}{\beta^n - \alpha^n} = \frac{C_1 - C_3}{C_2 - C_3} \qquad (4.5)$$
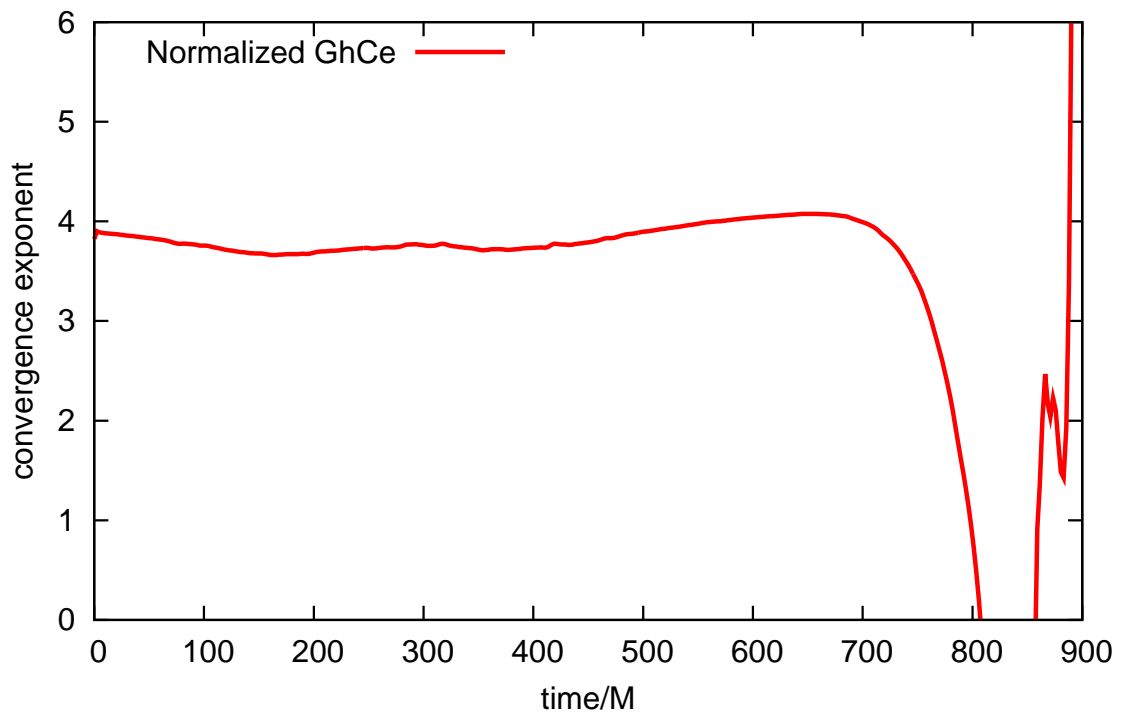
Figure 4.8: Convergence exponent for the L^2 norm of the normalized constraints.

where α is the ratio between the medium and coarse resolution and β, the ratio between the fine and coarse one. C_1, C_2, and C_3 represent a given quantity at coarse, medium and fine resolutions, respectively.

The uniform convergence is lost around $t \sim 800\,M$, at which time the values for the coarse and medium resolutions intersect, as is seen in Fig. 4.7.

We stop our simulations when the characteristic speeds at the excision boundary change sign, which means that there is spurious information entering the domain. That moment is characterized by a blow-up of the constraints. This feature is due to the inadequacy of the rather simple gauge conditions used here at times close to merger. At the time the simulations presented here were performed, we used the same simple conditions used then by the Caltech-Cornell collaboration, namely, keeping the gauge source functions fixed in the comoving frame. Since then, better conditions have been developed, which do allow simulations to go through merger and ringdown [153]. For the purposes of this presentation, however, following six orbits of an inspiral is sufficient.

4.5.2   Waveforms

Waveforms are computed via the Newman-Penrose curvature scalar Ψ_4 as in [134]. Subsequently we decompose Ψ_4 in spin-weighted spherical harmonics $_{-2}Y_{\ell m}(\theta, \phi)$. We focus our discussion to the $\ell = 2$, $m = 2$ mode. The extraction is done at $r = 50\,M$.

Figure 4.9 shows the real component of Ψ_4. We see that they all agree at early

119
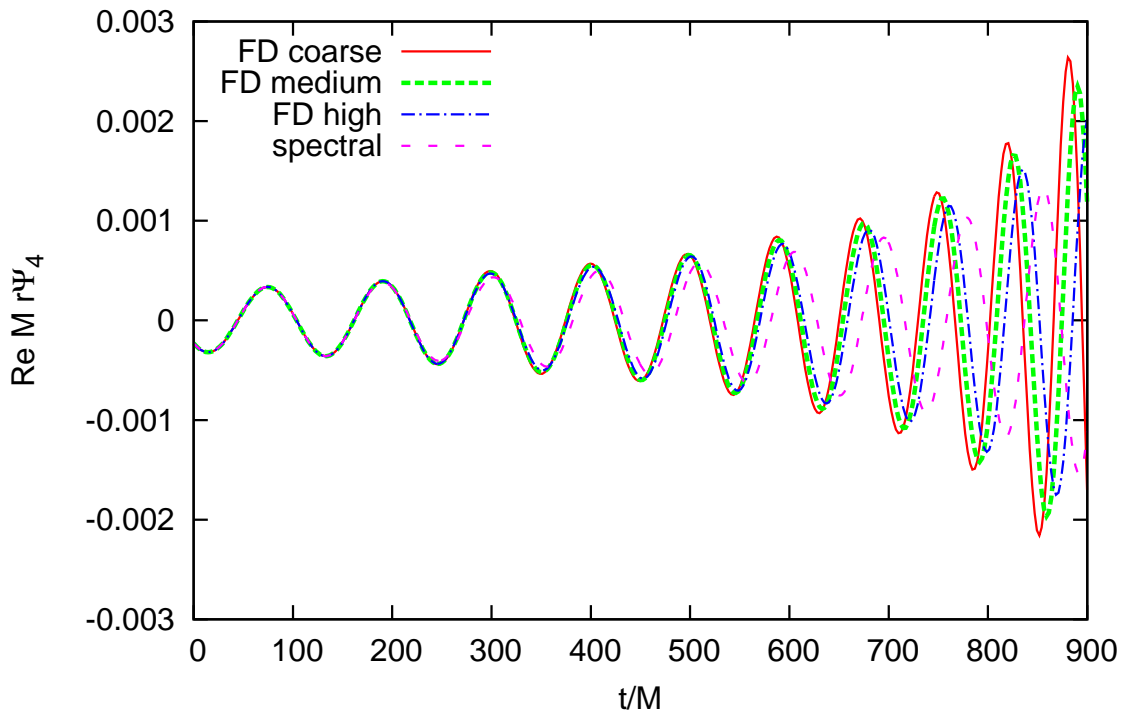
Figure 4.9: Real part of Ψ_4 for the finite difference and spectral results.

times and drift apart during the later stages of the evolution. A more meaningful

comparison is shown in Figs. 4.10 and 4.11, where we plot amplitude and phase of

the extracted wave. The differences between the finite differences waveforms and

the spectral one are shown in Figs. 4.12 and 4.13 for the amplitude and phase,

respectively.

4.6   Remarks

In our study we have shown that we can evolve orbiting black holes in a

stable way using a high-order multipatch approach and that this method scales well

with the number of processors. As a result, we expect to be able to achieve good
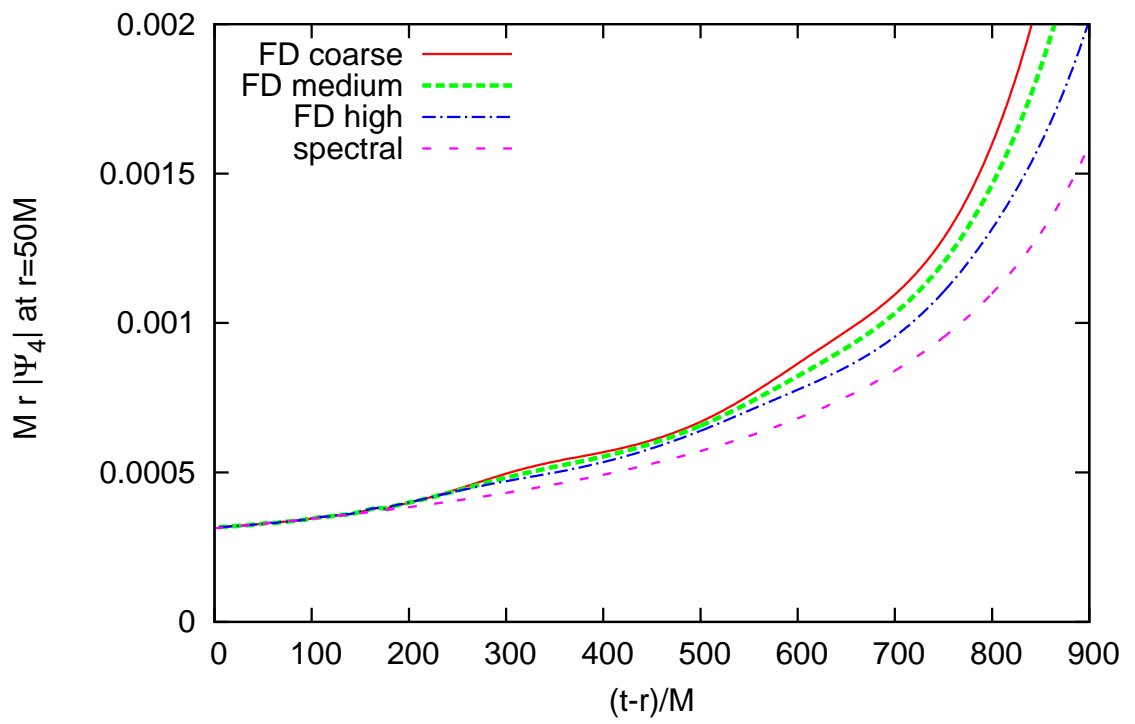
Figure 4.10: Ψ_4 amplitude for the finite difference and spectral results.
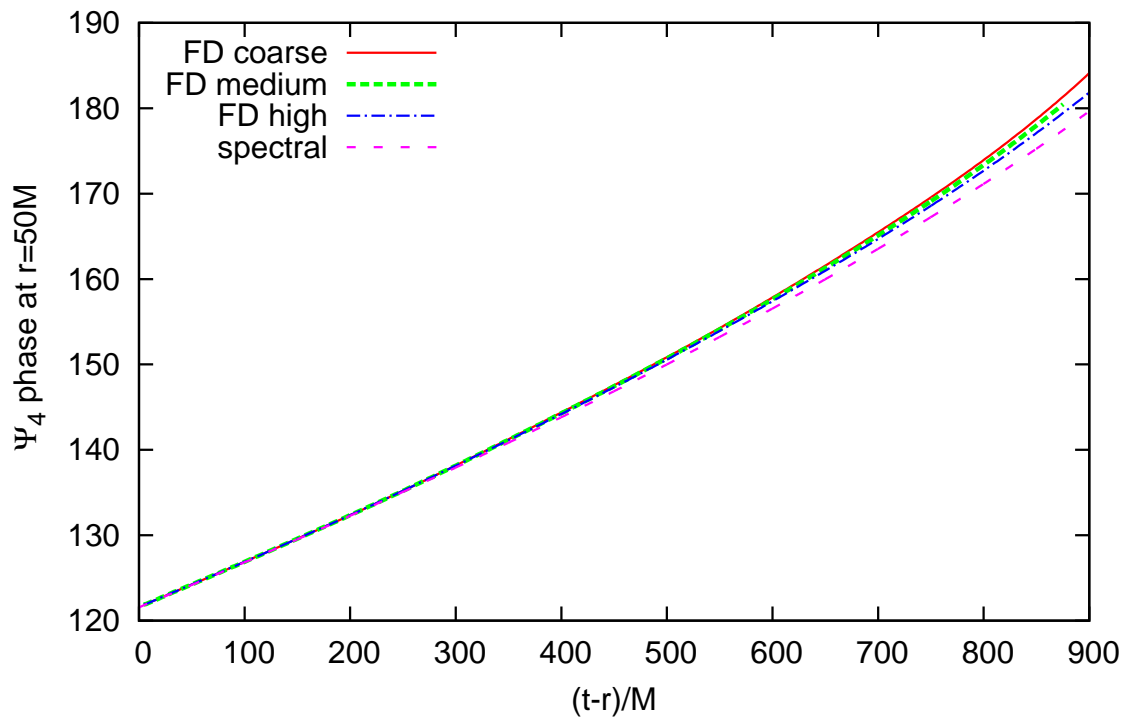
Figure 4.11: Ψ_4 phase for the finite difference and spectral results. Phases are in radians in all graphs.
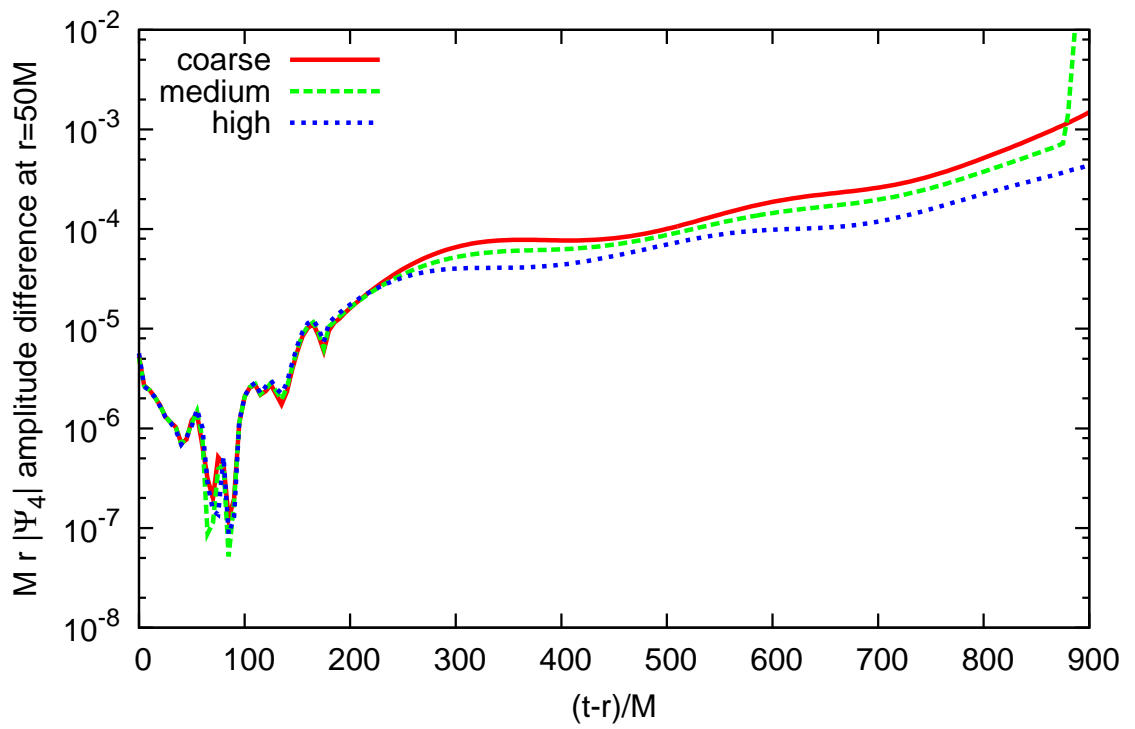
Figure 4.12: Differences in the Ψ_4 amplitude between the finite difference and the spectral results.
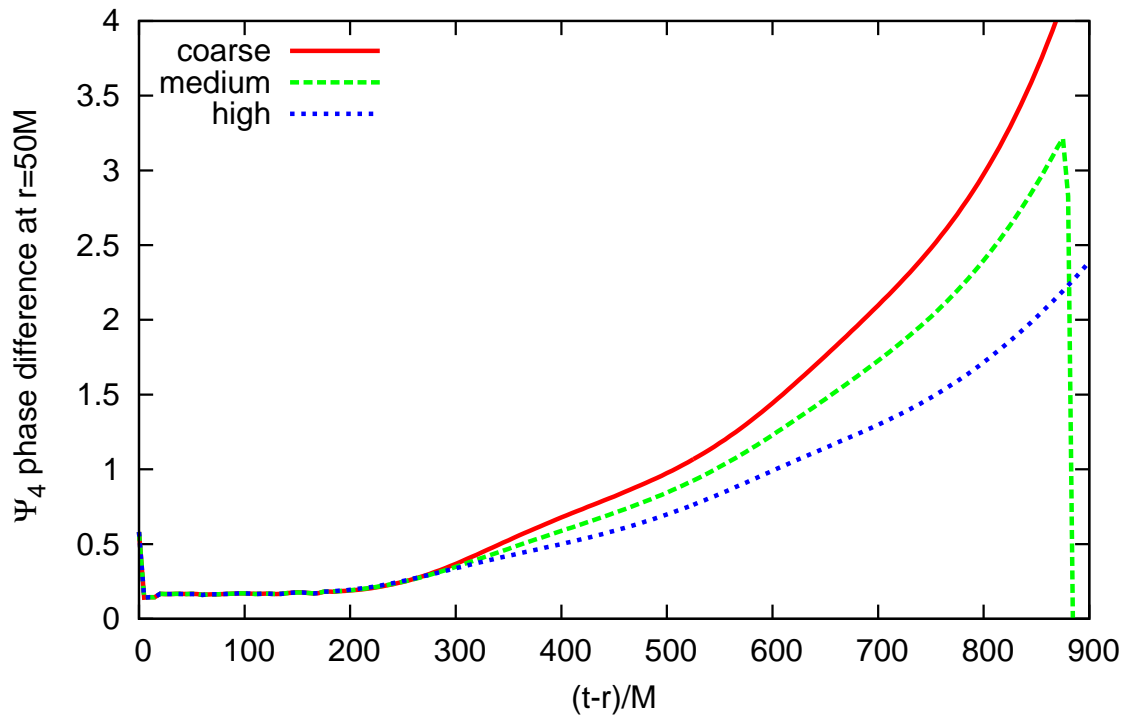
Figure 4.13: Differences in the Ψ_4 phase between the finite difference and the spectral results.

accuracy while still using only modest computational resources. These results also suggest that multipatch methods are an excellent alternative to AMR, with benefits of simplicity and $O(N)$ scaling for improving resolution in the wave zone. Finally, multipatch methods will allow one to use the same grid to evolve both metric and matter fields for a binary pair composed of a black hole and neutron star, allowing the advantages of high-order methods without the drawbacks of a hybrid spectral-finite difference approach.

Chapter 5

Comparing waveforms computed by different numerical relativity codes

5.1 Introduction and overview

At present time, most (if not all) numerical relativity groups can successfully numerically simulate the binary black hole problem, modeling all three phases of the collision, i.e. inspiral, merger and ringdown. The results presented in this chapter do not correspond to the current (as of this writing) state-of-the-art in numerical relativity, but to an earlier stage. The idea emerged by the end of 2007, when the Caltech-Cornell collaboration managed to perform a high-accuracy 15-orbit run which ended short before merger [30]. The problem carrying out the simulation past the merger of the two black holes was due to the rather simple coordinate conditions by then used, within the generalized harmonic formulation of the Einstein equations [113]. In the harmonic formulation of the equations the gauge conditions are specified by means of source functions. At that time, it was unknown how to to prescribe convenient gauge source functions that were useful when the spacetime becomes highly dynamical, i.e. close the the merger phase. On the other hand, the (by then, recently introduced) turducken[1] technique offered the possibility of evolving

---

[1]The word 'turducken' is the name of a Southern American dish consisting of a partially de-boned turkey stuffed with a de-boned duck, which itself is stuffed with a small de-boned chicken.

generic initial data, starting with the inspiral, going through merger and ringdown stages, using the coordinate conditions of the so-called moving punctures [54, 20] within the BSSN formulation [125, 158, 21] of the Einstein equations. The turducken proposal had been successfully tested and validated in several cases.

Thus, the idea was to pick a three-dimensional slice of the Caltech-Cornell simulation, in other words, a snapshot at a given time t and use the values of the 3-metric and extrinsic curvature as initial data for a turducken evolution, thus providing an effective method for completing and finishing the simulation. A multi-institution collaboration was launched, where every group would perform these final steps of the simulation with their own codes. By the time that different groups reported their waveforms, the Caltech-Cornell collaboration was able to find a proper gauge [153] for the generalized harmonic equations that was better suited for the merger phase. With this new gauge conditions, they were able to continue the simulation all the way through merger and ringdown. At the end, the situation was such that all participating research groups had managed to evolve the provided initial data, offering the opportunity to compare the extracted waveforms computed by different codes—starting from the same initial data.

In the following sections, we present the methods that we (Maryland-LSU group) employed to evolve the initial data provided. Other research groups that participated in the effort were AEI[2], Jena-FAU[3], Penn State and Princeton. We will

Here we are actually referering to the 'relativistic turducken', which means the method we use to stuff a black hole.

[2]Albert Einstein Institute

[3]Florida Atlantic University

focus in describing our simulations and present the final result of the comparison, namely the extracted waveforms.

5.2 Numerical techniques

5.2.1 Initial data

The initial data set is the key element for comparing waveforms in this study. We use a snapshot of an ongoing evolution of the Einstein equations. The data comes from the 15-orbit run of equal mass, non-spinning black holes performed by the Caltech-Cornell collaboration using the generalized harmonic formulation of Einstein equations and pseudo-spectral methods [30]. From this simulation, we take the value for the lapse, shift, 3-metric and extrinsic curvature at a time $t = 7600M$ (M being the sum of the irreducible masses of the black holes), thus making that instant the starting time $t = 0$ of our simulations.[4] That instant of time corresponds roughly to three orbits before merger.

The process of reading the initial data generated by a pseudo-spectral collocation method and initializing every point of the cartesian finite difference grid is handled via spectral interpolation. Since this procedure has a very small numerical error, it is not considered as a source of uncertainty in our simulations.

Another issue that needs to be overcome is the fact that the Caltech-Cornell

---

[4]Strictly speaking, we don't necessarily need the lapse and shift functions since they just characterize the gauge. However, they provide a good choice for initializing the lapse and shift in our code.

simulation uses a domain where the interior of the black holes is excised. This was

solved using the turducken approach [40, 39]. The idea here is to smoothly fill in

the interior of the black hole with something that is not necessarily a solution of

the Einstein equations. In practice, what we do is to solve an elliptic equation in

the excised region for each of the dynamical quantities aforementioned. The natural

boundary condition is the value of the field at the excision border. Solving an elliptic

equation is not a mandatory procedure. Filling in the interior of the black holes can

be done by any procedure that gives a smooth second spatial derivative across the

excision boundary.

The choice of lapse and shift is in principle an arbitrary one. Thus we set the

lapse profile at $t = 0$ according to

$$\alpha = \left[1 + \frac{1}{\sqrt{(x - x_1)^2 + (y - y_1)^2 + z^2}} + \frac{1}{\sqrt{(x - x_2)^2 + (y - y_2)^2 + z^2}} \right]^{-4} \quad (5.1)$$

where x_i and y_i are the initial coordinate positions of the black holes. The shift

vector is initialized to zero. We found in our numerical experiments that this choice

of lapse and shift reduced the (coordinate-dependent, of course) eccentricity in the

orbits.

5.2.2   Evolution system and gauge conditions

We evolve the initial data using the BSSN formulation of the Einstein equa-

tions [125, 158, 21] with the 1+log and gamma-driver conditions for the gauge [10].

The computational domain extends to a distance of $186M$, with M being the sum

of the irreducible masses of the individual black holes. Our runs make use of the

adaptive mesh refinement capability implemented in Cactus [46] via Carpet [58]. We use a total of 9 levels of refinement with ratio of 2 in resolution between adjacent levels. The grid spacing in the finest level is $0.0161M$ and $4.12M$ in the coarsest box. Derivatives are taken using a fourth order accurate operator, whereas time integration is done with a fourth order Runge-Kutta algorithm. To check convergence of our simulations we ran at higher resolutions, being the grid spacing a factor of 1.2 and 1.5 times smaller than the above mentioned resolution. All the results presented here correspond to the highest resolution available.

5.2.3 Wave Extraction

In our simulations we use the results of first order perturbation theory to compute the Moncrief function in the same way as in [105]. The plus and cross polarizations of the gravitational radiation can be written in terms of the Moncrief function Q as [124]

$$h_+ - ih_\times = \frac{1}{\sqrt{2}r} \sum_{\ell=2}^{\infty} \sum_{m=-\ell}^{\ell} \left(Q_{\ell m}^+ - i \int_{\infty}^{t} Q_{\ell m}^\times (t') dt' \right) {}_{-2}Y^{\ell m}. \tag{5.2}$$

Subsequently, the Newman-Penrose scalar Ψ_4 is computed by taking two time derivatives of the plus and cross components of the gravitational wave amplitude [167]

$$\Psi_4 = \partial_t^2 h_+ - i\partial_t^2 h_\times. \tag{5.3}$$

We compared the waveforms obtained via the Moncrief functions with another extraction method that uses gauge-invariant perturbation theory [132]. This method is the one described in detail in Chapter 3. Both methods are essentially the same

in their approach. The difference being that the later identifies the background geometry in dynamical way. When this is done the background metric components and the mass have a small temporal dependence. The differences between both extraction methods become noticeable the closer the extraction spheres are to the black hole. However, both methods render the same result as the extraction radius becomes larger.

5.2.4 Wave Extrapolation

Since waveforms are extracted at finite distance from the source, it is expected that those waveforms do not fully describe what an observer would see at future null infinity. At finite distances, there is always a systematic error in the extraction procedure that involves the identification of a background geometry to compute the gravitational radiation (perturbative method) or the construction of a null tetrad (Newman-Penrose method). Such effects fall-off as $1/r$, as we extrapolate the waveform to infinity, the leading order should not contain any dependence on r.

The extrapolation to infinity is done using the method described in [30]. The waveforms are aligned using the retarded coordinate $u = t - r^*$ where r^* is the tortoise coordinate. We fit the amplitude A and phase ϕ of the waveform to a polynomial in powers of $1/r$,

$$\phi(u,t) = \phi_{(0)}(u) + \sum_{k=1}^{3} \frac{\phi_{(k)}(u)}{r^k}, \tag{5.4}$$

$$rA(u,t) = A_{(0)}(u) + \sum_{k=1}^{3} \frac{A_{(k)}(u)}{r^k}. \tag{5.5}$$

We keep terms up to $1/r^3$ since higher powers tend to amplify the noise.

5.3 Comparing Waveforms

The dominant mode $\ell = m = 2$ of the waveforms was compared in two ways, at finite extraction radius and extrapolated to infinity. At finite distance we have the advantage that we are comparing the exact same quantity and the differences in the shape of the wave are due to numerical error, extraction procedures and gauge dependence. In Fig. 5.1 we plot the real part of Ψ_4 for the waveforms computed by the Caltech-Cornell spectral code and our finite differences one. They are extracted at coordinate radius $r = 100$. The agreement is pretty good. Figures 5.2 and 5.3 show the amplitude and phase for Ψ_4. We compute the difference between the two waveforms for both, amplitude and phase. The result is shown in Figs. 5.4 and 5.5. We point out that other contribution to the discrepancy comes from the method we use to compute Ψ_4, which consisted in taking two numerical time derivatives from the Moncrief function data. That process introduces errors in the final waveform since derivatives taken using finite differences tend to amplify numerical noise in the data.

For the comparison of waveforms at infinity we performed the fitting procedure outlined in Sec. 5.2.4. As a first step, we located the position of the maximum in the amplitude of the waveforms. They are then shifted in time such that the maximum corresponds to $t = 0$ for both of them (see Fig. 5.6). In the next step, using data in the coordinate time interval $[-20, 20]$, we minimize the square of the difference in amplitude by shifting one of the waveforms in time. The result is shown in Fig. 5.7, where it's clear that the agreement is better. After this, we recompute the difference
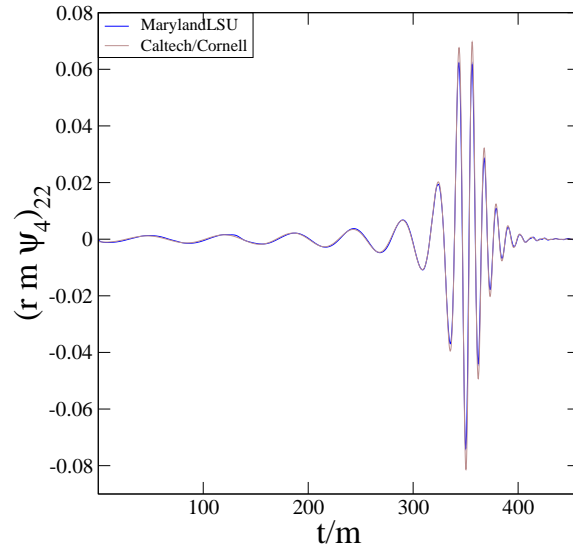
Figure 5.1: Real part of Ψ_4 waveform extracted at a coordinate radius $r = 100$.
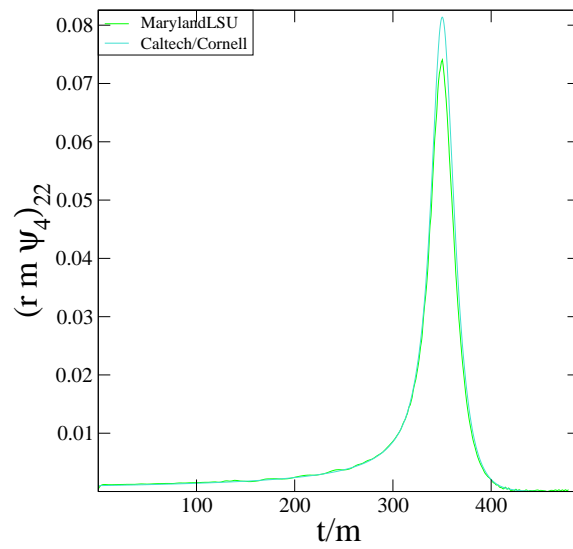
Figure 5.2: Amplitude $|\Psi_4|$ of the waveform extracted at a coordinate radius $r = 100$.
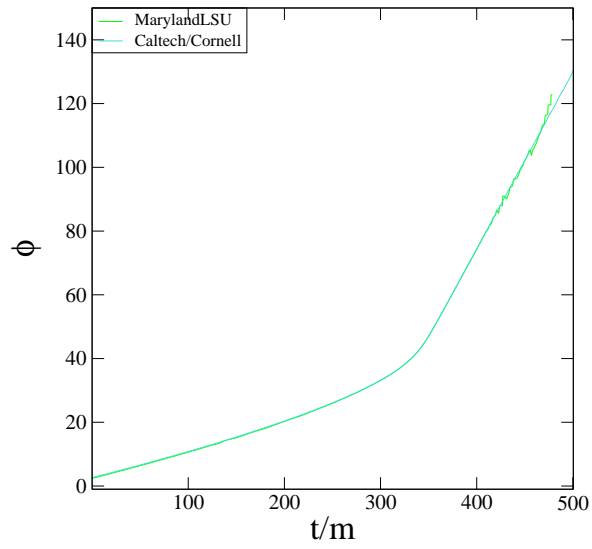
Figure 5.3: Phase of Ψ_4 waveform extracted at a coordinate radius $r = 100$.
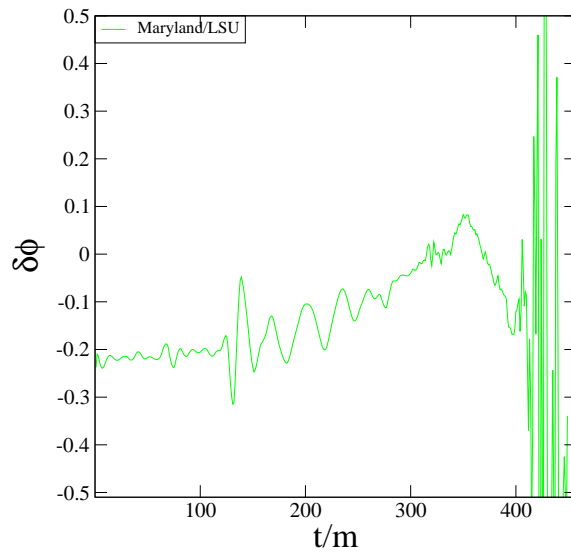
Figure 5.4: Phase difference between the Caltech-Cornell waveform and the Maryland-LSU one, at coordinate radius $r = 100$.
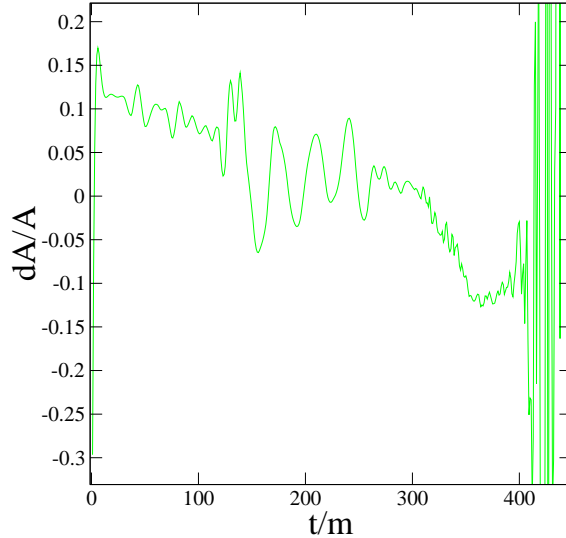
Figure 5.5: Relative amplitude difference between the Caltech-Cornell waveform and the Maryland-LSU one, at coordinate radius $r = 100$.

in the amplitude and plot it in Fig. 5.8.

As for the phase, using the shifted data by minimizing the difference in the amplitude, we do an additional phase shifting to minimize the phase difference between the waveforms over the coordinate time interval $[-40, 40]$. The phase difference between waveforms is shown in Fig. 5.11.

The difference in the amplitude between the waveforms is less than 0.005. The difference in phase is less than 0.1 rad (inspiral) and 0.2 for the merger and ringdown phase.

5.4 Conclusion

Acceptable agreement has been found in the waveforms compared in this study. The agreement is improved when the waveforms are extrapolated to infinity. Given that the initial data is exactly the same, the two main sources of error are the

135
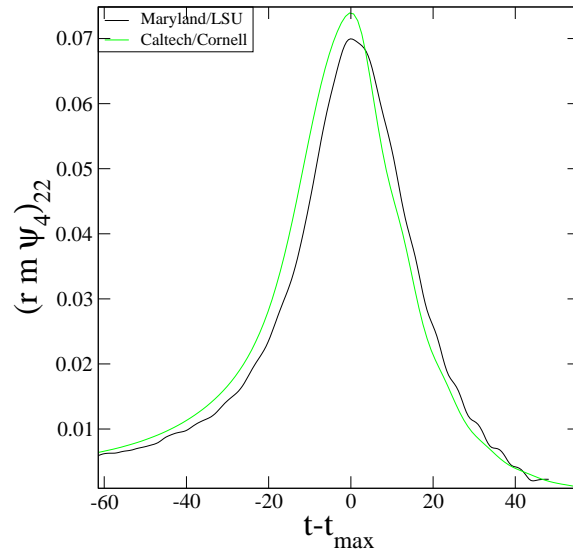
Figure 5.6: Amplitude of waveforms extrapolated at infinity shifted to align them at maximum peak.
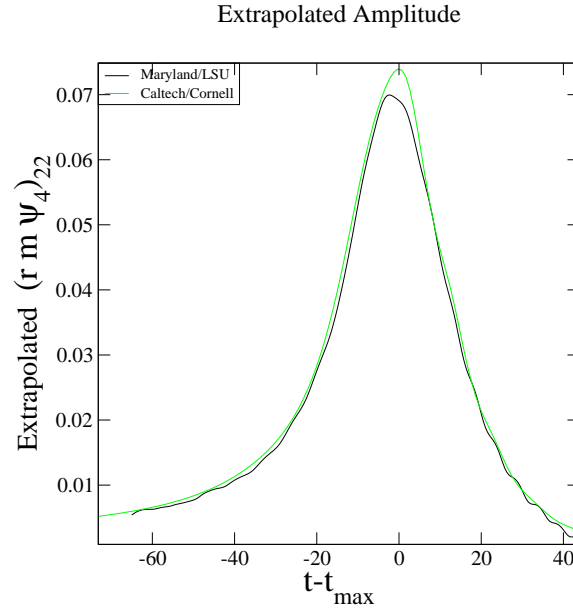
Figure 5.7: Amplitude of waveforms extrapolated at infinity shifted to minimize the difference in the amplitude over the interval $[-20, 20]$.
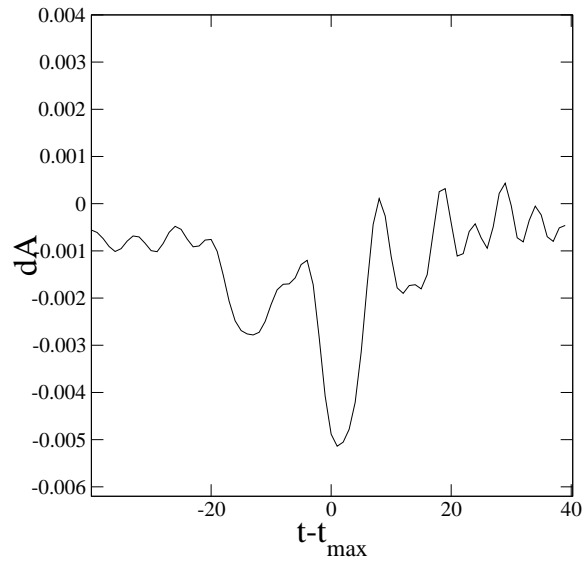
Figure 5.8: Amplitude difference of waveforms extrapolated at infinity.
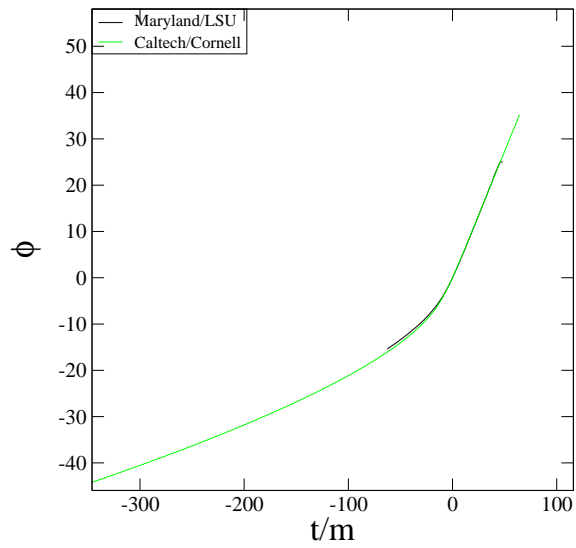
Figure 5.9: Phase of waveform extrapolated at infinity, shifted to align them at maximum peak with zero phase difference.

137
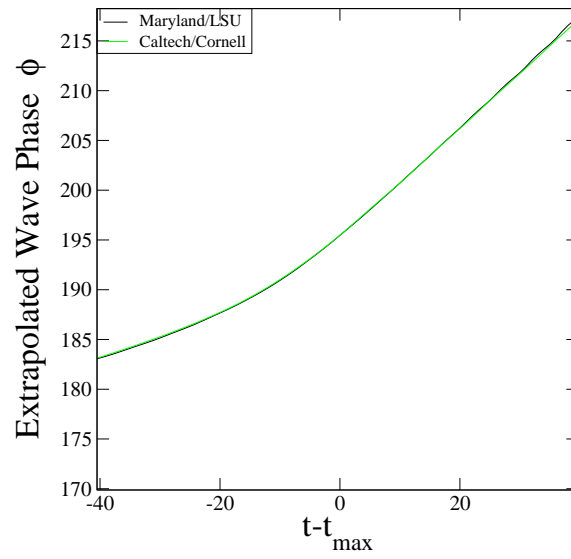
Figure 5.10: Phase of waveforms extrapolated at infinity, shifted to minimize the difference in the phase over the interval $[-40, 40]$.
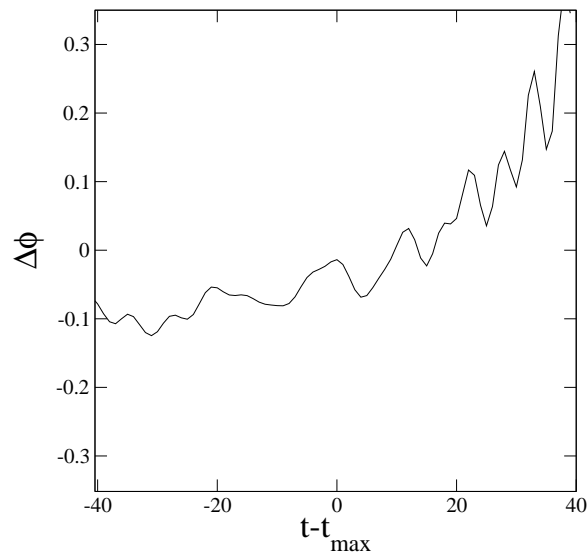
Figure 5.11: Phase difference between the Caltech-Cornell and Maryland-LSU waveform extrapolated at infinity.

accumulation of truncation error during the evolution and the systematic error emanating from the procedure to extract gravitational waveforms. The results of finite differences codes are much similar among themselves than the waveform from the Caltech-Cornell group, where the evolution of the Einstein equations is done using pseudo-spectral methods. This statement is based in comparisons with other research groups whose data will we presented elsewhere.

Chapter 6

Mode-coupling generation of gravitational radiation in the ringdown
of Schwarzschild black holes

6.1 Outlook and Motivation

The black hole no-hair theorem [93, 23] states that the end point of any system
with enough gravitational energy to form a black hole is remarkably simple: it is
uniquely characterized by one member of the Kerr family [96], which is described by
only two parameters: the spin and mass of the final black hole. As a consequence, the
details by which different systems decay to such endpoints have been of interest for
many decades. Pioneering studies were done by Price [140] in the early seventies,
who studied linearized perturbations of non-rotating (Schwarzschild) black holes.
Price established that except for pathological solutions [146] there is always an
intermediate stage where the ring-down is dominated by a set of oscillating and
exponentially decaying solutions, the so-called quasi-normal modes (QNM), followed
by a power-law 'tail' decay due to backscattering.

In the case of gravitational perturbations of non-rotating black holes the rel-
evant equations from which QNM can be inferred are the Regge-Wheeler [142] and
Zerilli [177, 178] ones. For rotating black holes the analogue (though based on a
curvature formalism, as opposed to a metric one) is the Teukolsky equation [167],

whose QNM structure was first studied by Teukolsky and Press [137]. Comprehensive reviews on the topic are presented in [26, 102].

The least damped QNM frequency correspond to the fundamental mode. Subsequent modes (overtones) decay much faster. Because of this, they are very difficult to detect, even for high accuracy waveforms (numerically or measured). Hence, in practice, after some transition time at the linearized level the ringdown of Kerr black holes is described by a few oscillating modes which decay exponentially in time, until they reach the tail regime and the signal becomes sufficiently small. During the tail phase, the signal decays in a specific power-law dictated by the effective backscattering problem. It is interesting to note that the tail decay problem for Kerr black holes is still not completely clear and, in fact, certain aspects of the problem have been under dispute over many years until recently [170, 78].

From an observational point of view this universal ringdown is of great power: one can use a single QNM detection to infer the mass and spin of the black hole source, *assuming* General Relativity (GR) to be correct. Alternatively, through a two-mode detection one can test GR and/or the assumption that a black hole is the source of the measured signal [66]. The main idea is that the QNM frequencies of both detections have to be consistent with respect to their inferred masses and spins.

The LISA mission is expected to measure gravitational waves in the low frequency spectrum: $(10^{-5} - 10^{-1})$Hz, the main expected sources being the collisions of supermassive binary black holes (SMBBH) [27]. Flanagan and Hughes [69] showed that quite generically, the signal to noise ratio for this problem in the inspiral regime

141

should be comparable to that one of the ringdown, i.e. once the two black holes have collided into a single one which is decaying to a stationary Kerr state through QNM. Therefore, detection of SMBBH by LISA via the measurement of QNM seems to be feasible. Assuming a lower cutoff of $(10^{-4} - 10^{-5})$Hz and requiring that the QNM signal lives long enough to travel once through LISA's propagation arms places a constraint on the mass range of the SMBBH candidates: from a few $10^5 M_\odot$ to $(10^8 - 10^9)M_\odot$.

A step beyond detection analysis is that one of parameter estimation. In Ref. [24, 27] it was found that by means of a single QNM detection, LISA would be able to accurately infer the mass *and* spin of supermassive black holes: for black holes with mass $M \gtrsim 10^5 M_\odot$ the errors in mass and spin would be smaller than one part in 10^2, and smaller than one part in 10^5 for the more optimistic case $M \gtrsim 5 \times 10^5 M_\odot$ [1] These accuracies depend on the ringdown efficiency ϵ_{rd}, defined as the fraction of mass radiated in ringdown waves. In these references very conservative values were used: $\epsilon_{rd} \approx 0.1\% - 3\%$. For example, it has been found in numerical simulations of two equal mass, non-spinning black holes starting from quasi-circular motion that around $\epsilon_{red} \approx 2\% - 3\%$ of the total mass is radiated in the ringdown regime [44]. The inclusion of different masses and/or spin increases this value.

In [24, 27] it was also found that at least a second detection of *either* mass *or* spin should be possible for LISA. Resolving *both* spin and angular momentum (or , equivalently, both frequency and damping times associated with the QNM

---

[1]Only cases with $M \gtrsim 10^5 M_\odot$ are considered in [27, 24, 27] because otherwise the QNM signal is short lived enough that special detection techniques might be needed.

oscillation of this second mode) might require a very large critical SNR, which might in turn need the second mode to radiate a significant portion of the emitted gravitational wave when compared to the first one. Whether this is feasible or not can only be established by giving precise predictions of the amplitudes for second-mode candidates.

The dominant mode from a binary black hole collision is expected to be the one with angular multipole indices $\ell = m = 2$, which has so far always been modeled or expected to behave as the fundamental QNM in linearized theory. With respect to candidates for a second detectable mode, it is usually thought of either a higher multipole, fundamental QNM or a higher $\ell = m = 2$ overtone. Still, all these possibilities are usually considered and modeled within linearized perturbation theory, and expected to behave accordingly. The rationale behind this reasoning is that non-linear modes are usually thought to be too small.

In the mid to late nineties there was a burst of interest in second-order perturbations of Schwarzschild black holes from a different angle (see Ref. [77] and references therein). By that time, the main motivation was to study black hole collisions in the so-called closed limit approximation and compare perturbative analysis with supercomputer simulations. In those days, supercomputer simulations of binary black holes were starting close enough that the results could be reproduced by perturbation theory. Motivated by the close limit success, work on second-order perturbations of Kerr black holes was started around the same time [55], though for technical reasons the resulting formalism did not reach a stage where explicit calculations could be carried out. Similarly, for the sake of definiteness and limitations in

143

computer algebra schemes, second-order Schwarzschild perturbations were worked out only for a few particular multipole cases.

In the present work we re-examine the issue of second-order perturbations of Schwarzschild black holes but with a different focus in mind. First, our approach allows us to study *generic* first and second-order perturbations [36], mostly due to the development of a suitable theoretical framework [34] and to the advance of very efficient symbolic algebra tools for tensor-type calculations [119, 35]. Second, our goal is not to benchmark numerical relativity codes, which are quite mature by now. Instead, we want to explore *generic* properties of self-generated second-order modes due to mode-mode coupling. The natural questions that arise are: how much energy do they radiate?, which are the dominant modes?, at what (complex) frequencies they resonate?, how all these aspects depend on the characteristics of the initial perturbation?, what is the dynamics of the wave propagation and how can they be used for detection of two-mode signals?, to mention a few.

The structure of this presentation is as follows: Section 6.2 reviews the basics of our first and second-order formalism for *generic* perturbations. Section 6.3 describes our pseudo-spectral collocation (PSC) approach for solving the first and second-order Zerilli functions. The latter is powered by a quadratic source which depends on the first-order Zerilli function and higher-order derivatives. Section 6.4 presents our results.

6.2   First and second-order gauge invariant perturbations of Schwarzschild

We very briefly summarize those results of the formalism for *arbitrary* second-order gauge-invariant perturbations presented in [36] which are relevant for the current work; see that reference for more details.

The gravitational radiation is composed by two different polarities, which can be completely described in terms of two master functions. In a Schwarzschild background, the so-called Regge-Wheeler function contains all the relevant information of the axial sector, whereas the Zerilli function encodes the polar degree of freedom. Therefore, at first-order the relevant equations to solve are

$$\Box\, {}^{\{1\}}\Psi_\ell^m - V\, {}^{\{1\}}\Psi_\ell^m = 0 \tag{6.1}$$

where ${}^{\{1\}}\Psi_\ell^m$ denotes either the first-order Regge-Wheeler or Zerilli master functions for a given (ℓ, m) mode, and the Zerilli and Regge-Wheeler potentials are, respectively

$$V_{\mathrm{Z}} = \frac{\ell(\ell+1)}{r^2} - \frac{6M}{r^3}\frac{r^2\lambda(\lambda+2) + 3M(r-M)}{(r\lambda + 3M)^2}, \tag{6.2}$$

$$V_{\mathrm{RW}} = \frac{\ell(\ell+1)}{r^2} - \frac{6M}{r^3}. \tag{6.3}$$

In the above expressions $\lambda \equiv \frac{1}{2}(\ell-1)(\ell+2)$, M is the mass of the Schwarzschild black hole, and the box is the two-dimensional D'Alambertian operator corresponding to the Schwarzschild background. It can be expressed in any coordinates, but usually these are taken to be the tortoise ones. It turns out however, to be much easier from an implementation point of view to excise the black hole from the computational domain by using, for example, Kerr-Schild coordinates. We do so in this study (both

145

at first and second-order).

The Regge-Wheeler-Zerilli (RWZ) equations (6.1) are second-order in time and space hyperbolic equations for each master function. As such, in order to produce a non-trivial and unique solution the value of the master functions and their time derivatives have to be initialized at $t = 0$. One comment is in place here: whatever initial values are given to these functions and time derivatives, the linearized Hamiltonian and momentum constraints are *automatically* satisfied. The same holds in the second-order case. This is a non-trivial property which is not immediately apparent but turns out to be a consequence of the formalism, one ends up by construction explicitly satisfying those constraints. This property was used, for example, in Ref. [132] to construct initial data which satisfies the linearized constraints for three-dimensional numerical evolutions without having to numerically solve the standard elliptic equations of the initial value problem in the $3 + 1$ decomposition of spacetime [121].

Any solution of Eqs. (6.3) generates second-order contributions which can be described by Regge-Wheeler and Zerilli-type equations with source terms

$$\Box \, {}^{\{2\}}\Psi_\ell^m - V \, {}^{\{2\}}\Psi_\ell^m = {}^{\{2\}}\mathcal{S}_\Psi \, , \tag{6.4}$$

The sources ${}^{\{2\}}\mathcal{S}_\Psi$ are rather complicated and lengthy expressions which depend quadratically on the lower order perturbations and their time and space derivatives from both first-order sectors. That is, the coupling of even (odd) parity modes in general generates odd (even) parity second-order modes.

For computational efficiency (based on the numerical scheme that we use to

solve the first and second-order RWZ equations), whenever higher than first-order time derivatives appear in the source of Eq. (6.4) we use Eq. (6.1) to 'trade' time derivatives by spatial ones.

The radiated energy can then be computed in terms of first $^{\{1\}}\Psi_\ell^m$ and second-order $^{\{2\}}\Psi_\ell^m$ modes. Reference [36] deals with the most general case for these sources and computation of the radiated energy. Here we want to quantitatively explore the predictions of the formalism for the cases of most physical interest, study first-order mode interactions and the resulting ones generated at second-order. This is the case described by a first-order, even-parity $\ell = m = 2$ mode.

The self-coupling between these modes generates second-order $(\ell = 4, m = \pm 4)$ even-parity ones, whereas the coupling between them gives rise to the second-order $(\ell = 4, m = 0)$, $(\ell = 2, m = 0)$ and $(\ell = 0, m = 0)$ even-parity modes as well as to the $(\ell = 3, m = 0)$ and $(\ell = 1, m = 0)$ odd-parity ones. Since we deal only with different radiative aspects of this system, we can ignore modes with $\ell < 2$.

We could introduce non-vanishing second-order modes with any harmonic label (ℓ, m) via initial second-order perturbations. However, we are interested in the particular solution of Eq. (6.4), since the homogeneous one will be exactly the same as the first-order one. Therefore, here we will always assume vanishing initial data for all the second-order modes and concentrate on those modes generated by first order mode coupling.

In this particular case, the full radiated power associated with the mentioned

modes for a given observer located at r_{obs} as a function of time is simply given by

$$
\begin{aligned}
\text{Power}(r_{obs}, t) \quad = \quad & \frac{dE}{dt} = \frac{\epsilon^2}{12\pi} \left| \partial_t \, {}^{\{1\}}\Psi_2^2 \right|^2 + \frac{9\epsilon^4}{640\pi} \left\{ \left| \partial_t \, {}^{\{2\}}\Psi_4^0 \right|^2 + 2 \left| \partial_t \, {}^{\{2\}}\Psi_4^4 \right|^2 \right\} \\
& + \frac{\epsilon^4}{96\pi} \left| \partial_t \, {}^{\{2\}}\Psi_2^0 \right|^2 + \mathcal{O}\left(\epsilon^5\right) \;,
\end{aligned}
\tag{6.5}
$$

where all the expressions on the right hand side are evaluated, at (r_{obs}, t). In principle this equation is valid only at null infinity but, as it is usually the case, we evaluate it at a finite but sufficiently large radius.

6.3   Numerics

We now describe in some detail our numerical approach for solving the first and second-order RWZ equations, since in the past, difficulties have been reported with the high order derivatives in the sources of the second-order version of these equations. In our approach, we find no such difficulties and therefore it is important to emphasize the high numerical accuracy of our results.

We numerically solve the first and second-order RWZ equations using a pseudo-spectral collocation (PSC) method. The spatial derivatives are computed using Chebyshev polynomials and Gauss-Lobatto (GL) collocation points; the system is evolved in time using a standard fourth order Runge-Kutta scheme. We use a small enough time-step for the time integration so that the solution converges exponentially with the number of collocation points (see below). High accuracy in this problem is important because the second-order modes could be small enough so that they could be confused or masked with numerical errors. The accuracy of all the simulations presented here are at the level of double precision round-off, and as

148

we will see this is well below what we need to assert our conclusions with confidence.

GL collocation points are not equally spaced; rather they cluster near the edges of the computational domain (equally spaced points would not give exponential convergence). For that reason it is standard to use a multi-domain approach. Here we subdivide our radial domain in (non-overlapping) blocks of length $10M$ each, communicated through a penalty technique. At each interface each incoming characteristic mode u^+ is penalized according to (see [92] and references therein)

$$\dot{u^+} = (\ldots) - \frac{\alpha N^2 \delta}{r_{block}}(u^+ - v^+), \tag{6.6}$$

where v^+ is the value of the same mode at the interface point using the neighboring block, r_{block} is the size of the corresponding block ($10M$ in these simulations), α is the associated characteristic speed, N the number of collocation points on that block and δ a penalty parameter chosen here to be $\delta = 0.6$. At the outer boundary each characteristic incoming mode is similarly penalized to zero; though this is done simply to achieve stability, in our simulations the domain is large enough that our results are causally disconnected from the outer boundary. The singularity of the black hole is dealt with through excision (i.e. by placing an inner boundary inside the event horizon).

Figure 6.1 shows a self convergence test for the first-order Zerilli function, extracted at $r = 51M$, both changing the number of collocation points as well as the timestep. The initial data used below for such test was

$$^{\{1\}}\Psi = 0 \quad , \quad ^{\{1\}}\dot{\Psi}(t = 0, r) = e^{-(r - r_0)^2/\sigma^2}, \tag{6.7}$$

with $\sigma = 4M$, $r_0 = 20M$ and a spatial domain $[1.8M, 301.8M]$. From those plots, we

see that using 30 collocation points per domain and a timestep $\Delta t = 0.001M$ gives a numerical error at the level of double precision round-off. Hence, unless otherwise stated, we use such resolutions for all of our simulations.

For definiteness we show the result of a sample convergence test in Fig. 6.2 for the second order $\ell = m = 4$ mode, where the source is the one corresponding to Fig. 6.1.

In order to compare the magnitude of the errors with the solutions themselves, in Fig. 6.3 we show the absolute values of the first-order ${}^{\{1\}}\Psi_2^2$ and second-order ${}^{\{2\}}\Psi_2^0$, ${}^{\{2\}}\Psi_4^0$ and ${}^{\{2\}}\Psi_4^4$ Zerilli solutions from the previous plots at their highest resolutions; all extracted at $r = 51M$. The purpose of this figure is to qualitatively discuss their behavior. Recall however that no physical conclusion can be inferred without further analysis from the second-order Zerilli functions, since they are non-unique. What is really important is the radiated energy in terms of them [cf. Eq. (6.5)]. We will turn to this in the next Section. Another feature to mention is that for most of the ringdown, the order of magnitude of the second-order Zerilli functions appear to be comparable to (and in one case even larger than) the first-order one. There is no contradiction in this, since their contribution to the energy is scaled by ϵ^4 (ϵ being the perturbative parameter, see Eq. (6.5), while the contribution of the first-order Zerilli function is scaled by ϵ^2). However, this behavior will be important when discussing their ringing frequencies.
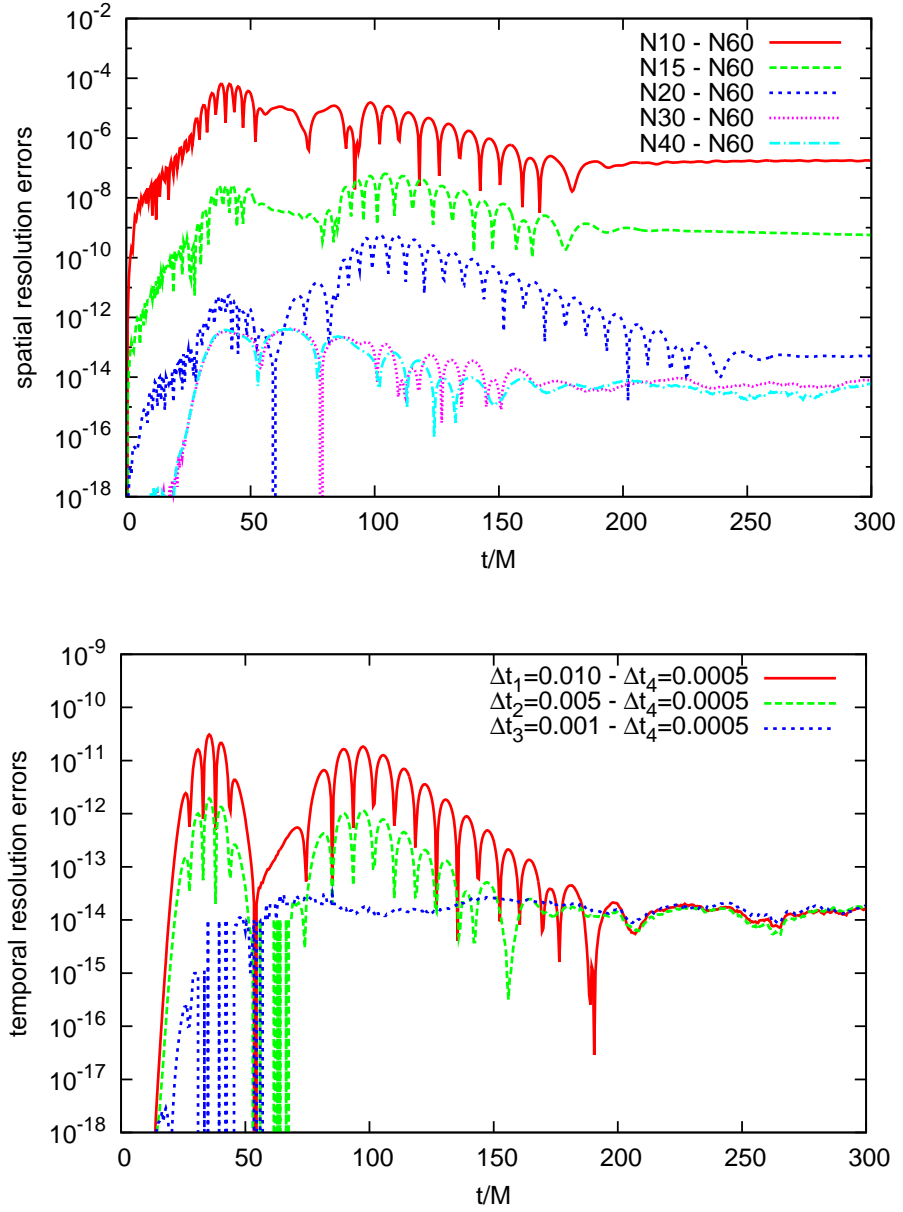
Figure 6.1: Absolute numerical errors for different spatial resolutions using a fixed timestep $\Delta t = 0.01M$ (top), and for different timesteps using a fixed spatial resolution of $N = 60$ points per domain (bottom). Both figures show the differences between several resolutions and the most accurate one, which is $N = 60$ for the top panel and $\Delta t_4 = 0.0005M$ for the bottom one. In both cases the observer is located at $r = 51M$. We see exponential convergence and errors in the order of double precision round-off.
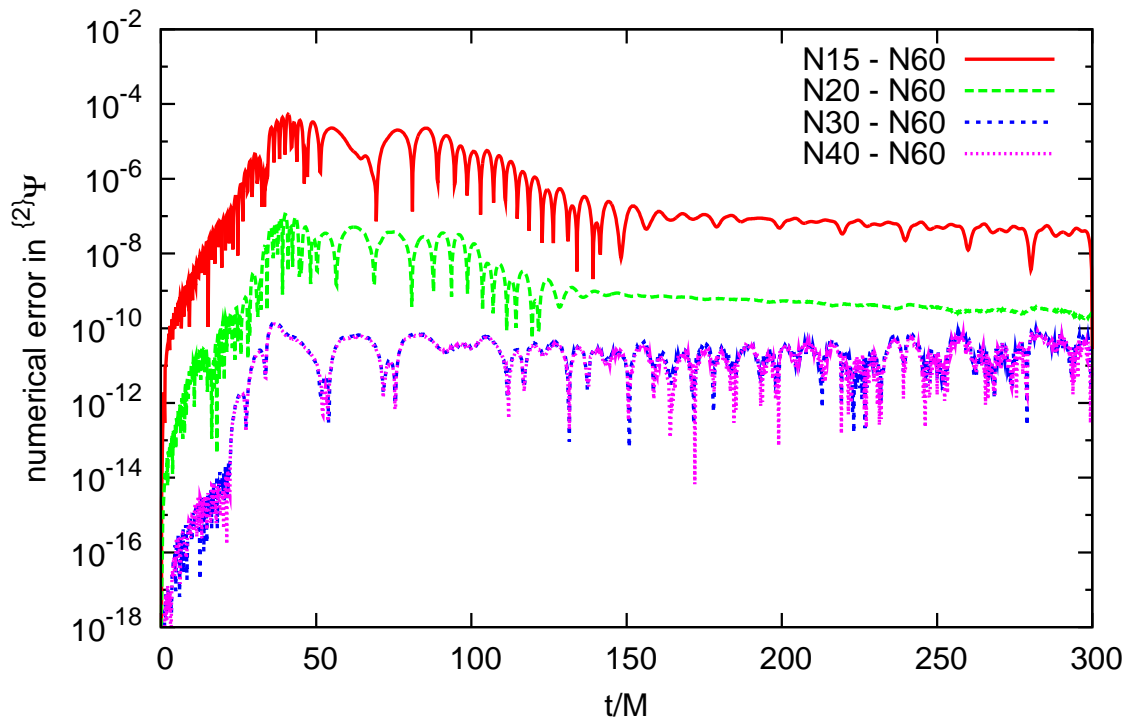
Figure 6.2: Absolute numerical errors in the second-order Zerilli function ${}^{\{2\}}\Psi_4^4$ for different spatial resolutions and a fixed timestep $\Delta t = 0.001M$. The errors are to be interpreted as in the previous figures. The observer position is $r = 51M$.
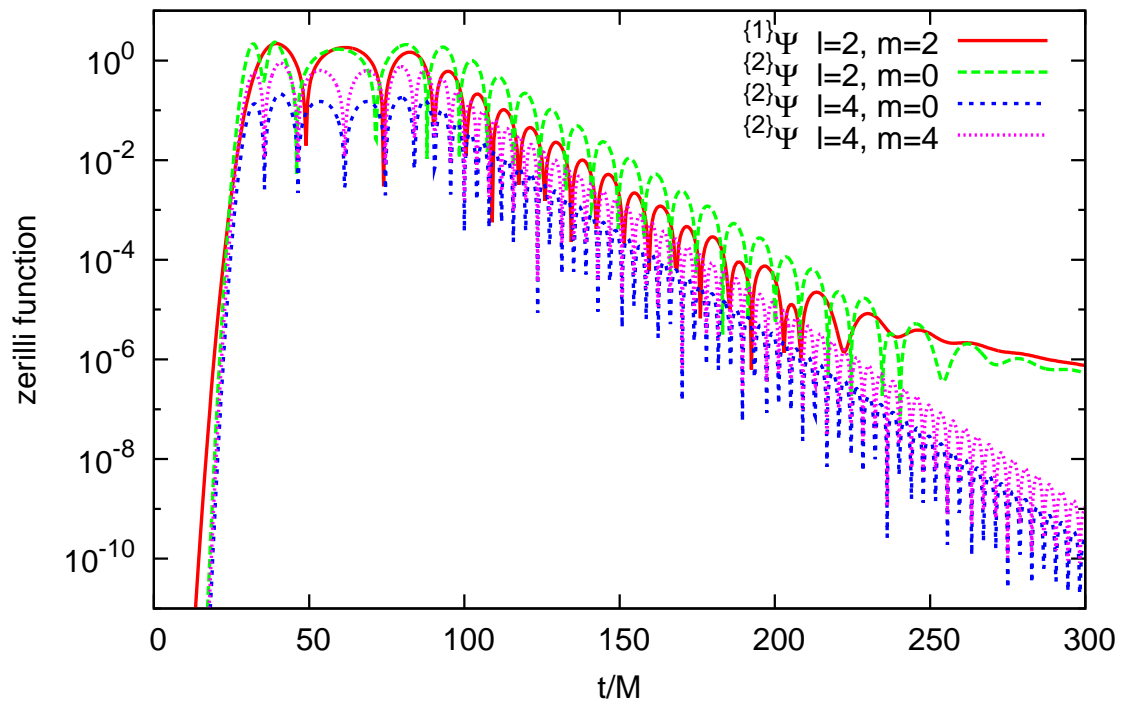
Figure 6.3: Absolute value of all (first and second-order) Zerilli functions extracted at $r = 51M$.

6.4 Results and discussion

6.4.1 Setup of numerical simulations

In numerical simulations of binary black hole evolutions, it is found that around 2% of the ADM mass is radiated after a common apparent horizon is found; i.e. in the ringdown [44]. This is also consistent with the close-limit prediction of grazing black holes for a final black hole with spin $a \sim 0.7$ [97]. In our perturbative treatment, the radiated energy scales with ϵ [quadratically in the leading contribution, and to the fourth power in the next correction, see Eq. (6.5)].

We solve the first-order Zerilli equation with four different types of initial data:

1. Time Derivative (TD)

$$
\begin{aligned}
{}^{\{1\}}\Psi_2^2(t=0,r) &= 0, \\
{}^{\{1\}}\dot{\Psi}_2^2(t=0,r) &= e^{-(r-r_0)^2/\sigma^2}
\end{aligned}
$$

2. Time Symmetric (TS)

$$
\begin{aligned}
{}^{\{1\}}\Psi_2^2(t=0,r) &= Me^{-(r-r_0)^2/\sigma^2} \\
{}^{\{1\}}\dot{\Psi}_2^2(t=0,r) &= 0
\end{aligned}
$$

3. Approximately Outgoing (OUT)

$$
\begin{aligned}
{}^{\{1\}}\Psi_2^2(t=0,r) &= Me^{-(r-r_0)^2/\sigma^2} \\
{}^{\{1\}}\dot{\Psi}_2^2(t=0,r) &= -(1-2M/r)\partial_r \, {}^{\{1\}}\Psi_2^2(t=0,r)
\end{aligned}
$$

154

4. Approximately Ingoing (IN)

$$^{\{1\}}\Psi_2^2(t=0,r) \;\;=\;\; Me^{-(r-r_0)^2/\sigma^2}$$

$$^{\{1\}}\dot{\Psi}_2^2(t=0,r) \;\;=\;\; (1-2M/r)\partial_r \,^{\{1\}}\Psi_2^2(t=0,r)$$

At second-order we give zero initial data, i.e. we solve the equations for the pure coupling of the first-order modes. For each simulation we then calculate the contribution to the radiated energy $^{\{n\}}E_\ell^m$ due to each mode as

$$^{\{n\}}E_\ell^m(t) = \epsilon^{2n} \,^{\{n\}}k_\ell^m \int_0^t \left| \partial_{\tilde{t}} \,^{\{n\}}\Psi_\ell^m(r_{obs},\tilde{t}) \right|^2 d\tilde{t}, \tag{6.8}$$

where $^{\{n\}}k_\ell^m$ are the constants that appear in Eq. (6.5).

6.4.2 Oscillation and damping frequencies

Ioka and Nakano have put forward the idea that high-order modes should oscillate with twice the (complex) quasi-normal frequency of first-order modes [95, 126]. This seems reasonable, since the source for the second-order Zerilli equation is quadratic in the first-order modes, so one could imagine that frequencies get doubled in Fourier space. The physical picture, however, is at the same time more subtle and simpler.

Recall that the physical process we are studying here is the coupling of linear modes. At the level of setting initial data, that means that we initialize the second-order Zerilli functions to zero for all the modes. The second-order Zerilli functions have sources which are quadratic in the first-order solution. What happens in practice is that those sources quickly excite the second-order solutions to a non-vanishing

value and later decay very fast in time. As a consequence, once the second-order functions have been excited, they essentially propagate with a vanishing source. In other words, they propagate as their linearized cousins would do. In particular, they oscillate with the same, standard, QNM frequencies.

Figures 6.4 illustrate this behavior for the different types of initial data considered here. In all cases the source decays much faster than the second-order solution itself and therefore can be discarded in determining the behavior of the solution at late times. However, there is one effect in which the source, though small, plays a qualitative role: in determining the length of the ringing period, which in most of the cases, turns out to be longer than for the first-order modes. Elsewhere we will report on detailed analysis of second-order tails. Other way to understand why second-order solutions have the same QNM frequencies as the first-order one is to compare the dynamics of the solutions ${}^{\{1\}}\Psi_\ell^m$, ${}^{\{2\}}\Psi_\ell^m$ themselves and the source term ${}^{\{2\}}\mathcal{S}_\Psi$ of Eq. (6.4). In Fig. 6.5 we plot these three quantities as functions of r for different times in the evolution. It is a generic feature that the source term is dominant only during the first $\sim 20M$, decaying faster to several orders of magnitude below ${}^{\{2\}}\Psi_\ell^m$.

Table 6.1 shows the measured QNM frequencies from our numerical data, for the different initial data types, using a standard least-squares fitting method. The measured frequencies agree very well with those predicted by first-order theory for each of those modes. As described in Sec. 6.3 our numerical solutions (both at first and second-order) are of extreme high resolution. We therefore do not believe that lack of resolution could be the reason why we do not find traces of the predicted

156
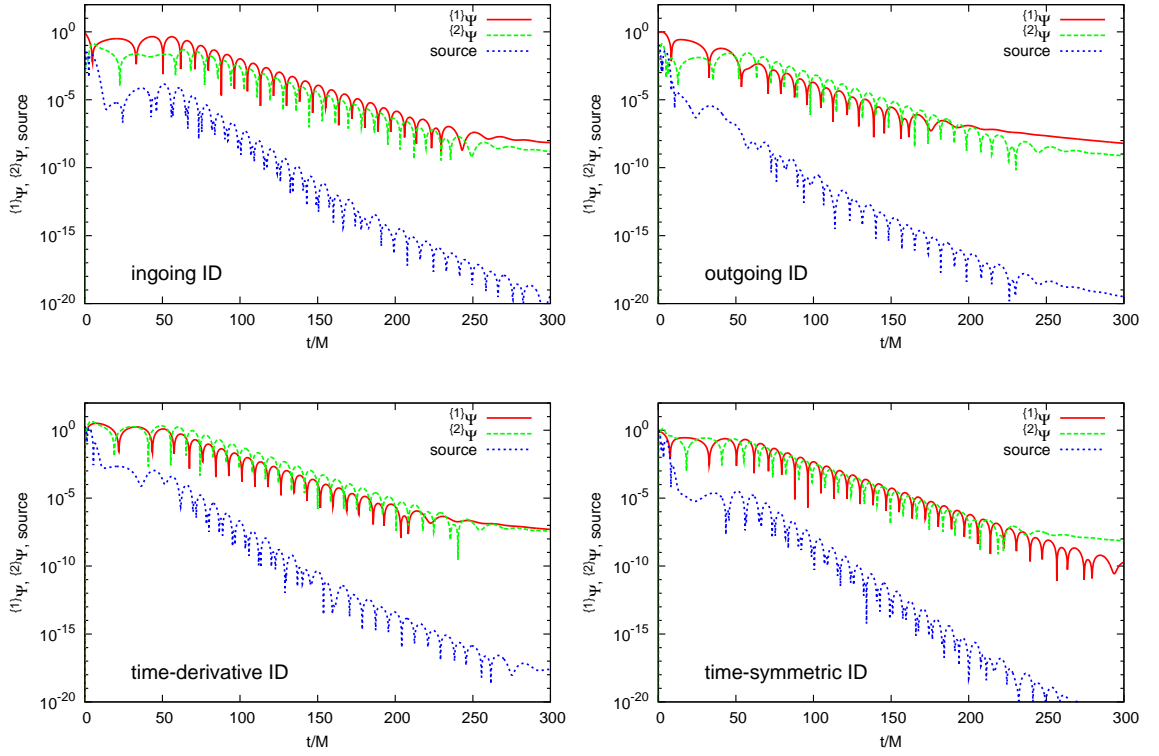
Figure 6.4: $^{\{1\}}\Psi$, $^{\{2\}}\Psi$ and source term as functions of time for different types of initial data. The source plays a role only at very early times, being much smaller than the first and second order solution for most of the evolution.

157
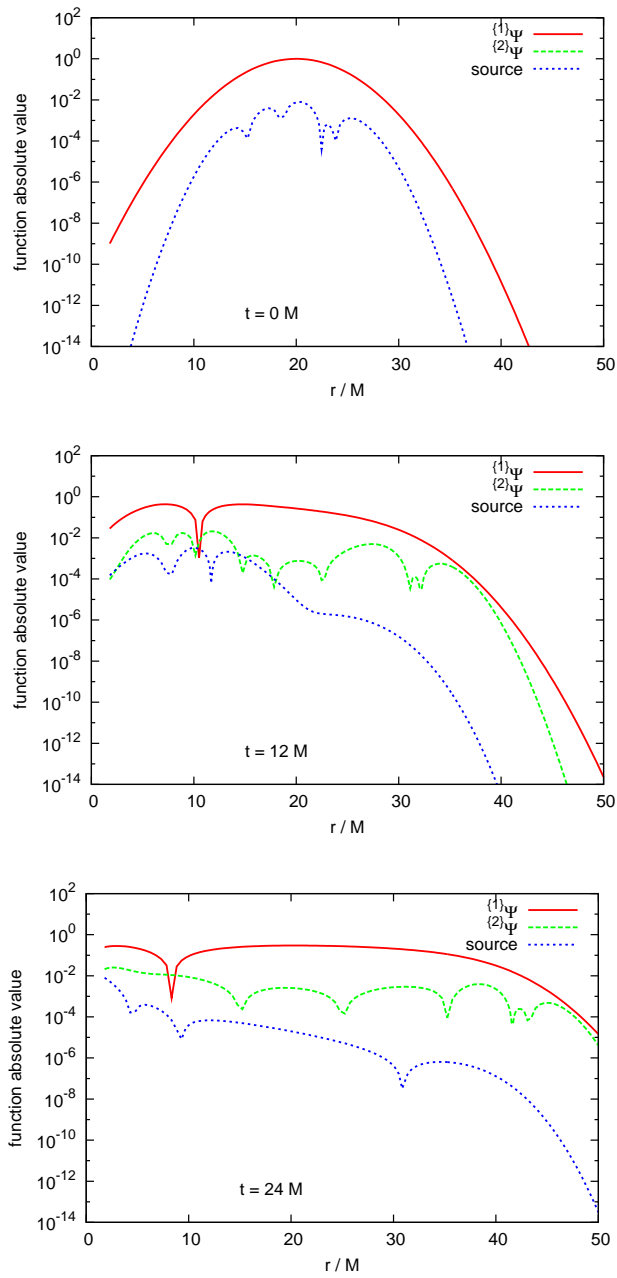
Figure 6.5: Snapshots of the first-order solution $\ell = 2$ and second-order one $(\ell = 4, m = 0)$ along with the source function for the second-order equation for ingoing initial data. The generic behavior of the source is to rapidly decrease several orders of magnitude below the solutions themselves. Notice that the first snapshot corresponds to the initial time therefore the second-order Zerilli function vanishes.

	1st order	2nd order
ID	$\ell = 2$, $m = 2$	$\ell = 2$, $m = 0$
TD	$0.372 - 0.0858i$	$0.374 - 0.0887i$
TS	$0.374 - 0.0886i$	$0.373 - 0.0889i$
IN	$0.374 - 0.0884i$	$0.373 - 0.0896i$
OUT	$0.370 - 0.0877i$	$0.374 - 0.0888i$

	2nd order	
ID	$\ell = 4$, $m = 0$	$\ell = 4$, $m = 4$
TD	$0.807 - 0.0935i$	$0.807 - 0.0935i$
TS	$0.809 - 0.0938i$	$0.809 - 0.0938i$
IN	$0.808 - 0.0929i$	$0.809 - 0.0929i$
OUT	$0.809 - 0.0938i$	$0.809 - 0.0932i$

Table 6.1: Measured QNM frequencies from our numerical simulations. They agree with those predicted by linearized theory, *even* for the second-order modes. These known QNM frequencies are $0.37367 - 0.08896i$ for $\ell = 2$ and $0.80918 - 0.09416i$ for $\ell = 4$ [102].

second-order QNMs. If they are present, they must be excited at such small values that we are having difficulty detecting them with a fitting procedure.

6.4.3 Radiated energy

In order to acquire a broad idea of the behavior of the second order contribution to the radiated energy, we took on the task of exploring a region of the r_0 and σ parameters that characterize our initial data. We evolved the Gaussian perturbation for several values of its initial location r_0 and width σ such that $2M \leq r_0 \leq 10M$ and $1M \leq \sigma \leq 100M$. The result is shown in Fig. 6.6, where the vertical axis represents the ratio between the second-order contributions to the integrated energy [as defined in Eq. (6.8)] compared to the *total* radiated energy at first-order ${}^{\{1\}}E_2^2(t \to \infty) \approx 0.02M$. Calling this ratio ρ_ℓ^m, we have a

$$\rho_\ell^m = \frac{{}^{\{2\}}E_\ell^m}{{}^{\{1\}}E_2^2} \tag{6.9}$$

for each of the three second-order modes mentioned above. Notice that ρ is inversely proportional to the perturbation parameter squared. For this reason, we express ρ in units of $1/\epsilon^2$ in all our plots. The qualitative behavior is very similar for the four initial data types considered here. There are some features worth noticing. For instance, the ratio ρ is larger for values of σ closer to $1M$ and tends to an asymptotic value of $\sim 10^{-3}/\epsilon^2$ as σ becomes larger than $10M$. The ratio ρ_ℓ^m is pretty much insensible to the initial location r_0 for large values of the width σ. However, ρ_ℓ^m tends to increase with r_0 for widths closer to $1M$. The value of ρ_4^0 is always less than ρ_4^4 and ρ_2^0 by one or two orders of magnitude. These last two ratios keep much

160
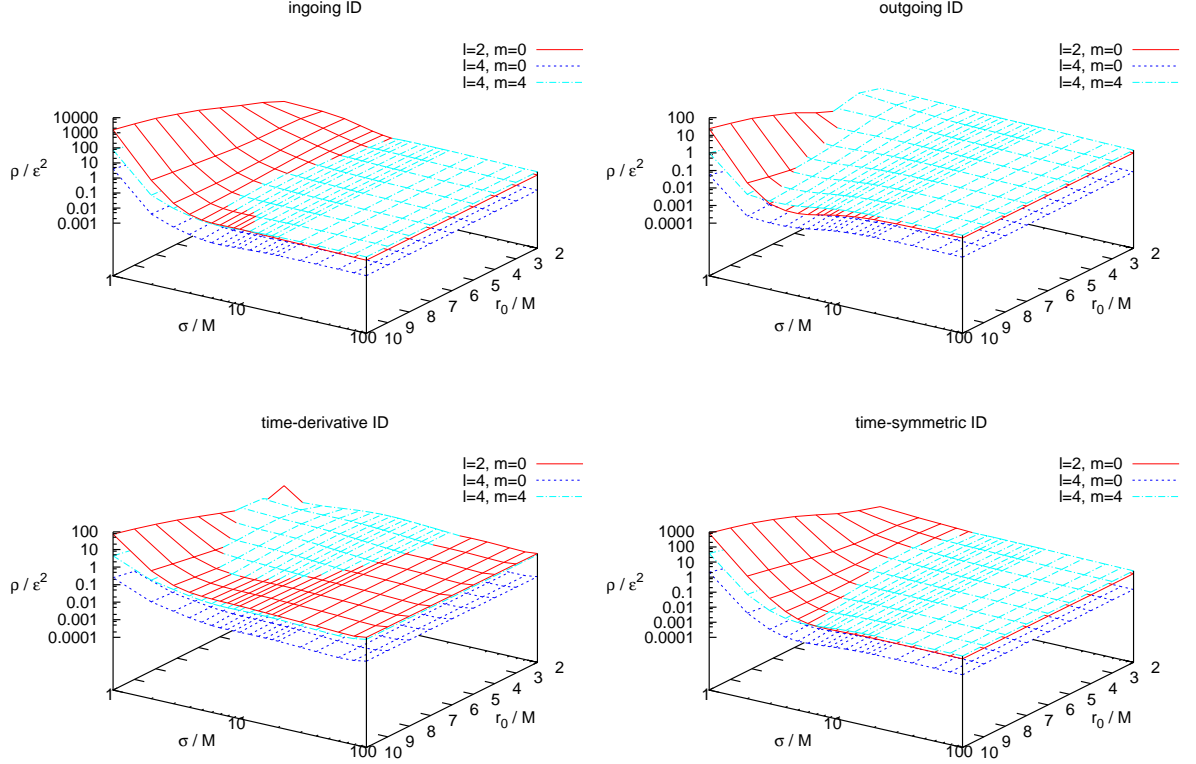
Figure 6.6: Ratio of the radiated energy at second and first perturbation order $\rho_\ell^m = {}^{\{2\}}E_\ell^m / {}^{\{1\}}E_2^2$ for several values of the initial pulse location r_0 and its width σ. Ingoing and time-symmetric initial data are very similar. For the outgoing case, the $\ell = 2$, $m = 0$ mode is dominant only for small widths and large initial locations of the Gaussian pulse. In time-derivative case, the $\ell = 4$, $m = 4$ mode dominates for a specific region of σ and r_0.

closer to each other and it can be seen that $\rho_4^4 > \rho_2^0$ for large σ but the relationship gets inverted when σ is small, being ρ_2^0 the dominant one. This is true for all initial data sets except for the time-symmetric one, where ρ_4^4 is dominant for a subset of the values r_0 and σ considered here.

We discuss our results for OUT (approximately outgoing) initial data, with $r_0 = 20M, \sigma = 4M$ and defer the reader to Tables 6.2 and 6.3 for the same description of the other families of initial data. Figure 6.7 shows the ratio ρ_ℓ^m as a function

of time for a fixed observer at $r = 51M$ (top panel) and as a function of r for a time $t = 2000M$ (bottom panel). The two leading induced modes, $(\ell = 2, m = 0)$ and $(\ell = 4, m = 4)$ contribute to around $0.1\epsilon^2\%$ of the total radiated energy $^{\{1\}}E_2^2$. This indicates that non-linearities in the ringdown process of a binary black hole collision are important.

The ratio ρ_ℓ^m in Fig. 6.7 can be understood as the error one is commiting when neglecting the nonlinearities by considering a linear perturbative scheme to extract the gravitational waves. In agreement with the common belief, the relative contributions of the high-order modes to the radiated energy become smaller with larger extraction radius. Even though, as expected, this decreasing tendency becomes constant from certain specific value of the radius ($r \approx 40M$ for this evolution) on. Therefore, this systematic error can not be improved by increasing the extraction radius further than the mentioned specific value. That is, from certain distance on, *relative to the total radiated energy, non-linearities do not become less important far away from the source.* This feature is independent of the type of initial data.

A natural question is how much the induced, second-order radiated energy depends on the location of the first-order perturbation. In order to answer that question we compute the radiated energy for a family of different initial data, changing r_0 and looking at the relative amplitude of the second-order modes among themselves, as a function of r_0. More precisely, we compute the ratios $^{\{2\}}E_4^0/{}^{\{2\}}E_2^0$ and $^{\{2\}}E_4^4/{}^{\{2\}}E_2^0$, all of them evaluated at large enough times (i.e. we compute the total radiated energy) as a function of r_0. The advantage of looking at these ratios is that they are independent of the 'size' of the perturbation ϵ. Figure 6.8 shows the
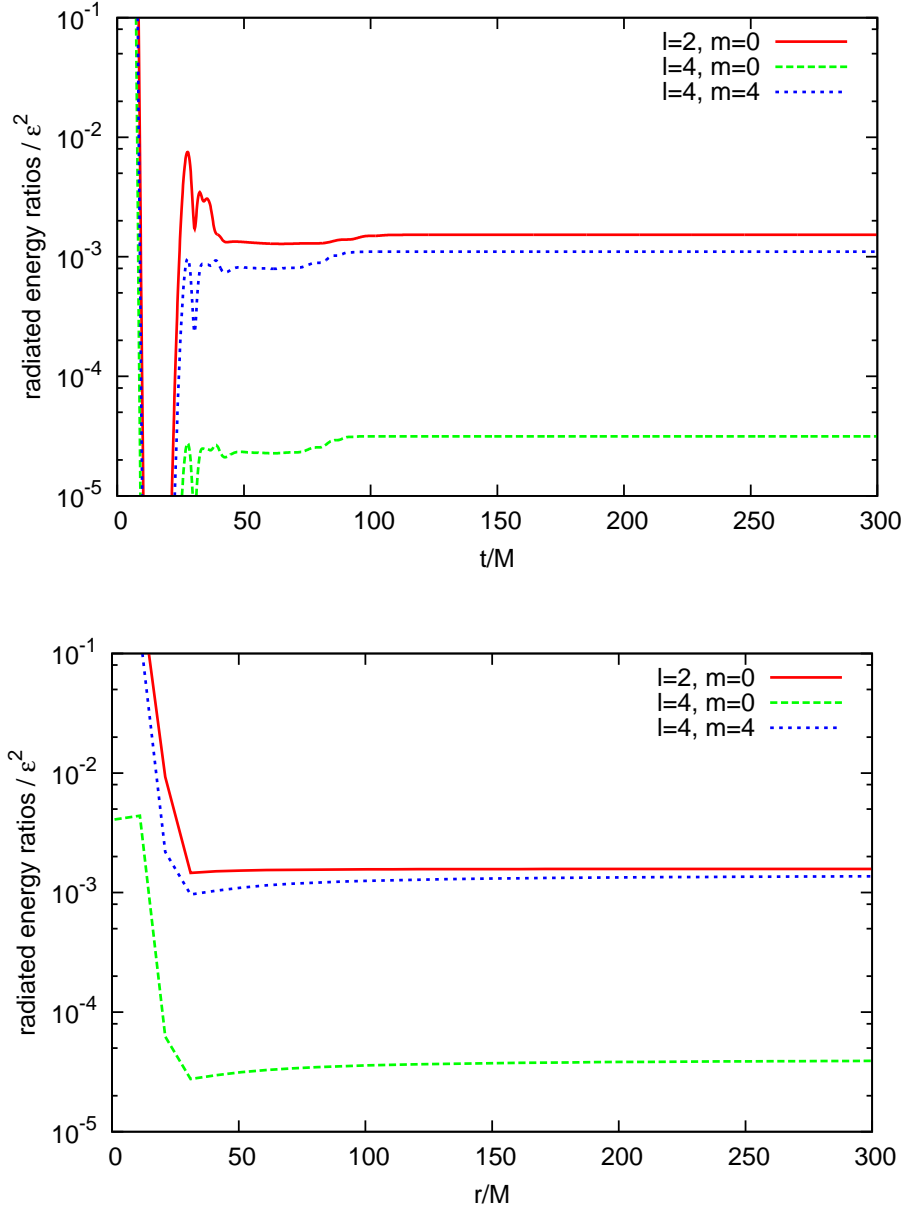
Figure 6.7: Ratio ${}^{\{2\}}E_\ell^m / {}^{\{1\}}E_2^2$ of the radiated energy as function of time (top) for an observer located at $r = 51M$. The same quantity is ploted as a function of the radial coordinate r (bottom) for a time $t = 2000M$.
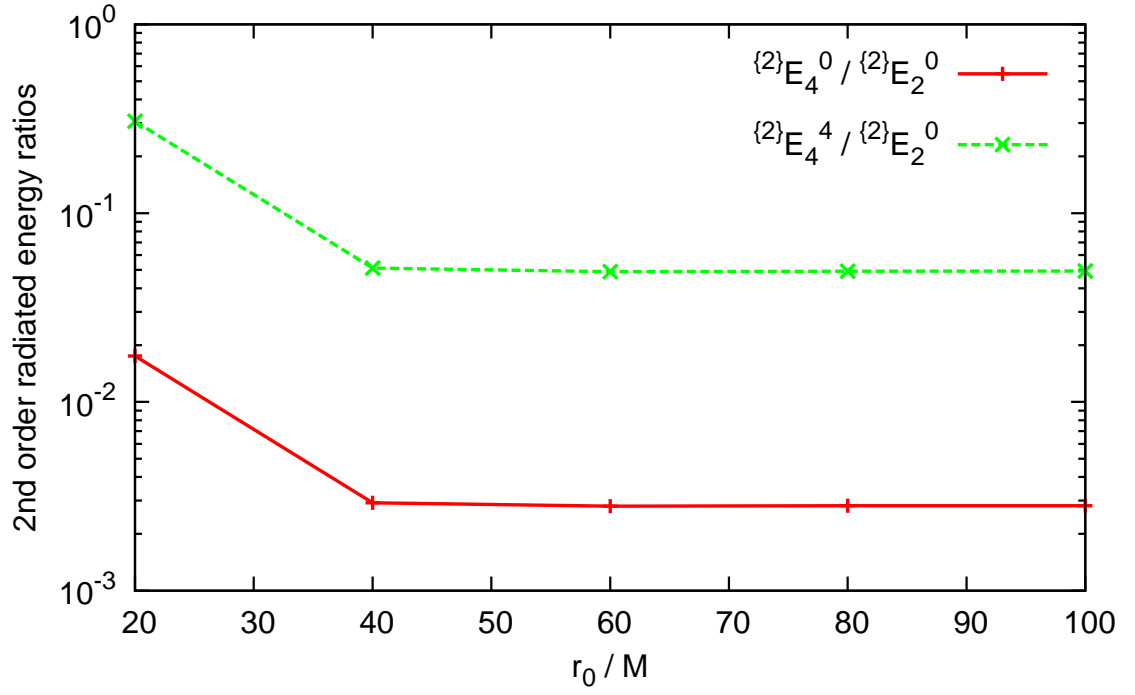
Figure 6.8: Ratios between the total radiated energy from the different second-order modes versus r_0 for OUT initial data.

r_0	TD	TS	OUT	IN
20	0.01119	0.00287	0.01752	0.068467
40	0.00392	0.00260	0.00292	0.059240
60	0.00320	0.00271	0.00280	0.058925
80	0.00304	0.00275	0.00282	0.058946
100	0.00298	0.00276	0.00282	0.058950

Table 6.2: ${}^{\{2\}}E_4^0 / {}^{\{2\}}E_2^0$

164

r_0	TD	TS	OUT	IN
20	0.19590	0.05030	0.30670	1.1981
40	0.06860	0.04551	0.05111	1.0367
60	0.05611	0.04746	0.04901	1.0312
80	0.05329	0.04814	0.04931	1.0315
100	0.05225	0.04839	0.04937	1.0316

Table 6.3: $^{\{2\}}E_4^4 / {}^{\{2\}}E_2^0$

results, which indicate that these ratios are rather independent of the location of the initial data. This property holds for all the other initial data types as well.

6.5 Concluding remarks

We have carried out a sistematic study of generic first and second-order perturbations for the specific case of the self-coupling of a first-order mode. We found that the second-order correction to the radiated energy at first-order is roughly of $0.1\epsilon^2\%$. It remains to quantify the value of the perturbation parameter ϵ. One way in which this could be done is to compare the radial dependence of the Zerilli function for the binary black hole case. To simplify the scenario one could take a head-on collision of equal mass non-spinning black holes. The idea would be to mimic the Zerilli profile just after merger with the initial data supplied to the perturbation equations. Then a comparison of the amount of radiated energy in both cases should gives us an estimation of ϵ.

Work in this direction is currently under development and we plan to present the full report in the near future.

Chapter 7

General conclusions

We have presented different studies in the context of numerical relativity and black hole perturbation theory. Below we summarize general remarks and conclusions presented in this dissertation.

High order finite difference techniques combined with a multiblock domain decomposition provide a powerful tool for numerical analysis. The scope of these methods is not restricted to numerical relativity. We have shown the success of these methods starting from a spherically symmetric version of Einstein equations in Chapter 2, a full three-dimensional implementation for a single black hole in Chapter 3 and the binary black hole problem (also three-dimensional) in Chapter 4. For the reasons mentioned in those chapters, multiblock methods are a viable alternative to the more common adaptive mesh refinement approach.

Pseudo-spectral collocations methods are also used in our analysis. The great advantage of spectral methods is their high accuracy. In Chapter 6 we were able to obtain numerical solutions with errors of the order of double-precision round-off. This is important, since we can rule out numerical error as a source of possible inconsistencies in our results. The multiblock domain decomposition idea is also used in this relatively easy problem, in conjunction with spectral methods. In this particular case this is useful since the distribution of grid points tends to accumulate

them at the boundaries of the domain. Therefore, covering the whole domain with a single block would demand more points than using several blocks to achieve a reasonable resolution where grid points are more sparse.

We have done a quantitative assessment of the quality of the waveforms computed with the Regge-Wheeler-Zerilli perturbative method. The main point being that extraction at a finite distance contains an error that does not converge to zero as the resolution of the simulation is increased (Chapter 3). This error comes from a wrong identification of the background spacetime coordinates in the perturbative formalism. A way of eradicating this systematic error is to extrapolate the waveforms to infinity. In Chapter 5 we see that this is indeed the case. However there is still room to play with the procedure to carry out the extrapolation.

Chapter 5 also serves as evidence for the usefulness of the turducken approach, whereby initial data with excised black holes is used in a non-excised topologically trivial domain. The idea behind is that the interior of the black hole can be replaced with any smooth function without constraint-violating modes entering the computational domain from the black holes. This method effectively stretches a bridge between initial data sets that are constructed in a domain where the black holes are excised from the numerical grid.

In Chapter 6 we have used second order perturbation theory to compute the energy contribution of self-coupling first order modes. By evolving generic perturbations of a Schwarzschild black hole we found that the fraction of energy carried out by second order modes is of the order of $0.1\epsilon^2\%$. This quantity depends on the size of the perturbation parameter ϵ which could be set by comparing perturbative

estimations with full numerical relativity results.

Appendix A

Vector and tensor spherical harmonic decomposition (odd *and* even-parity sectors)

We discuss now, in some detail, how to compute a multipole decomposition using vector and tensor spherical harmonics. A vector field V_A defined on the manifold S^2 can be decomposed in multipoles using even and odd-parity basis vectors. Denoting the components in this basis by $h_{\text{even}}^{(\ell,m)}$ and $h_{\text{odd}}^{(\ell,m)}$, V_A can be written as

$$V_A = \sum_{\ell=1}^{\infty} \sum_{m=-\ell}^{\ell} h_{\text{even}}^{(\ell,m)} Y_A^{(\ell,m)} + h_{\text{odd}}^{(\ell,m)} S_A^{(\ell,m)}. \tag{A.1}$$

Here, $Y_A^{(\ell,m)}$ and $S_A^{(\ell,m)}$ are the even and odd-parity basis vectors tangent to the sphere, respectively. They are defined as

$$Y_A^{(\ell,m)} = \hat{\nabla}_A Y^{(\ell,m)} \tag{A.2}$$

$$S_A^{(\ell,m)} = \hat{\epsilon}_A^B \hat{\nabla}_B Y^{(\ell,m)}, \tag{A.3}$$

where $\hat{\nabla}_A$ is the covariant derivative compatible with the unit sphere metric $\hat{g}_{AB}$ and $\hat{\epsilon}_{AB}$ is the Levi-Civita tensor with components $\hat{\epsilon}_{\theta\phi} = \sin\theta$. They satisfy the relations $\hat{\nabla}_C \hat{g}_{AB} = 0$ and $\hat{\nabla}_C \hat{\epsilon}_{AB} = 0$. These vectors obey the orthogonality relations

$$\int \hat{g}^{AB} \bar{Y}_A^{(\ell,m)} Y_B^{(\ell'm')} d\Omega = \ell(\ell+1)\delta_{\ell\ell'}\delta_{mm'}, \tag{A.4}$$

$$\int \hat{g}^{AB} \bar{S}_A^{(\ell,m)} S_B^{(\ell'm')} d\Omega = \ell(\ell+1)\delta_{\ell\ell'}\delta_{mm'}, \tag{A.5}$$

$$\int \hat{g}^{AB} Y_A^{(\ell,m)} S_B^{(\ell'm')} d\Omega = 0. \tag{A.6}$$

Here $d\Omega = \sin\theta\, d\theta\, d\phi$ is the area element in polar spherical coordinates and the bar denotes complex conjugation. Using the orthogonality property we can find the multipole modes $h_{\text{even}}^{(\ell,m)}$ and $h_{\text{odd}}^{(\ell,m)}$. The result is

$$h_{\text{even}}^{(\ell,m)} = \frac{1}{\ell(\ell+1)}\int \hat{g}^{AB}V_A\bar{Y}_B^{(\ell,m)}\, d\Omega, \tag{A.7}$$

$$h_{\text{odd}}^{(\ell,m)} = \frac{1}{\ell(\ell+1)}\int \hat{g}^{AB}V_A\bar{S}_B^{(\ell,m)}\, d\Omega. \tag{A.8}$$

Using spherical coordinates the components of the even-parity basis are

$$Y_\theta^{(\ell,m)} = \partial_\theta Y^{(\ell,m)} \tag{A.9}$$

$$Y_\phi^{(\ell,m)} = \partial_\phi Y^{(\ell,m)}. \tag{A.10}$$

For the odd parity we get

$$S_\theta^{(\ell,m)} = -\frac{1}{\sin\theta}\partial_\phi Y^{(\ell,m)} \tag{A.11}$$

$$S_\phi^{(\ell,m)} = \sin\theta\, \partial_\theta Y^{(\ell,m)}. \tag{A.12}$$

Expanding the integral with these vector components we obtain that

$$h_{\text{even}}^{(\ell,m)} = \frac{1}{\ell(\ell+1)}\int V_\theta\bar{Y}_\theta^{(\ell,m)} + \frac{1}{\sin^2\theta}V_\phi\bar{Y}_\phi^{(\ell,m)}\, d\Omega, \tag{A.13}$$

$$h_{\text{odd}}^{(\ell,m)} = \frac{1}{\ell(\ell+1)}\int \frac{1}{\sin\theta}\left(V_\phi\bar{Y}_\theta^{(\ell,m)} - V_\theta\bar{Y}_\phi^{(\ell,m)}\right)\, d\Omega. \tag{A.14}$$

For tensors, the idea is the same. If V_{AB} is a tensor field defined on the unit sphere, the multipole decomposition takes the form

$$V_{AB} = \sum_{\ell=2}^{\infty}\sum_{m=-\ell}^{\ell} K^{(\ell,m)}\hat{g}_{AB}Y^{(\ell,m)} + G^{(\ell,m)}Y_{AB}^{(\ell,m)} + h_2^{(\ell,m)}S_{AB}^{(\ell,m)}, \tag{A.15}$$

where $\hat{g}_{AB}Y^{(\ell,m)}$ and $Y_{AB}^{(\ell,m)}$ are the even-parity tensor basis, whereas $S_{AB}^{(\ell,m)}$ is the odd-parity tensor basis. We follow the Regge–Wheeler notation by using K and G

for the even-parity components and h_2 for the odd-parity one. The tensor basis is defined as

$$Y_{AB}^{(\ell,m)} = \hat{\nabla}_A \hat{\nabla}_B Y^{(\ell,m)} + \frac{1}{2}\ell(\ell+1)\hat{g}_{AB} Y^{(\ell,m)} \tag{A.16}$$

$$S_{AB}^{(\ell,m)} = \frac{1}{2}\left(\hat{\nabla}_A S_B^{(\ell,m)} + \hat{\nabla}_B S_A^{(\ell,m)}\right) \tag{A.17}$$

This definition agrees with Zerilli tensor harmonics up to a factor of 2, as we will see. They obey the orthogonality relations

$$\int \hat{g}^{AC}\hat{g}^{BD}\bar{Y}_{CD}^{(\ell,m)}Y_{AB}^{\ell' m'}\, d\Omega = \frac{1}{2}\ell(\ell-1)(\ell+1)(\ell+2)\delta_{\ell\ell'}\delta_{mm'}, \tag{A.18}$$

$$\int \hat{g}^{AC}\hat{g}^{BD}\bar{S}_{CD}^{(\ell,m)}S_{AB}^{\ell' m'}\, d\Omega = \frac{1}{2}\ell(\ell-1)(\ell+1)(\ell+2)\delta_{\ell\ell'}\delta_{mm'}, \tag{A.19}$$

and integration of the product of two different tensor basis vanishes. With this we can find K, G and h_2. The result is

$$K^{(\ell,m)} = \frac{1}{2}\int V_{AB}g^{AB}\bar{Y}^{\ell m}\, d\Omega \tag{A.20}$$

$$G^{(\ell,m)} = \frac{2}{\ell(\ell-1)(\ell+1)(\ell+2)}\int \hat{g}^{AC}\hat{g}^{BD}V_{AB}\bar{Y}_{CD}^{(\ell,m)}\, d\Omega \tag{A.21}$$

$$h_2^{(\ell,m)} = \frac{2}{\ell(\ell-1)(\ell+1)(\ell+2)}\int \hat{g}^{AC}\hat{g}^{BD}V_{AB}\bar{S}_{CD}^{(\ell,m)}\, d\Omega \tag{A.22}$$

Using spherical coordinates the components of the basis are

$$Y_{\theta\theta}^{(\ell,m)} = \frac{1}{2}W^{(\ell,m)} \tag{A.23}$$

$$Y_{\theta\phi}^{(\ell,m)} = \frac{1}{2}X^{(\ell,m)} \tag{A.24}$$

$$Y_{\phi\phi}^{(\ell,m)} = -\frac{1}{2}\sin^2\theta\, W^{(\ell,m)} \tag{A.25}$$

$$S_{\theta\theta}^{(\ell,m)} = -\frac{1}{2\sin\theta}X^{(\ell,m)} \tag{A.26}$$

$$S_{\theta\phi}^{(\ell,m)} = \frac{1}{2}\sin\theta\, W^{(\ell,m)} \tag{A.27}$$

$$S_{\phi\phi}^{(\ell,m)} = \frac{1}{2}\sin\theta\, X^{(\ell,m)}, \tag{A.28}$$

172

where $W^{(\ell,m)}$ and $X^{(\ell,m)}$ are defined by Zerilli [179] as

$$W^{(\ell,m)} = 2\left[\partial_\theta^2 + \frac{1}{2}\ell(\ell+1)\right]Y^{(\ell,m)} \tag{A.29}$$

$$X^{(\ell,m)} = 2\partial_\phi\left(\partial_\theta - \cot\theta\right)Y^{(\ell,m)}. \tag{A.30}$$

Assuming that V_{AB} is a symmetric tensor and abbreviating the normalization constant as $L = \ell(\ell-1)(\ell+1)(\ell+2)$, we expand the integrals to get

$$K^{(\ell,m)} = \frac{1}{2}\int\left(V_{\theta\theta} + \frac{V_{\phi\phi}}{\sin^2\theta}\right)\bar{Y}^{(\ell,m)}\,d\Omega \tag{A.31}$$

$$G^{(\ell,m)} = \frac{1}{L}\int V_{\theta\theta}\bar{W}^{(\ell,m)} + \frac{1}{\sin^2\theta}\left(2V_{\theta\phi}\bar{X}^{(\ell,m)} - V_{\phi\phi}\bar{W}^{(\ell,m)}\right)\,d\Omega \tag{A.32}$$

$$h_2^{(\ell,m)} = \frac{1}{L}\int\frac{V_{\phi\phi}}{\sin^3\theta}\bar{X}^{(\ell,m)} + 2\frac{V_{\theta\phi}}{\sin\theta}\bar{W}^{(\ell,m)} - \frac{V_{\theta\theta}}{\sin\theta}\bar{X}^{(\ell,m)}\,d\Omega \tag{A.33}$$

The $Y^{\ell m}$ are normalized with respect to the standard metric $\hat{g}_{AB}$ on S^2, an exception being the cases $\ell = 0$ and $\ell = 1$; where we choose the normalization such that $Y^{0,0} = 1$, and $\int_{S^2}Y^{1,m}\bar{Y}^{1,m}d\Omega = 4\pi/3$.

Bibliography

[1] A. Abrahams and R. Price. Applying black hole perturbation theory to numerically generated spacetimes. *Phys. Rev. D*, 53:163, 1996.

[2] A. M. Abrahams, L. Rezzolla, M. E. Rupright, A. Anderson, Peter Anninos, Thomas W. Baumgarte, N. T. Bishop, S. R. Brandt, J. C. Browne, K. Camarda, M. W. Choptuik, Gregory B. Cook, R. R. Correll, C. R. Evans, L. S. Finn, G. C. Fox, R. Gómez, T. Haupt, M. F. Huq, L. E. Kidder, S. A. Klasky, P. Laguna, W. Landry, L. Lehner, J. Lenaghan, R. L. Marsa, J. Massó, R. A. Matzner, S. Mitra, P. Papadopoulos, M. Parashar, F. Saied, P. E. Saylor, Mark A. Scheel, E. Seidel, Stuart L. Shapiro, D. Shoemaker, L. Smarr, B. Szilagyi, Saul A. Teukolsky, M. H. P. M. van Putten, P. Walker, J. Winicour, and Jr J. W. York. Gravitational wave extraction and outer boundary conditions by perturbative matching. *Phys. Rev. Lett.*, 80:1812–1815, 1998.

[3] Andrew Abrahams. Analytic-numerical matching for gravitational waveform extraction. In C. Evans, L. Finn, and D. Hobill, editors, *Frontiers in Numerical Relativity*. Cambridge University Press, Cambridge, England, 1989.

[4] Andrew Abrahams and C. Evans. Reading off gravitational radiation waveforms in numerical relativity calculations: Matching to linearised gravity. *Phys. Rev. D*, 37:318–332, 1988.

[5] Andrew Abrahams and C. Evans. Gauge invariant treatment of gravitational radiation near the source: Analysis and numerical simulations. *Phys. Rev. D*, 42:2585–2594, 1990.

[6] A. A. Abramovici, W. Althouse, R. P. Drever, Y. Gursel, S. Kawamura, F. Raab, D. Shoemaker, L. Sievers, R. Spero, K. S. Thorne, R. Vogt, R. Weiss, S. Whitcomb, and M. Zuker. Ligo: The laser interferometer gravitational-wave observatory. *Science*, 256:325–333, 1992.

[7] Miguel Alcubierre, G. Allen, B. Brügmann, G. Lanfermann, E. Seidel, W.-M. Suen, and M. Tobias. Gravitational collapse of gravitational waves in 3D numerical relativity. *Phys. Rev. D*, 61:041501 (R), 2000.

[8] Miguel Alcubierre, W. Benger, B. Brügmann, G. Lanfermann, L. Nerger, E. Seidel, and R. Takahashi. 3D Grazing Collision of Two Black Holes. *Phys. Rev. Lett.*, 87:271103, 2001.

[9] Miguel Alcubierre, Bernd Brügmann, Peter Diener, Frank Herrmann, Denis Pollney, Edward Seidel, and Ryoji Takahashi. Testing excision techniques for dynamical 3D black hole evolutions. submitted to Phys. Rev. D, 2004.

[10] Miguel Alcubierre, Bernd Brügmann, Peter Diener, Michael Koppitz, Denis Pollney, Edward Seidel, and Ryoji Takahashi. Gauge conditions for long-term numerical black hole evolutions without excision. *Phys. Rev. D*, 67:084023, 2003.

[11] Miguel Alcubierre, Bernd Brügmann, Denis Pollney, Edward Seidel, and Ryoji Takahashi. Black hole excision for dynamic black holes. *Phys. Rev. D*, 64:061501(R), 2001.

[12] Miguel Alcubierre et al. Toward standard testbeds for numerical relativity. *Class. Quant. Grav.*, 21:589, 2004.

[13] A. Anderson and J. W. York. Fixing Einstein's equations. *Phy. Rev. Lett.*, 82:4384–4387, 1999.

[14] Marcus Ansorg. A double-domain spectral method for black hole excision data. *Phys. Rev. D*, 72:024018, 2005.

[15] Marcus Ansorg, Bernd Brügmann, and Wolfgang Tichy. A single-domain spectral method for black hole puncture data. *Phys. Rev. D*, 70:064011, 2004.

[16] Luca Baiotti, Bruno Giacomazzo, and Luciano Rezzolla. Accurate evolutions of inspiralling neutron-star binaries: prompt and delayed collapse to black hole. *Phys. Rev.*, D78:084033, 2008.

[17] J. Baker, S. R. Brandt, M. Campanelli, C. O. Lousto, E. Seidel, and R. Takahashi. Nonlinear and perturbative evolution of distorted black holes: Odd-parity modes. *Phys. Rev. D*, 62:127701, 2000. gr-qc/9911017.

[18] John Baker, Manuela Campanelli, and Carlos O. Lousto. The Lazarus project: A pragmatic approach to binary black hole evolutions. *Phys. Rev. D*, 65:044001, 2002.

[19] John G. Baker, Joan Centrella, Dae-Il Choi, Michael Koppitz, and James van Meter. Binary black hole merger dynamics and waveforms. *Phys. Rev.*, D73:104002, 2006.

[20] John G. Baker, Joan Centrella, Dae-Il Choi, Michael Koppitz, and James van Meter. Gravitational wave extraction from an inspiraling configuration of merging black holes. *Phys. Rev. Lett.*, 96:111102, 2006.

[21] Thomas W. Baumgarte and Stuart L. Shapiro. On the numerical integration of Einstein's field equations. *Phys. Rev. D*, 59:024007, 1999.

[22] Christopher Beetle, Marco Bruni, Lior M. Burko, and Andrea Nerozzi. Towards wave extraction in numerical relativity: Foundations and initial-value formulation. *Phys. Rev. D*, 72:024013, 2005.

[23] Jacob D. Bekenstein. Black holes: Classical properties, thermodynamics, and heuristic quantization. 1998.

[24] E. Berti, V. Cardoso, and C. M. Will. Black hole spectroscopy with LISA. *AIP Conf. Proc.*, 873:82–88, 2006.

[25] Emanuele Berti and Vitor Cardoso. Quasinormal ringing of kerr black holes. I: The excitation factors. *Phys. Rev. D*, 74:104020, 2006.

[26] Emanuele Berti, Vitor Cardoso, and Andrei O. Starinets. Quasinormal modes of black holes and black branes. *Class. Quant. Grav.*, 26:163001, 2009.

[27] Emanuele Berti, Vitor Cardoso, and Clifford M. Will. On gravitational-wave spectroscopy of massive black holes with the space interferometer LISA. *Phys. Rev.*, D73:064030, 2006.

[28] N. T. Bishop, R. Gómez, L. Lehner, and J. Winicour. Cauchy-characteristic extraction in numerical relativity. *Phys. Rev. D*, 54:6153–6165, 1996.

[29] Luc Blanchet, L. P. Grishchuk, and Gerhard Schaefer. Post-Newtonian approximations, compact binaries, and strong-field tests of gravity. 2007.

[30] Michael Boyle et al. High-accuracy comparison of numerical relativity simulations with post-Newtonian expansions. *Phys. Rev.*, D76:124038, 2007.

[31] Patrick R. Brady, Jolien D. E. Creighton, and Kip S. Thorne. Computing the merger of black-hole binaries: the ibbh problem. *Phys. Rev. D*, 58:061501, 1998.

[32] S. Brandt, J. A. Font, J. M. Ibáñez, Joan Massó, and E. Seidel. Numerical evolution of matter in dynamical axisymmetric black hole spacetimes. I. method and tests. *Comp. Phys. Comm.*, 124:169–196, 2000.

[33] S. R. Brandt and E. Seidel. Evolution of distorted rotating black holes II: Dynamics and analysis. *Phys. Rev. D*, 52(2):870–886, 1995.

[34] David Brizuela, Jose M. Martin-Garcia, and Guillermo A. Mena Marugan. Second and higher-order perturbations of a spherical spacetime. *Phys. Rev.*, D74:044039, 2006.

[35] David Brizuela, José M. Martín-García, and Guillermo A. Mena Marugán. xPert: Computer algebra for metric perturbation theory. *Gen. Rel. Grav.*, 2009.

[36] David Brizuela, Jose M. Martin-Garcia, and Manuel Tiglio. A complete gauge-invariant formalism for arbitrary second- order perturbations of a Schwarzschild black hole. *Phys. Rev.*, D80:024021, 2009.

[37] O. Brodbeck, S. Frittelli, P. Hübner, and O. A. Reula. Einstein's equations with asymptotically stable constraint propogation. *J. Math. Phys.*, 40:909–923, 1999.

[38] David Brown, Peter Diener, Olivier Sarbach, Erik Schnetter, and Manuel Tiglio. Turduckening black holes: an analytical and computational study. 2008.

[39] David Brown, Peter Diener, Olivier Sarbach, Erik Schnetter, and Manuel Tiglio. Turduckening black holes: an analytical and computational study. *Phys. Rev.*, D79:044023, 2009.

[40] David Brown, Olivier Sarbach, Erik Schnetter, Manuel Tiglio, Peter Diener, Ian Hawke, and Denis Pollney. Excision without excision. *Phys. Rev. D*, 76:081503(R), 2007.

[41] Bernd Bruegmann et al. Calibration of Moving Puncture Simulations. *Phys. Rev.*, D77:024027, 2008.

[42] Bernd Brügmann, Wolfgang Tichy, and Nina Jansen. Numerical simulation of orbiting black holes. *Phys. Rev. Lett.*, 92:211101, 2004.

[43] Bernard F. Schutz B.S. Sathyaprakash. Physics, astrophysics and cosmology with gravitational waves. *Living Reviews in Relativity*, 12(2), 2009.

[44] Alessandra Buonanno, Gregory B. Cook, and Frans Pretorius. Inspiral, merger and ring-down of equal-mass black-hole binaries. *Phys. Rev.*, D75:124018, 2007.

[45] Lior M. Burko, Thomas W. Baumgarte, and Christopher Beetle. Towards a novel wave–extraction method for numerical relativity: III. analytical examples for the Beetle–Burko radiation scalar. *Phys. Rev. D*, 73:024002, 2006.

[46] Cactus. http://www.cactuscode.org.

[47] G. Calabrese, L. Lehner, and M. Tiglio. Constraint-preserving boundary conditions in numerical relativity. *Phys. Rev. D*, 65(10):104031–+, May 2002.

[48] Gioel Calabrese, Luis Lehner, David Neilsen, Jorge Pullin, Oscar Reula, Olivier Sarbach, and Manuel Tiglio. Novel finite-differencing techniques for numerical relativity: application to black hole excision. *Class. Quantum Grav.*, 20:L245–L252, 2003.

[49] Gioel Calabrese, Luis Lehner, Oscar Reula, Olivier Sarbach, and Manuel Tiglio. Summation by parts and dissipation for domains with excised regions. *Class. Quantum Grav.*, 21:5735–5758, 2004.

[50] K. Camarda and E. Seidel. Numerical evolution of dynamic 3D black holes: Extracting waves. *Phys. Rev. D*, 57:R3204, 1998.

[51] K. Camarda and E. Seidel. Three-dimensional simulations of distorted black holes: Comparison with axisymmetric results. *Phys. Rev. D*, 59:064019, 1999.

[52] M. Campanelli and C. O. Lousto. Second order gauge invariant gravitational perturbations of a Kerr black hole. *Phys. Rev. D*, 59:124022, 1999.

[53] Manuela Campanelli, Bernard J. Kelly, and Carlos O. Lousto. The Lazarus Project II: Space-like extraction with the Quasi-Kinnersley tetrad. *Phys. Rev.*, D73:064005, 2006.

[54] Manuela Campanelli, C. O. Lousto, P. Marronetti, and Y. Zlochower. Accurate evolutions of orbiting black-hole binaries without excision. *Phys. Rev. Lett.*, 96:111101, 2006.

[55] Manuela Campanelli and Carlos O. Lousto. Second order gauge invariant gravitational perturbations of a Kerr black hole. *Phys. Rev.*, D59:124022, 1999.

[56] M. Carpenter, D. Gottlieb, and S. Abarbanel. Time-stable boundary conditions for finite-difference schemes solving hyperbolic systems. methodology and application to high-order compact schemes. *J. Comput. Phys.*, 111:220–236, 1994.

[57] M. Carpenter, J. Nordström, and D. Gottlieb. A stable and conservative interface treatment of arbitrary spatial accuracy. *J. Comput. Phys.*, 148(2):341, 1999.

[58] Carpet. `http://www.carpetcode.org`.

[59] S. Chandrasekhar. *The Mathematical Theory of Black Holes*. Oxford University Press, Oxford, England, 1983.

[60] S. Chandrasekhar. *The mathematical theory of black holes*. Oxford University Press, New York, 1992.

[61] Peter Diener, Ernst Nils Dorband, Erik Schnetter, and Manuel Tiglio. New, efficient, and accurate high order derivative and dissipation operators satisfying summation by parts, and applications in three-dimensional multi-block evolutions. in preparation, 2005.

[62] Peter Diener, Ernst Nils Dorband, Erik Schnetter, and Manuel Tiglio. New, efficient, and accurate high order derivative and dissipation operators satisfying summation by parts, and applications in three-dimensional multi-block evolutions. *J. Sci. Comput.*, 32:109–145, 2007.

[63] Peter Diener et al. Accurate evolution of orbiting binary black holes. *Phys. Rev. Lett.*, 96:121101, 2006.

[64] Ernst Nils Dorband, Emanuele Berti, Peter Diener, Erik Schnetter, and Manuel Tiglio. A numerical study of the quasinormal mode excitation of Kerr black holes. *Phys. Rev.*, D74:084028, 2006.

[65] Ernst Nils Dorband, Emanuele Berti, Peter Diener, Erik Schnetter, and Manuel Tiglio. A numerical study of the quasinormal mode excitation of Kerr black holes. *Phys. Rev. D*, 74:084028, 2006.

[66] Olaf Dreyer et al. Black hole spectroscopy: Testing general relativity through gravitational wave observations. *Class. Quant. Grav.*, 21:787–804, 2004.

[67] Matthew D. Duez et al. Evolving black hole-neutron star binaries in general relativity using pseudospectral and finite difference methods. *Phys. Rev.*, D78:104015, 2008.

[68] Matthew D. Duez, Stuart L. Shapiro, and Hwei-Jang Yo. Relativistic hydrodynamic evolutions with black hole excision. *Phys. Rev. D*, 69:104016, 2004.

[69] Éanna É. Flanagan and Scott A. Hughes. Measuring gravitational waves from binary black hole coalescence: I. signal to noise for inspiral, merger, and ringdown. *Phys. Rev. D*, 57:4535, 1998.

[70] A. Einstein. Die feldgleichungen der gravitation. *Preuss. Akad. Wiss. Berlin, Sitzber*, pages 844–847, 1915.

[71] R. Epstein and R. V. Wagoner. Post-newtonian generation of gravitational waves. *Astrophys. J.*, 197:717–23, 1975.

[72] David R. Fiske, John G. Baker, James R. van Meter, Dae-Il Choi, and Joan M. Centrella. Wave zone extraction of gravitational radiation in three-dimensional numerical relativity. *Phys. Rev. D*, 71:104036, 2005. gr-qc/0503100.

[73] P. Chris Fragile, Christopher C. Lindner, Peter Anninos, and Jay D. Salmonson. Application of the Cubed-Sphere Grid to Tilted Black-Hole Accretion Disks. *Astrophys. J.*, 691:482–494, 2009.

[74] H. Friedrich. On the hyperbolicity of Einstein's and other gauge field equations. *Comm. Math. Phys.*, 100:525–543, 1985.

[75] H. Friedrich. Hyperbolic reductions for Einstein's equations. *Class. Quantum Grav.*, 13:1451–1469, 1996.

[76] U. Gerlach and U. Sengupta. Gauge-invariant perturbations on most general spherically symmetric space-times. *Phys. Rev. D.*, 19:2268–2272, 1979.

[77] Reinaldo J. Gleiser, Carlos O. Nicasio, Richard H. Price, and Jorge Pullin. Gravitational radiation from Schwarzschild black holes: The second order perturbation formalism. *Phys. Rept.*, 325:41–81, 2000.

[78] Reinaldo J. Gleiser, Richard H. Price, and Jorge Pullin. Late time tails in the Kerr spacetime. *Class. Quant. Grav.*, 25:072001, 2008.

[79] Roberto Gómez, Luis Lehner, R.L. Marsa, Jeffrey Winicour, A. M. Abrahams, A. Anderson, Peter Anninos, Thomas W. Baumgarte, N. T. Bishop, S. R. Brandt, J. C. Browne, K. Camarda, M. W. Choptuik, Gregory B. Cook, R. Correll, C. R. Evans, L. S. Finn, G. C. Fox, T. Haupt, M. F. Huq, L. E. Kidder, S. A. Klasky, P. Laguna, W. Landry, J. Lenaghan, J. Masso, R. A. Matzner, S. Mitra, Philippos Papadopoulos, M. Parashar, L. Rezzolla, M. E. Rupright, F. Saied, P. E. Saylor, Mark A. Scheel, E. Seidel, Stuart L. Shapiro, D. Shoemaker, L. Smarr, B. Szilagyi, Saul A. Teukolsky, M. H. P. M. van Putten, P. Walker, and J. W. York Jr. Stable characteristic evolution of generic three-dimensional single-black-hole spacetimes. *Phys. Rev. Lett.*, 80:3915–3918, 1998.

[80] Roberto Gómez, R.L. Marsa, and Jeffrey Winicour. Black hole excision with matching. *Phys. Rev. D*, 56:6310–6319, 1997. gr-qc/9708002.

[81] Jose A. Gonzalez, Ulrich Sperhake, Bernd Bruegmann, Mark Hannam, and Sascha Husa. Total recoil: the maximum kick from nonspinning black-hole binary inspiral. *Phys. Rev. Lett.*, 98:091101, 2007.

[82] T. Goodale, G. Allen, G. Lanfermann, J. Massó, T. Radke, E. Seidel, and J. Shalf. The Cactus framework and toolkit: Design and applications. In *Vector and Parallel Processing - VECPAR'2002, 5th International Conference, Lecture Notes in Computer Science*, Berlin, 2003. Springer.

[83] E. Gourgoulhon, P. Grandclément, K. Taniguchi, J. Marck, and S. Bonazzola. Quasiequilibrium sequences of synchronized and irrotational binary neutron stars in general relativity: Method and tests. *Phys. Rev. D*, 63:064029, 2001.

[84] Philippe Grandclément, Eric Gourgoulhon, and Silvano Bonazzola. Binary black holes in circular orbits. II. Numerical methods and first results. *Phys. Rev. D*, 65:044021, 2002.

[85] A. Gullstrand. Allgemeine lösung des statischen einkörperproblems in der einsteinschen gravitationstheorie. *Ark. Mat. Astron. Fys.*, 16(8):1–15, 1922.

[86] C. Gundlach and J. M. Martin-Garcia. Gauge-invariant and coordinate-independent perturbations of stellar collapse I: the interior. *Phys. Rev. D*, 61:08024, 2000.

[87] Carsten Gundlach, Jose M. Martin-Garcia, G. Calabrese, and I. Hinder. Constraint damping in the z4 formulation and harmonic gauge. *Class. Quantum Grav.*, 22:3767–3774, 2005.

[88] Bertil Gustafsson. On the convergence rate for difference approximations to mixed initial boundary value problems. Technical Report 33, Department of Computer Science, Uppsala University, May 1971.

[89] Bertil Gustafsson. The convergence rate for difference approximations to mixed initial boundary value problems. *Mathematics of Computation*, 29(130):396–406, 1975.

[90] F. Herrmann, I. Hinder, D. Shoemaker, and P. Laguna. Unequal-Mass Binary Black Hole Plunges and Gravitational Recoil. *Class. Quant. Grav.*, 24:S33–S42, 2007.

[91] Frank Herrmann. private communication, 2009.

[92] J. Hesthaven. Spectral penalty methods. *Appl. Numer. Math.*, 33 (1-4):23, 2000.

[93] Markus Heusler. Stationary black holes: Uniqueness and beyond. *Living Reviews in Relativity*, 1(6), 1998.

[94] Peter Hübner. From now to timelike infinity on a finite grid. *Class. Quantum Grav.*, 18:1871–1884, 2001.

[95] Kunihito Ioka and Hiroyuki Nakano. Second and higher-order quasi-normal modes in binary black hole mergers. *Phys. Rev.*, D76:061503, 2007.

[96] R. P. Kerr. Gravitational field of a spinning mass as an example of algebraically special metrics. *Phys. Rev. Lett.*, 11:237–238, 1963.

[97] Gaurav Khanna, Reinaldo Gleiser, Richard Price, and Jorge Pullin. Close limit of grazing black hole collisions: Non-spinning holes. *New J. Phys.*, 2:3, 2000.

[98] L. E. Kidder, Mark A. Scheel, and Saul A. Teukolsky. Extending the lifetime of 3D black hole computations with a new hyperbolic system of evolution equations. *Phys. Rev. D*, 64:064017, 2001.

[99] L. E. Kidder, Mark A. Scheel, Saul A. Teukolsky, E. D. Carlson, and Gregory B. Cook. Black hole evolution by spectral methods. *Phys. Rev. D*, 62:084032, 2000.

[100] Lawrence E. Kidder, Lee Lindblom, Mark A. Scheel, Luisa T. Buchman, and Harald P. Pfeiffer. Boundary conditions for the einstein evolution system. *Phys. Rev. D*, 71:064020, 2005.

[101] Lawrence E. Kidder, Lee Lindblom, Mark A. Scheel, Luisa T. Buchman, and Harald P. Pfeiffer. Boundary conditions for the Einstein evolution system. *Phys. Rev. D*, 71:064020, 2005.

[102] K. D. Kokkotas and B. G. Schmidt. Quasi-normal modes of stars and black holes. *Living Rev. Rel.*, 2:1999–2, 1999. http://www.livingreviews.org/lrr-1999-2.

[103] A. V. Koldoba, M. M. Romanova, G. V. Ustyugova, and R. V. E. Lovelace. Three Dimensional MHD Simulations of Accretion to an Inclined Rotator: The Cubed Sphere Method. *Astrophys. J.*, 576:L53–L56, 2002.

[104] C. Konigsdorffer, G. Faye, and G. Schafer. Binary black-hole dynamics at the third-and-a-half post-newtonian order in the adm formalism. *Phys. Rev. D*, 68:044004, 2003.

[105] M. Koppitz, D. Pollney, C. Reisswig, L. Rezzolla, J. Thornburg, P. Diener, and E. Schnetter. Recoil Velocities from Equal-Mass Binary-Black-Hole Mergers. *Phys. Rev. Lett.*, 99(4):041102, July 2007.

[106] H. O. Kreiss and G. Scherer. Finite element and finite difference methods for hyperbolic partial differential equations. In C. De Boor, editor, *Mathematical Aspects of Finite Elements in Partial Differential Equations*, New York, 1974. Academica Press.

[107] H. O. Kreiss and G. Scherer. On the existence of energy estimates for difference approximations for hyperbolic systems. Technical report, Dept. of Scientific Computing, Uppsala University, 1977.

[108] Stephen R. Lau. Analytic structure of radiation boundary kernels for blackhole perturbations. *J. Math. Phys.*, 46:102503, 2005.

[109] E.W. Leaver. An analytic representation for the quasi-normal modes of Kerr black holes. *Proc. R. Soc. London, Ser. A*, 402:285–298, 1985.

[110] Luis Lehner, David Neilsen, Oscar Reula, and Manuel Tiglio. The discrete energy method in numerical relativity: Towards long-term stability. *Class. Quant. Grav.*, 21:5819–5848, 2004.

[111] Luis Lehner, Oscar Reula, and Manuel Tiglio. Multi-block simulations in general relativity: high order discretizations, numerical stability, and applications. *to appear in Class. Quantum Grav.*, 2005.

[112] Luis Lehner, Oscar Reula, and Manuel Tiglio. Multi-block simulations in general relativity: high order discretizations, numerical stability, and applications. *Class. Quant. Grav.*, 22:5283–5322, 2005.

[113] Lee Lindblom, Mark A. Scheel, Lawrence E. Kidder, Robert Owen, and Oliver Rinne. A New Generalized Harmonic Evolution System. *Class. Quant. Grav.*, 23:S447–S462, 2006.

[114] Frank Löffler, Luciano Rezzolla, and Marcus Ansorg. Numerical evolutions of a black hole-neutron star system in full general relativity: Head-on collision. *Phys. Rev. D*, 74:104018, 2006. gr-qc/0606104.

[115] A. I. MacFadyen, S. E. Woosley, and A. Heger. Supernovae, Jets, and Collapsars. *Astrophys. J.*, 550:410, 2001.

[116] M. Maggiore. *Gravitational Waves Volume 1: Theory and Experiments*. Oxford University Press, Oxford, 2008.

[117] Karl Martel and Eric Poisson. Regular coordinate systems for schwarzschild and other spherical spacetimes. *Am. J. Phys.*, 69:476–480, 2001.

[118] Karl Martel and Eric Poisson. Gravitational perturbations of the Schwarzschild spacetime: A practical covariant and gauge-invariant formalism. *Phys. Rev.*, D71:104003, 2005.

[119] José María Martín-García. xperm: fast index canonicalization for tensor computer algebra. *Comp. Phys. Commun.*, 179:597–603, 2008.

[120] K. Mattsson, M. Svärd, and J. Nordström. Stable and accurate artificial dissipation. *J. Sci. Comput.*, 21:57–79, 2004.

[121] C. W. Misner, K. S. Thorne, and J. A. Wheeler. *Gravitation*. Freeman, San Francisco, 1973.

[122] Charles W. Misner and D. H. Sharp. Relativistic equations for adiabatic, spherically symmetric gravitational collapse. *Phys. Rev. B*, 136(2):571–576, 1964.

[123] Charles W. Misner, Kip S. Thorne, and John A. Wheeler. *Gravitation*. W. H. Freeman, San Francisco, 1973.

[124] Alessandro Nagar and Luciano Rezzolla. Gauge-invariant non-spherical metric perturbations of schwarzschild black-hole spacetimes. *Class. Quantum Grav.*, 22:R167, 2005.

[125] Takashi Nakamura, Ken-ichi Oohara, and Y. Kojima. General relativistic collapse to black holes and gravitational waves from black holes. *Prog. Theor. Phys. Suppl.*, 90:1–218, 1987.

[126] Hiroyuki Nakano and Kunihito Ioka. Second Order Quasi-Normal Mode of the Schwarzschild Black Hole. *Phys. Rev.*, D76:084007, 2007.

[127] Andrea Nerozzi, Christopher Beetle, Marco Bruni, Lior M. Burko, and Denis Pollney. Towards wave extraction in numerical relativity: The quasi-Kinnersley frame. *Phys. Rev. D*, 72:024014, 2005.

[128] Andrea Nerozzi, Marco Bruni, Virginia Re, and Lior M. Burko. Towards a wave-extraction method for numerical relativity. IV: Testing the quasi-Kinnersley method in the Bondi-Sachs framework. *Phys. Rev. D*, 73:044020, 2006.

[129] J. Nordström and M. Carpenter. High-order finite difference methods, multidimensional linear problems and curvilinear coordinates. *J. Comput. Phys.*, 173:149–174, 2001.

[130] Roland Oechslin and H. T. Janka. Gravitational waves from relativistic neutron star mergers with nonzero-temperature equations of state. *Phys. Rev. Lett.*, 99:121102, 2007.

[131] P. Painlevé. La mécanique classique et la théorie de la relativité. *C. R. Acad. Sci.*, pages 677–680, 1921.

[132] Enrique Pazos, Ernst Nils Dorband, Alessandro Nagar, Carlos Palenzuela, Erik Schnetter, and Manuel Tiglio. How far away is far enough for extracting numerical waveforms, and how much do they depend on the extraction method? *Class. Quantum Grav.*, 24:S341–S368, 2007.

[133] Enrique Pazos, Manuel Tiglio, Matthew D. Duez, Lawrence E. Kidder, and Saul A. Teukolsky. Orbiting binary black hole evolutions with a multipatch high order finite-difference approach. 2009.

[134] Harald P. Pfeiffer et al. Reducing orbital eccentricity in binary black hole simulations. *Class. Quant. Grav.*, 24:S59–S82, 2007.

[135] Harald P. Pfeiffer, Lawrence E. Kidder, Mark A. Scheel, and Saul A. Teukolsky. A multidomain spectral method for solving elliptic equations. *Comput. Phys. Commun.*, 152:253–273, 2003.

[136] W. H. Press, B. P. Flannery, Saul A. Teukolsky, and W. T. Vetterling. *Numerical Recipes*. Cambridge University Press, Cambridge, England, 1986.

[137] William H. Press and Saul A. Teukolsky. Perturbations of a Rotating Black Hole. II. Dynamical Stability of the Kerr Metric. *Astrophys. J.*, 185:649–674, 1973.

[138] Frans Pretorius. Evolution of binary black hole spacetimes. *Phys. Rev. Lett.*, 95:121101, 2005.

[139] Frans Pretorius. Simulation of binary black hole spacetimes with a harmonic evolution scheme. *Class. Quantum Grav.*, 23:S529–S552, 2006.

[140] R. Price. Nonspherical perturbations of relativistic gravitational collapse. I. scalar and gravitational perturtbations. *Phys. Rev. D*, 5:2419, 1972.

[141] Jocelyn S. Read et al. Measuring the neutron star equation of state with gravitational wave observations. *Phys. Rev.*, D79:124033, 2009.

[142] T. Regge and J. Wheeler. Stability of a Schwarzschild singularity. *Phys. Rev.*, 108(4):1063–1069, 1957.

[143] L. Rezzolla, A. M. Abrahams, Richard A. Matzner, M.E. Rupright, and Stuart L. Shapiro. Cauchy-perturbative matching and outer boundary conditions: computational studies. *Phys. Rev. D*, 59:064001, 1999.

[144] Oliver Rinne. Stable radiation-controlling boundary conditions for the generalized harmonic Einstein equations. *Class. Quant. Grav.*, 23:6275–6300, 2006.

[145] Oliver Rinne, Lee Lindblom, and Mark A. Scheel. Testing outer boundary treatments for the Einstein equations. *Class. Quant. Grav.*, 24:4053–4078, 2007.

[146] I. Robinson and A. Trautman. Some spherical gravitational waves in general relativity. *Proc. Roy. Soc. Lond.*, A265:463–473, 1962.

[147] C. Ronchi, R. Iacono, and P. S. Paolucci. The "cubed sphere": A new method for the solution of partial differential equations in spherical geometry. *J. Comp. Phys*, 124:93, 1996.

[148] M. E. Rupright, A. M. Abrahams, and L. Rezzolla. Cauchy-perturbative matching and outer boundary conditions I: Methods and tests. *Phys. Rev. D*, 58:044005, 1998.

[149] Olivier Sarbach and Manuel Tiglio. Gauge invariant perturbations of schwarzschild black holes in horizon-penetrating coordinates. *Phys. Rev.*, D64:084016, 2001.

[150] Olivier Sarbach and Manuel Tiglio. Boundary conditions for Einstein's field equations: Analytical and numerical analysis. *J. Hyperbol. Diff. Equat.*, 2:839, 2005.

[151] Mark A. Scheel, Adrienne L. Erickcek, Lior M. Burko, Lawrence E. Kidder, Harald P. Pfeiffer, and Saul A. Teukolsky. 3d simulations of linearized scalar fields in kerr spacetime. *Phys. Rev. D*, 69:104006, 2004.

[152] Mark A. Scheel et al. Solving Einstein's equations with dual coordinate frames. *Phys. Rev.*, D74:104006, 2006.

[153] Mark A. Scheel et al. High-accuracy waveforms for binary black hole inspiral, merger, and ringdown. *Phys. Rev.*, D79:024003, 2009.

[154] Erik Schnetter, Peter Diener, Ernst Nils Dorband, and Manuel Tiglio. A multi-block infrastructure for three-dimensional time- dependent numerical relativity. *Class. Quant. Grav.*, 23:S553–S578, 2006.

[155] Erik Schnetter, Peter Diener, Nils Dorband, and Manuel Tiglio. A multi-block infrastructure for three-dimensional time-dependent numerical relativity. *Class. Quantum Grav.*, 23:S553–S578, 2006.

[156] Erik Schnetter, Scott H. Hawley, and Ian Hawke. Evolutions in 3D numerical relativity using fixed mesh refinement. *Class. Quant. Grav.*, 21(6):1465–1488, 21 March 2004.

[157] Paolo Secchi. The initial boundary value problem for linear symmetric hyperbolic systems with characteristic boundary of constant multiplicity. *Differential Integral Equations*, 9:671–700, 1996.

[158] M. Shibata and Takashi Nakamura. Evolution of three-dimensional gravitational waves: Harmonic slicing case. *Phys. Rev. D*, 52:5428, 1995.

[159] M. Shibata and K. Uryū. Gravitational waves from the merger of binary neutron stars in a fully general relativistic simulation. *Prog. Theor. Phys.*, 107:265, 2002.

[160] Masaru Shibata and Yu-ichirou Sekiguchi. Three-dimensional simulations of stellar core collapse in full general relativity: Nonaxisymmetric dynamical instabilities. *Phys. Rev. D*, 71:024014, 2005.

[161] Ulrich Sperhake. Binary black-hole evolutions of excision and puncture data. *Phys. Rev.*, D76:104015, 2007.

[162] B. Strand. Summation by parts for finite differencing approximations for d/dx. *J. Comput. Phys.*, 110:47, 1994.

[163] Bo Strand. *High-Order Difference Approximations for Hyperbolic Initial Boundary Value Problems*. PhD thesis, Uppsala University, Department of Scientific Computing, Uppsala University. Uppsala, Sweden, 1996.

[164] B. Szilágyi, Roberto Gómez, N. T. Bishop, and Jeffrey Winicour. Cauchy boundaries in linearized gravitational theory. *Phys. Rev. D*, 62:104006, 2000.

[165] B. Szilagyi and Jeffrey Winicour. Well-posed initial-boundary evolution in general relativity. *Phys. Rev. D*, 68:041501(R), 2003.

[166] R. Takahashi et al. Operational status of TAMA300 with the Seismic Attenuation System (SAS). *Class. Quant. Grav.*, 25:114036, 2008.

[167] Saul A. Teukolsky. Perturbations of a rotating black hole. I. fundamental equations for gravitational, electromagnetic, and neutrino-field perturbations. *Astrophys. J.*, 185:635–647, 1973.

[168] Jonathan Thornburg. Black hole excision with multiple grid patches. *Class. Quantum Grav.*, 21(15):3665–3691, 7 August 2004.

[169] K. Thorne. Ligo, virgo, and the international network of laser-interferometer gravitational-wave detectors. In M. Sasaki, editor, *Proceedings of the Eighth Nishinomiya-Yukawa Symposium on Relativistic Cosmology*, Japan, 1994. Universal Academy Press.

[170] Manuel Tiglio, Lawrence E. Kidder, and Saul A. Teukolsky. High accuracy simulations of Kerr tails: coordinate dependence and higher multipoles. *Class. Quant. Grav.*, 25:105022, 2008.

[171] Michele Vallisneri. Prospects for gravitational-wave observations of neutron-star tidal disruption in neutron-star/black-hole binaries. *Phys. Rev. Lett.*, 84:3519, 2000.

[172] Clifford M. Will. The confrontation between general relativity and experiment. *Living Reviews in Relativity*, 9(3), 2006.

[173] B Willke, P Aufmuth, C Aulbert, S Babak, R Balasubramanian, B W Barr, S Berukoff, S Bose, G Cagnoli, M M Casey, D Churches, D Clubley, C N Co-lacino, D R M Crooks, C Cutler, K Danzmann, R Davies, R Dupuis, E Elliffe, C Fallnich, A Freise, S Gossler, A Grant, H Grote, G Heinzel, A Hepton-stall, M Heurs, M Hewitson, J Hough, O Jennrich, K Kawabe, K Kotter, V Leonhardt, H Luck, M Malec, P W McNamara, S A McIntosh, K Mossavi, S Mohanty, S Mukherjee, S Nagano, G P Newton, B J Owen, D Palmer, M A Papa, M V Plissi, V Quetschke, D I Robertson, N A Robertson, S Rowan, A Rudiger, B S Sathyaprakash, R Schilling, B F Schutz, R Senior, A M Sintes, K D Skeldon, P Sneddon, F Stief, K A Strain, I Taylor, C I Torrie, A Vec-chio, H Ward, U Weiland, H Welling, P Williams, W Winkler, G Woan, and I Zawischa. The geo 600 gravitational wave detector. *Classical and Quantum Gravity*, 19:1377, 2002. http://geo600.aei.mpg.de.

[174] Jeffrey Winicour. Characteristic evolution and matching. *Living Rev. Rel.*, 1:5, 1998. [Online article].

[175] Jeffrey Winicour. Characteristic evolution and matching. *Living Rev. Rel. (submitted)*, 2005.

[176] Tetsuro Yamamoto, Masaru Shibata, and Keisuke Taniguchi. Simulating co-alescing compact binaries by a new code SACRA. *Phys. Rev.*, D78:064054, 2008.

[177] F. J. Zerilli. Effective potential for even-parity Regge-Wheeler gravitational perturbation equations. *Phys. Rev. Lett.*, 24(13):737–738, 1970.

[178] F. J. Zerilli. Gravitational field of a particle falling in a Schwarzschild geometry analyzed in tensor harmonics. *Phys. Rev. D.*, 2:2141, 1970.

[179] F. J. Zerilli. Tensor harmonics in canonical form for gravitational radiation and other applications. *J. Math. Phys.*, 11:2203–2208, 1970.

[180] Burkhard Zink, Enrique Pazos, Peter Diener, and Manuel Tiglio. Cauchy-perturbative matching revisited: tests in spherical symmetry. *Phys. Rev.*, D73:084011, 2006.

[181] Burkhard Zink, Erik Schnetter, and Manuel Tiglio. Multi-patch methods in general relativistic astrophysics - I. Hydrodynamical flows on fixed back-grounds. *Phys. Rev.*, D77:103015, 2008.

[182] Y. Zlochower, J. G. Baker, M. Campanelli, and C. O. Lousto. Accurate black hole evolutions by fourth-order numerical relativity. *Phys. Rev. D*, 72:024021, 2005.